Optimization of Tin Selenide Thermoelectric Properties

by

Andrew J. Golabek

A thesis

presented to the University of Waterloo

in fulfillment of the

thesis requirement for the degree of

Master of Science

in

Chemistry

Waterloo, Ontario, Canada, 2023

Author's Declaration

I hereby declare that I am the sole author of this thesis. This is a true copy of the thesis, including any required final versions, as accepted by my final examiners. I understand that my thesis may be made electronically available to the public.

Abstract

The high performance thermoelectric material tin selenide is of notable interest to the field of thermoelectric materials; since breaking the record for being the most efficient thermoelectric material due to the ultralow thermal conductivity. These materials have many potential and current applications such as radioisotope generators, waste heat recovery in vehicles, power generation, sensors, and refrigeration.

The optimization of the thermoelectric properties of *p*-type double doped tin selenide, and *n*-type double doped tin selenide have been investigated through the course of this thesis project. The experimental synthesis parameters have been thoroughly investigated to determine a consistent, optimized procedure for the production of polycrystalline tin selenide thermoelectric materials. The key components of the optimized synthesis procedure include, cooling method from melt synthesis (water quenching), preparation before hot pressing (ball milling 600 rpm, 6 hours), reduction (773 K, 8 hours, 5 % H_2/Ar), and hot pressing parameters (773 K, 48 MPa, 10 min).

Using consistent synthesis methods, the optimization of the composition for the double doped *p*-type, and *n*-type samples was determined by using a triangulated 3-dimensional surface plot for each of the systems. The *p*-type system $Na_xCu_ySn_{1-x-y}Se$ ($0 \le x \le 0.035$), ($0 \le y \le 0.016$) had two compositions of interest with notably high average and peak thermoelectric figure of merit (*ZT*) $Na_{0.034}Cu_{0.016}Sn_{0.961}Se$ (0.45, 0.96), $Na_{0.0113}Cu_{0.0077}Sn_{0.978}Se$ (0.45, 0.77) between 298 K and 773 K, low minimum thermal conductivities (*K*) of (0.36 W m^{-1} K^{-1}), (0.45 W m^{-1} K^{-1}), and peak electrical conductivity (σ) (132 S cm^{-1} at 420 K), (239 S cm^{-1} at 323 K) respectively. The *n*-type system $Sn_{1-x}Bi_xSe_{1-y}Br_y$ ($0 \le x \le 0.06$), ($0 \le y \le 0.06$) had a composition of interest with notably high

peak and average thermoelectric figure of merit (*zT*) (0.57 at 773 K, 0.21 from 298 K to 773 K), low minimum thermal conductivity (0.48 W m^{-1} K^{-1}), and power factor (3.66 µW cm^{-1} K^{-2}) for $SnSe_{0.94}Br_{0.06}$.

Finally using the fully optimized procedure and compositions three high performance *p*-type, and two *n*-type polycrystalline tin selenide samples were prepared with the compositions; $Na_{0.033}Cu_{0.015}Sn_{0.96}Se$, $Na_{0.033}Ag_{0.015}Sn_{0.96}Se$, $Na_{0.034}Au_{0.015}Sn_{0.96}Se$, $SnSe_{0.94}Br_{0.06}$, $SnSe_{0.94}Cl_{0.06}$. All five samples were prepared using identical sources of tin, and were prepared in parallel to ensure comparison between the different dopants can be consistently determined.

The highest performance *p*-type sample was $Na_{0.033}Ag_{0.016}Sn_{0.963}Se$, with a maximum z*T* of 2.12 at 910 K, an average *zT* of 0.87 from 298 K to 910 K, minimum thermal conductivity of 0.24 W m^{-1} K^{-1} at 910 K and peak power factor of 6.01 µW cm^{-1} K^{-2} at 468-516 K.

The highest performance *n*-type sample was $SnSe_{0.9}Br_{0.1}$, with a maximum *zT* of 0.77 at 910 K, and an average *zT* of 0.34 from 298 K to 910 K, minimum thermal conductivity of 0.49 W m^{-1} K^{-1} at 811 K and peak power factor of 4.89 µW cm^{-1} K^{-2} at 910 K.

Acknowledgements

I would like to thank Professor Holger Kleinke for the opportunity and support in researching thermoelectric materials with the Kleinke lab. Being able to do research which is at the forefront of a field of science had been a lifelong goal of mine. I would also like to thank my committee members Professor Rodney Smith, and Professor Pavle Radovanovic for their time, and teaching during the completion of my studies.

I would also like to thank my lab members Luke Menezes, Daniel Ramirez, Dr. Cheryl Sturm, and Nikhil Barua for their support and guidance with my research. I would also like to thank Dr. Howard Siu for the chance to be a teaching assistant in his Chem313L, and 310L labs, as well as his friendship and support. I would also like to thank Boris Nazareth for his support.

Finally I would like to thank my family, and friends for their support during these years of research.

Table Of Contents

List of Figures

List of Tables

List of Symbols

η	efficiency
K	Kelvin
T_H	Hot End Temperature (K)
T_C	Cold End Temperature (K)
T	Temperature (K)
S	Seebeck Coefficient (uV K^{-1})
σ	Electrical Conductivity (S cm^{-1})
K	Total Thermal Conductivity (W m^{-1} K^{-1})
K_E	Electrical Contribution to Thermal Conductivity (W m^{-1} K^{-1})
K_L	Lattice Thermal Conductivity (W m^{-1} K^{-1})
L_0	Lorenz Number (W Ω K^{-2})
L	Thickness of Pellet
$t_{1/2}$	Time to reach half maximum signal
A	Cross Sectional Surface Area of Bar
C_p	Heat Capacity
α	Thermal Diffusivity
M	Molar Mass
R	Universal Gas Constant
v	
l	Mean Free Path Length
θ	Angle (Degrees)

SC	Single Crystal
PC	Polycrystalline
m^*	Effective Mass of an Electron
τ	Time between collisions
μ	Carrier Mobility
e	Charge
n	Charge Carrier Concentration or Number
h	Planck Constant
k_B	Boltzmann Constant
$\boldsymbol{\theta}$	Entropy per Charge Carrier
N	Number of Charge Carriers
T	Temperature Gradient
$\boldsymbol{u}$	Chemical Potential
G	Gibbs Free Energy
V	Voltage

List of Abbreviations

SC Single Crystal

PC Polycrystalline

P_p Density of Sample (g cm^{-3})

P_L Density of Liquid(g cm^{-3})

M_a Mass of sample in Air

M_L Mass of sample in Liquid

UTC Upper Thermocouple

DTC Lower Thermocouple

PTC1 Top Platinum Thermocouple

PTC2 Bottom Platinum Thermocouple

PF Power Factor ($\mu W\ cm^{-1}\ K^{-2}$)

zT / *ZT* Thermoelectric Dimensionless Figure of Merit

Chapter 1: Introduction

1.1 Thermoelectric Materials Applications

Thermoelectric materials are an interesting type of material with the ability to use an abundant source of energy (heat gradients) and directly convert this into electricity which can then be stored or used immediately.[1-2] With the ability to also create a heat gradient using an applied electric current, there are innumerable possible applications for thermoelectric materials. Similarly to solar power, thermoelectric devices have many advantages over conventional power generation; with no requirement for moving parts, no emissions or waste products during use, and a long lifespan.[3,4,7] Some of the most well known applications of the thermoelectric effect include, radioisotope generators, thermocouples, and consumer devices such as watches.[3–7] A radioisotope generator uses a long lasting nuclear power source which through the waste heat of nuclear decay generates a heat gradient, and therefore allows the use of thermoelectric materials surrounding the power source to generate electricity. A well known example of this is the Voyager spacecrafts, which were powered for over two decades using this type of generator.[8] Perhaps the most common use of the thermoelectric effect is as thermocouples, where the materials generate a small voltage which is directly related to the temperature at the junction, and can therefore be used as a temperature sensor.[6,9] In the future as thermoelectric materials and devices become more efficient and cost efficient, industrial and consumer applications will increase and may include; converting waste exhaust heat from cars, buildings, factories, and electric devices into power, and conversely the opposite effect being used for cooling such as in a refrigerator.[4,7]

1.2 Thermoelectric Effect

Despite the promising characteristics of thermoelectric materials as a power source such as low cost, low toxicity, longevity, the relatively low efficiency has reduced the industrial and consumer applications. Even the highest performance materials have only been able to achieve up to 20 % of the theoretical maximum thermodynamic efficiency. Within the thermoelectric materials field, the efficiency is characterized by the 'dimensionless figure of merit' '*zT* or *ZT*'. This value is used since it can be directly calculated from the properties of the material. The highest *zT* materials currently researched are tin selenides (SnSe), which have achieved *zT* values of 2.5-3.[1,2,10–12] As the *zT* values of devices approach this range, thermoelectric materials will start to become competitive with other energy conversion technologies, and still maintain the previously mentioned inherent benefits.[7]

The thermoelectric effect is used in thermoelectric devices by combining both *p*-type, and *n*-type semiconductor materials, as they are connected into a series, and a heat gradient is applied to both such that both *p*-type and *n*-type sides have a hot end and a cold end, electrical power will be generated as the heat flows from the hot end to the cold end.

The efficiency may be generalized as (η), from the equation;

$$\eta = \frac{P}{Q} \tag{1-1}$$

Where (*P*) is the power generated from the device, and (*Q*) is the flow of heat from the hot to cold side, or in the use of a device as a refrigerator, (*P*) is the power supplied to the device, and (*Q*) is the flow of heat generated (cooling the cold side, and heating the hot side). The

theoretical maximum efficiency of a given device can be found from the following equation;[13,14]

$$\eta_{max} = \frac{T_H - T_C}{T_H} \frac{\sqrt{1+ZT}-1}{\sqrt{1+ZT}+\frac{T_C}{T_H}}$$

(1-2)

Where η_{max} is the peak efficiency, T_H is the hot side temperature in kelvin, T_C is the cold side temperature, and ZT is the figure of merit of the device (from both *p*-type and *n*-type materials used in the devices construction). From this equation we can see that thermoelectric devices operate with an efficiency governed by the maximum Carnot heat engine efficiency, and therefore it can never reach 100 % efficient. Inspecting this equation it becomes immediately obvious that as ZT increases, η_{max} increases, approaching the theoretically perfect Carnot engine efficiency. This dimensionless figure of merit ZT or zT is calculated for a material from the following physical properties; ZT can be directly determined from the following physical properties: Seebeck coefficient (S), electrical conductivity (σ), and thermal conductivity (κ). As well as being dependent on the operating temperature.

$$ZT = \frac{S^2\sigma}{\kappa}T$$

(1-3)

From this equation it is clear that to optimize a thermoelectric material, the Seebeck coefficient, electrical conductivity, and maximum operating temperature must be maximized, while also reducing the thermal conductivity to a minimum. This is a large challenge in the

field of thermoelectric material design because each of these properties are closely related to each other.

1.2.1 Thermal Conductivity

The thermal conductivity κ is one of the key physical properties of a thermoelectric material that determines its maximum efficiency. In general κ refers to the total thermal conductivity which is the sum of the lattice thermal conductivity κ_l and the electrical contribution κ_e .[9,14]

$$\kappa = \kappa_e + \kappa_l \tag{1-4}$$

The common units used in this paper for thermal conductivity are W m^{-1} K^{-1}

The thermal conductivity of both *p*-type and *n*-type materials in a thermoelectric device should be minimized in order to maximize the *ZT* value, as shown earlier in equation (1-3). This can be approached through both the lattice and electrical components of the total thermal conductivity. However because the electrical component is based upon how the propagation of charge carriers through the material effects the total thermal conductivity. Reducing the electrical component is not always desirable since this will correspondingly reduce the electrical conductivity of the material as well, thus canceling any gains made by the reduced total thermal conductivity. Despite this there is a delicate balance that must be made in the optimization of a thermoelectric material with respect to the electrical component of the total thermal conductivity. For example a material with metallic behaviour often have the electrical component dominating the contribution to the total thermal

conductivity, and in some cases decreasing it may be desirable as the trade off in decreased electrical conductivity might be favourable.

The relationship between the electrical and thermal conductivity can be described by the Wiedemann-Franz law.[15,16]

$$\kappa_e = L_0 T \sigma$$

(1-5)

Where (L_0) is the Lorenz number, (σ) is the electrical conductivity, and T is the temperature. The Lorenz number can be measured experimentally, and is approximately 2.44×10^{-8} W Ω K^{-2} for metals and 1.48×10^{-8} W Ω K^{-2} for semiconductors.[17] An interesting method to estimate the Lorenz number calculates it from the Seebeck coefficient, and was confirmed with multiple semiconductor materials.[17] The estimation uses the following equation.

$$L_0 = 1.5 + \exp\left[\frac{\lceil S \rceil}{116 \mu V\ K^{-1}}\right]\ \mathrm{V}^2\ \mathrm{K}^{-2}$$

(1-6)

Because of this simple and direct relationship between electrical conductivity and thermal conductivity, the main focus for reducing the total thermal conductivity for most thermoelectric materials is the lattice contribution. The lattice contribution is often chosen as a target property to reduce because it can be tuned more independently from the electrical conductivity and Seebeck coefficient. The lattice contribution is dependent on the vibration of the atoms within the crystal lattice. These vibrations are referred to as phonons, and as they move through a crystal lattice they transmit heat. The theoretical minimum lattice thermal conductivity K_l can be estimated from the specific heat capacity (C_p), and the phonon

mean-free-path (*l*), and the specific heat capacity can also be estimated using the Dulong-Petit law.[18]

$$K_l = \frac{1}{3} C_p v l \tag{1-7}$$

$$C_p = \frac{3R}{M} \tag{1-8}$$

Where (*R*) is the universal gas constant and (*M*) is the average molar mass of the sample. By tuning the transmission of phonons through the lattice of a material the lattice contribution to total thermal conductivity can be reduced to optimize the *zT* of a material. Methods that seek to do this attempt to scatter the phonon transmission and may include; changing the grain structure, adding defects to the crystal, or addition of heavy atoms.

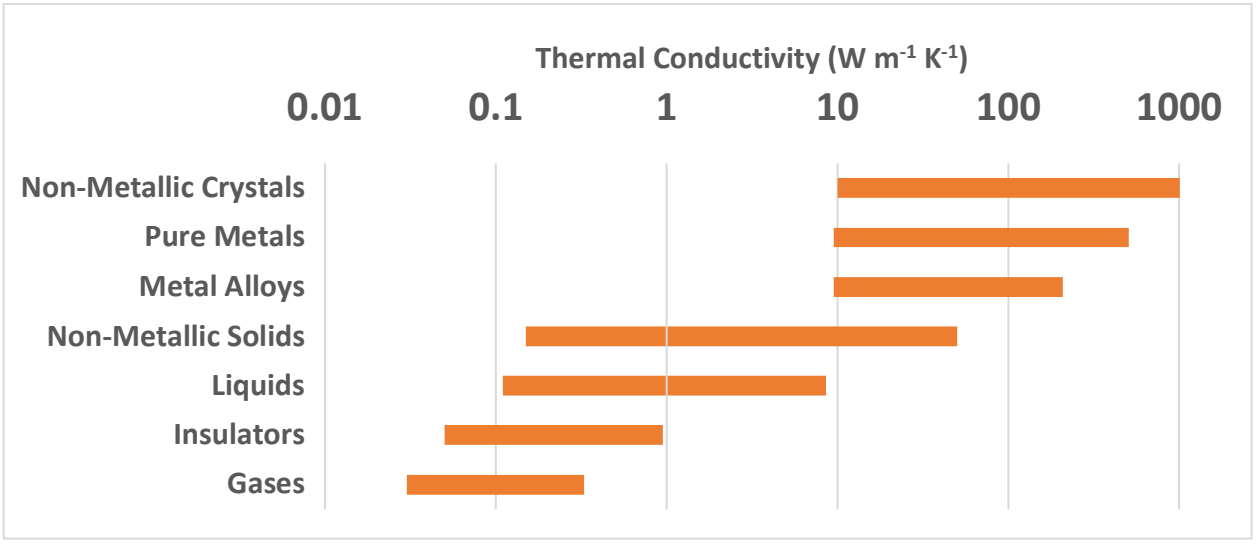

Figure 1. An approximate range of thermal conductivities of various material types.

As shown in Figure 1, the range of thermal conductivities across all materials spans a huge range through many orders of magnitude. Thermal conductivity is one of the most basic physical properties of all materials, and it doesn't give rise to the thermoelectric effect. The property that is key to the operation of thermoelectric devices is the Seebeck coefficient.

1.2.2 Seebeck Coefficient

The Seebeck coefficient is a measurement of the Seebeck effect, where charges build up when a temperature gradient is present through a material. From this basic definition it is easy to see that the Seebeck coefficient can be defined by the following equation;

$$S = \frac{\Delta V}{\Delta T} \tag{1-9}$$

Where S is the Seebeck coefficient, ΔV is the change in voltage, and ΔT is the change in temperature. For a given temperature gradient on a thermoelectric material, the voltage generated is proportional. Therefore the units used are uV K^{-1} . Further if two different metals are connected and the same temperature gradient is applied the voltage generated from each creates an electrical current between the two materials.[7] Because the Seebeck coefficient is dependent on the asymmetry of the charge transport through a material when subject to a thermal gradient it can be described using the ratio of the charge carriers entropy to its charge.[19] Essentially the system can be described with the electrical, and thermal potential summing to the Gibbs free energy of the system.

$$\partial G = -\boldsymbol{S}\partial T + \boldsymbol{u}\partial N \tag{1-10}$$

Where (G) is the Gibbs free energy, ($\boldsymbol{S}$) is the entropy, ($\boldsymbol{u}$) is the chemical potential, (∂T) is the temperature gradient, and (∂N) is the gradient in total number of charge carriers.

$$\frac{\partial \boldsymbol{u}}{\partial T} = \frac{\partial \boldsymbol{S}}{\partial N} = -\boldsymbol{\theta}$$

(1-11)

Where ($\boldsymbol{\theta}$) represents the entropy per charge carrier. Therefore, due to the temperature gradient through the material, the chemical potentials of the charge carriers throughout the material are different along the same gradient. This gradient of chemical potentials can be simply converted into a voltage potential.

$$\partial \phi = \frac{\partial \boldsymbol{u}}{q}$$

(1-12)

Depending on the type of charge carrier, the voltage may be positive (holes) for *p*-type, or negative (electrons) for *n*-type materials. From this the Seebeck coefficient may be calculated with from the voltage and temperature differences;

$$S = \frac{1}{q}\frac{\partial \boldsymbol{u}}{\partial T} = \frac{\boldsymbol{\theta}}{q} = \frac{\partial \phi}{\partial T}$$

(1-13)

For degenerate semiconductors such as most high performance thermoelectric materials, calculating the Seebeck coefficient is more complex, but it can be done using the Mott equation.[15,20]

$$S = \frac{8\pi^2 {k_B}^2}{3eh^2} m^* T \left(\frac{\pi}{3n}\right)^{2/3}$$

(1-14)

Where (k_B) is the Boltzmann constant, (S) is the Seebeck coefficient, (h) is the Planck constant, (T) is the temperature, and m^* is the effective mass. Since the Seebeck coefficient is raised to the second power in calculating the dimensionless figure of merit zT, its often one of the main focuses in increasing the efficiency of a thermoelectric material.

1.2.3 Electrical Conductivity

The last key property for understanding the performance of thermoelectric materials and devices is the electrical conductivity (σ) in S cm^{-1} . The electrical conductivity may be calculated from the following equation where (n) is the number of charge carriers, (e) is the charge of each charge carrier, and (u) is the carrier mobility.[21]

$$\sigma = neu \tag{1-15}$$

The ranges of electrical conductivity span many orders of magnitude from insulators, semiconductors, and metals. Based on the response of a materials electrical conductivity as a function of increasing temperature, a material can be categorized under each of these possible material types.[21] Often for the optimization of thermoelectric materials the target to increase the electrical conductivity is by increasing the carrier concentration. This can be achieved by doping which can either increase the prevalence of holes for p-type materials or free electrons in the material to act as charge carriers. Target carrier concentrations for thermoelectric materials often fall in the range from 10^{19} cm^{-3} to 10^{21} cm^{-3} . From the low end of the range materials will often behave as semiconductors, and as the carrier concentration increases will behave similarly to metals with respect to temperature (heavily doped

degenerate semiconductors). Since the carrier concentration directly affects the Seebeck coefficient, thermal conductivity, and electrical conductivity it might be considered the most important parameter for optimization of a thermoelectric material. Depending on the materials undoped carrier concentration, increasing it is often the goal for the gained electrical conductivity. However this does reach a limit of diminishing returns when as high carrier concentrations and temperature the charge carrier mobility because a limiting factor in the electrical conductivity. This occurs due to scattering of the charge carriers by phonons, which reduces their mean free path, and therefore decreases charge carrier mobility. As shown in the following equation where (τ) is the time between collisions, (l) is the mean free path length, (v) is the velocity of the charge carriers, and (m^*) is the effective mass of an electron.

$$u_e = \frac{e\tau}{m^*} = \frac{el}{m^* v} \tag{1-16}$$

Due to this complex dependence the optimal electrical conductivity is material dependant, as the corresponding Seebeck coefficient, and thermal conductivity are simultaneously affected when tuning the electrical conductivity.

1.3 Tin Selenide

Tin selenide is now known as the record holding thermoelectric material achieving a peak zT of approximately 2.8-3 in both polycrystalline and single crystal samples.[2,11,22] Although tin selenide is relatively new to the field of thermoelectric devices, there has been rapid progress and interest due to the high potential thermoelectric efficiency. A computational approach

revealed a potential peak *zT* of 4.33, showing that the possibility for further improvements in this material still exist.[23] Tin selenide (SnSe) consists of Sn(II) bonded to Se^{-2} in a distorted sodium chloride (NaCl) type structure at room temperature with the space group *Pnma* forming a layered orthorhombic structure. As the temperature increases SnSe undergoes a phase change at approximately 800 K to the *Cmcm* space group.[1,24] As the phase change occurs the thermal conductivity is further reduced leading to even higher *zT*.[1] The maximum

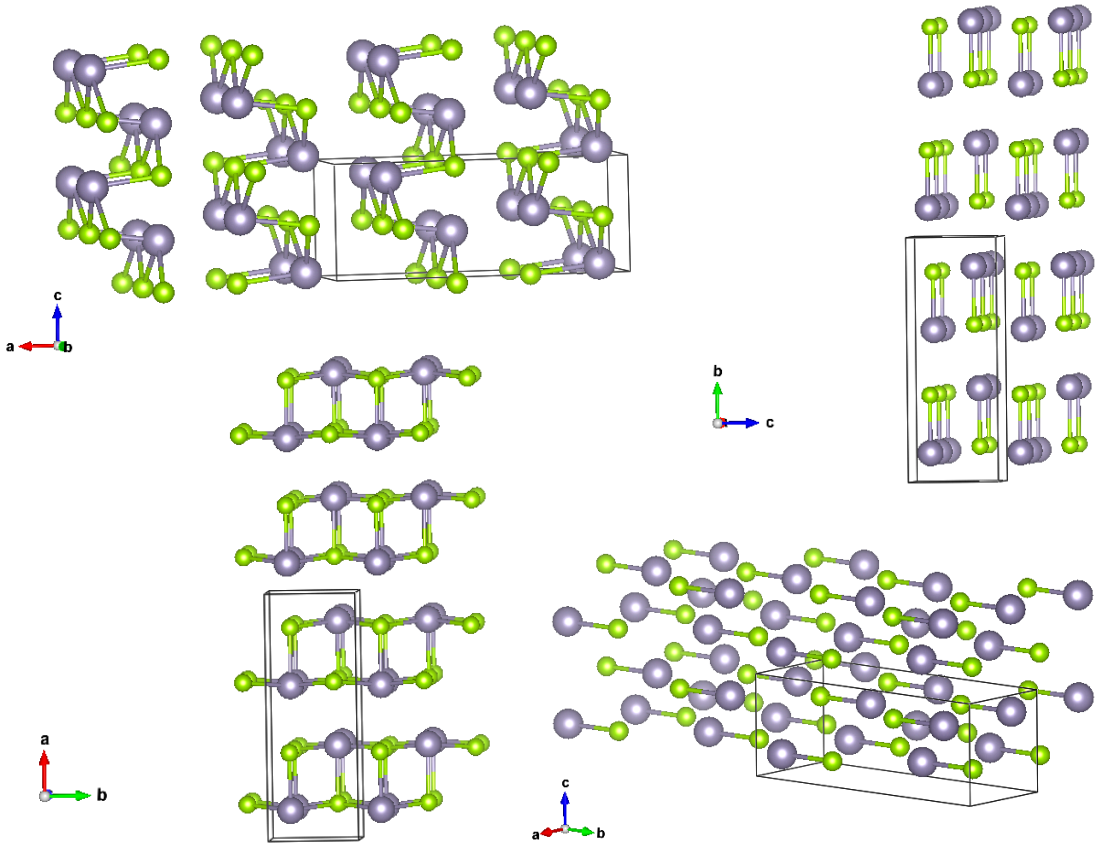

Figure 2. α-SnSe (*Pnma* low temperature phase left) and β-SnSe (*Cmcm* high temperature phase right) crystal structures of tin selenide, (tin silver, selenium green).

operating temperature depends on the specific samples composition due to dopants, and may range from 750 K to 923 K, the limitation occurring due to softening of the material as it approaches the melting temperature at 1134 K.[1]

Pictured in Figure 2, are the two different phases of tin selenide, *Pnma*, and *Cmcm*, the layered structure helps reduce the thermal conductivity due to the high Gruneisen parameters in both phases.

The Gruneisen parameters are the effect of the changing volume of the unit cell due to temperature on the vibrational properties of the crystal lattice. The non-linear effect of the volume change on the restoring force of the atoms displacement in vibration changes the phonon frequencies and therefore can significantly effect the thermal conductivity of the material.[25–27] Aside from the low thermal conductivity, tin selenide also has a relatively high Seebeck coefficient, and with a moderate electrical conductivity the properties are suitable as an ideal thermoelectric material. However this high thermoelectric performance is detracted by high cost of synthesis, poor mechanical properties, and air sensitivity.[1,2] The weak structure is directly due to large cleavage planes formed from the layered structure in single crystal samples, which often have the highest performance thermoelectric properties. The poor mechanical properties, and high cost of synthesis may be improved upon through the use of polycrystalline tin selenide if the thermoelectric properties of polycrystalline tin selenide can consistently match that of single crystal tin selenide.

For many thermoelectric materials the polycrystalline variant often has a higher *zT* due to a reduction in thermal conductivity due to increased phonon scattering from the grain boundaries present.[22] However until recently with the new oxide removal techniques, *zT*

values of polycrystalline tin selenide reported have been consistently lower than the single crystalline variants with usual peak *zT* values of 0.5-1.7 compared to 2.2-2.8 respectively.[2,22] The cause of this discrepancy between single crystal and polycrystalline tin selenide is the much lower electrical conductivity, and higher thermal conductivity attributed to oxidation of the tin.[2,22,28] When preparing tin selenide samples the tin is reactive with oxygen and forms various tin oxides, the majority comprising tin dioxide (SnO_2).[2,22,28]

Since the oxides of tin have much higher thermal conductivity, lower electrical conductivity, and cluster on the grain boundaries, the negative effect on thermoelectric properties is high on polycrystalline samples.[1,2,24] Presumably due to the lack of grain boundaries, and the crystallization process forming single crystal samples, any oxides present in or on the surface of the tin used for synthesis would be limited inside the structure of single crystal samples. This would explain the significant difference in properties commonly observed between single crystal and polycrystalline tin selenide samples. When compared to other high performance thermoelectric materials such as lead telluride (PbTe), and bismuth telluride (Bi_2Te_3), polycrystalline SnSe has similar mechanical properties such as hardness, compressive, and bending strength.[1] One advantage of tin selenide is the high thermal shock resistance of approximately -250 W m^{-1}. This thermal shock resistance is beneficial for thermoelectrics because of the heat gradient used, which often generates large internal stress through the material, and can cause fractures.[1] One of the other key natural features of tin selenide is the anisotropic properties, which means than when measuring the properties, each axis of the unit cell exhibits different electrical and thermal properties. For tin selenide the thermal conductivity is most affected, where the Gruneisen parameter of the

a-axis is much higher compared to the b-, and c- axes (4.1 vs 2.1, 2.3).[12] This difference in properties can be leveraged in single crystal samples by aligning the crystal axes with the thermal gradient to maximize the device efficiency. Polycrystalline samples often have randomly oriented grains, which may reduce the ability of using an optimal orientation, and the measured properties may be an 'average' of the summed orientation of the grains in the bulk sample. However by using a synthesis with preferred orientation of the grains, this can still be used effectively in polycrystalline samples.

With these key natural properties of pure tin selenide, the top methods for improving the thermoelectric properties of tin selenide include doping, and the new method of reduction of tin oxides.

1.3.1 Doping

Considering the electrical conductivity is relatively low, and especially low at room temperatures, one of the most important methods for improving tin selenides thermoelectric properties is through doping, with holes for *p*-type and extra free electrons for *n*-type tin selenide. Doping occurs through either non-stoichiometric synthesis, and or the addition of *p*-, or *n*-type dopants. Regardless of the method, the result is a change in the charge carrier concentration and or type. Pure, stoichiometric tin selenide is a *p*-type semiconductor, however through doping it may become degenerate, and or become *n*-type. By changing the charge carrier concentration through doping, all of the thermoelectric properties may be tuned; electrical conductivity, Seebeck coefficient, and thermal conductivity. In order to successfully use a dopant, it must be soluble within the lattice structure, substitute one of

the sites within the crystal structure and generate either additional holes or free electrons. Other cases where a new element is added but not as a dopant may be referred to as alloying or composites when the element doesn't change the charge carrier concentration. Addition of dopants may also lead to other changes due to disorder, change the band structure, affect physical properties, improve sintering density, or even reduce thermal conductivity with substitution of heavy elements.

There has been extensive research on doping tin selenide, with many elements showing promising results in improving the thermoelectric efficiency. Most doping strategies use p-type dopants since SnSe is naturally a *p*-type semiconductor. However through the use of heavy *n*-type doping there has been successful results achieving zT values greater than 2.[11] The most popular dopants for tin selenide appear to be sodium (Na), potassium (K), copper (Cu), lead (Pb), and silver (Ag).[1,7,36–41,24,29–35] Each of these individual elements has been used successfully to improve the zT of SnSe. Each element when used as a dopant has a slightly different effect on the electrical conductivity when plotted compared to temperature, for example, Ag increases the room temperature electrical conductivity greater than it does so for other temperatures, while Cu increases the electrical conductivity broadly throughout the temperature range of 400k-600k.[33,42,43] The most successful *n*-type dopants used to date are bromine (Br), and bismuth (Bi) both achieving zT values greater than 2.[10,11,44,45] In the single crystal doping with Br was able to increase the zT to a peak of 2.8, while in the polycrystalline sample doping with Br achieved a peak zT of 1.3.[10,11] Interestingly the amount of Br used in doping the polycrystalline samples was much higher (10 %) to achieve maximum performance

as the single crystal samples which only used (3 %) Br.[11] Both studies measuring the amount of Br by % of Se replaced by Br.

The electrical conductivity of the polycrystalline sample with 10 % Br doping was much lower than the single crystal sample with only 3 % Br doping.

Another unusual aspect is the electrical conductivities dependence on temperature when comparing the polycrystalline and single crystal samples, the single crystal samples showed the expected reduction in conductivity with increasing temperature, and increasing Seebeck coefficient for a heavily doped semiconductor.[10] While the polycrystalline doped Br samples showed an increasing electrical conductivity with increasing temperature, and yet still having the same Seebeck coefficient trend.[11]

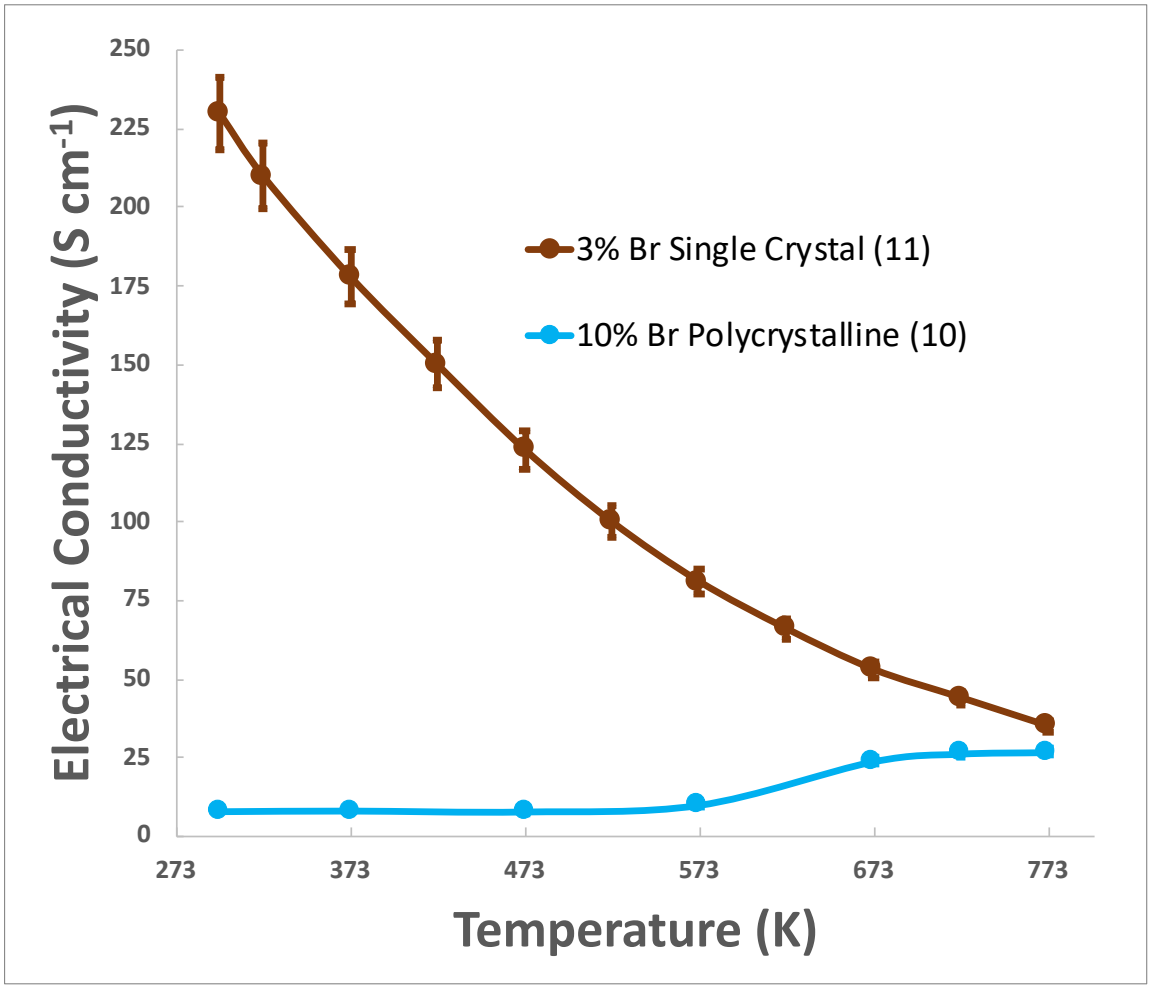

Figure 3. Electrical conductivity of single crystalline, and polycrystalline bromine doped tin selenide showing inverse trends in electrical conductivity (data taken from 10, 11).

Alternatively doping SnSe with holes for increasing the *p*-type carrier concentration can be done with the use of only Sn vacancies, with no additional replacement elements, which has achieved a high *zT* of 2.1 in a polycrystalline $Sn_{0.95}Se$ sample.[46] One advantage of hole doping in this method is a reduced lattice thermal conductivity, caused by the vacancies, and missing interatomic linkages, which lead to increased phonon scattering and reduced phonon travel.[46]

From Table 1. It is observed that some of the most popular and successful dopants for tin selenide are halogens, alkali metals and the ‘coinage’ group 11 metals Cu and Ag. Another common method as shown is by alloying with S or Ge.

Table 1. Top 25 published tin selenide thermoelectric materials peak properties, and type of material [single crystal (SC), polycrystalline (PC)].

Composition	Figure of Merit (*zT*)	Temperature (K)	Thermal Conductivity ($W\ m^{-1}\ K^{-1}$)	Electrical Conductivity ($S\ cm^{-1}$)	Seebeck Coefficient ($\mu V\ K^{-1}$)	SC/ PC	Ref
$Sn_{0.965}Na_{0.03}Se$	3.1	783	0.22	130	290	PC	[2]
$SnSe_{0.97}Br_{0.03}$	2.8	773	0.25	41	-477	SC	[10]
SnSe	2.6	923	0.35	89	342	SC	[12]
$(Sn_{0.95}Pb_{0.05})_{0.99}Na_{0.01}Se$	2.5	773	0.21	93	272	PC	[22]
$Sn_{0.98}Pb_{0.01}Zn_{0.01}Se$	2.2	873	0.21	50	328	PC	[37]
$Sn_{0.95}Se$	2.1	873	0.32	69	337	PC	[46]
$Sn_{0.97}Ge_{0.03}Se$	2.1	873	0.18	68	277	PC	[47]
$Sn_{0.99}Pb_{0.01}Se$+Se QD	2.0	873	0.25	33	425	PC	[48]
$Sn_{0.99}Pb_{0.01}Se_{0.93}S_{0.07}$	1.9	873	0.20	38	315	PC	[49]
$Sn_{0.978}Ag_{0.007}S_{0.25}Se_{0.75}$	1.8	823	0.24	50	325	PC	[50]
SnSe	1.7	758	0.12	22	340	PC	[51]
SnSe +1 % PbSe	1.7	873	0.25	42	330	PC	[52]
$Sn_{0.99}Ag_{0.01}Se_{0.85}S_{0.15}$	1.7	823	0.11	26	296	PC	[36]
$Sn_{0.995}Ag_{0.005}Se$ / 0.5 mol % SnTe	1.6	875	0.45	93	288	PC	[53]
$Sn_{0.882}Cu_{0.118}Se$	1.4	823	0.32	56	316	PC	[54]
$Sn_{0.97}Se_{0.7}S_{0.3}$	1.3	816	0.30	58	300	PC	[55]
$Sn_{0.99}Na_{0.01}Se$-Ag_8SnSe_6	1.3	773	0.39	70	320	PC	[38]
$Sn_{0.985}Ag_{0.015}Se$	1.3	773	0.30	45	344	PC	[41]
$SnSe_{0.9}Br_{0.1}$	1.3	773	0.27	27	-400	PC	[11]
$Sn_{0.99}Cu_{0.01}Se$	1.2	873	0.29	36	314	PC	[33]
$Sn_{0.99}Na_{0.005}K_{0.005}Se$	1.2	773	0.45	35	375	PC	[49]
$(Sn_{0.96}Pb_{0.04})_{0.99}Na_{0.01}Se$	1.1	773	0.35	89	269	PC	[56]
$Sn_{0.999}K_{0.001}Se$	1.1	823	0.30	18	333	PC	[35]
$SnSe_{0.985}Cl_{0.015}$	1.1	773	0.24	26	-399	PC	[41]
$Sn_{0.99}K_{0.01}Se$	1.1	773	0.44	19	421	PC	[29]

1.3.2 Reduction of Oxides

For polycrystalline tin selenide one of the most powerful methods used for improving the properties is by the removal and reduction of the tin oxides within and on the sample.

Recently it was found that the reduction of the tin oxides present on the powdered SnSe using hydrogen gas at an elevated temperature was able to significantly improve the properties of polycrystalline SnSe.[2,22,28] The oxides were found to concentrate along the grain boundaries, thus reducing electrical conductivity, and increase thermal conductivity. The tin oxides present are predominantly SnO_2 which has a total thermal conductivity of approximately 98 W m^{-1} K^{-1} , over a hundred times greater than SnSe.[57] Therefore even a small contamination or oxidation during handling can significantly degrade the properties of the samples. Especially when the sample is in a powdered state and handled in the air, the increased surface area allows for more rapid oxidation. An example of the sensitivity has been shown where addition of 0.005-0.03g SnO_2 to 5g of SnSe (0.1-0.6 wt %) significantly degraded the properties.[57] These oxides are not only present or caused by the sample preparation, but also contributed to from the tin used for synthesis. Despite appearing oxide free, and starting from a high purity of 99.999 %, Zhou et al.[2] reported that this starting material still contains enough oxides to significantly degrade the properties.[2] Interestingly the process used for preparing the samples in this report revealed that the thermal conductivity was mainly affected by the purity of the tin used for synthesis (in regards to being oxide free).

One of the main methods used for preparing tin metal is the use of a carbothermal reduction process, however hydrogen has been shown to be highly effective in reducing tin oxides back

into tin metal[58] Measuring the rate of oxide reduction at different temperatures and hydrogen partial pressures has revealed near complete reduction with times of less than 1 hour using partial pressures between 30.4 kPa, and 101.3 kPa in an argon atmosphere and temperatures between 773 K up to 1023 K. However once the reduction ratio or completeness reaches 95 % the rate reduces significantly, possibly due to the molten tin preventing the hydrogen gas from reaching all the oxide particles. Despite this, by using higher temperatures near 100 % reduction was achieved within a short time frame. The use of higher temperatures was judged to be more effective than by increasing the partial pressure.

Recently, Lee et al.[22] have shown that through ball milling, followed by a reduction process carried out at 613 K, with 4 % H_2/Ar gas flow for 8 hours prior to the sintering stage, was able to significantly improve the thermoelectric properties, notably increasing the electrical conductivity and reducing the thermal conductivity. The oxides were measured using XPS, and shown to have been significantly reduced, but not completely eliminated.[22] This process was able to achieve thermal conductivities of 0.2 W m^{-1} K^{-1} in line with the lowest recorded SnSe thermal conductivities previously reported in single crystal samples. However considering that oxides were still present, though to a low degree, further improvement was postulated by using more effective reduction process such as a higher temperature.[22]

More recently following this new method, Zhou et al.[2] has also shown that by using a process to purify the tin prior to preparation of SnSe powders, and then following with the same reduction process used by Lee et al.[22] the polycrystalline SnSe can achieve thermoelectric performance greater than that of the single crystal. To purify the tin prior to synthesis,

multiple steps were needed. First 99.999 % pure Sn chunks were reduced at 473K with 4 % H_2/Ar gas flow for 6 hours, and then heated to 1223 K in an evacuated ampule. Oxides formed an ash like material on the surface of the tin when cooled. Mechanical removal of the residues followed by the heating to 1223 K and cooling was repeated until the residue was no longer visible, and APT analysis confirmed near complete oxide removal. The purified tin was then used to prepare SnSe doped powders which were then reduced again at 613 K with 4 % H_2/Ar gas flow for 6 hours. The thermal conductivity, and electrical conductivity were improved with this process, while the Seebeck coefficient was unchanged, together this lead to an improved *zT* of approximately 3 at 773 K with the purified, reduced $Sn_{0.97}Na_{0.03}Se$ samples.

The significant effect of oxides has also brought into question the comparability of polycrystalline tin selenide thermoelectric results. When comparing any two published results, differing levels of oxygen may have accounted for the majority or all of the difference in thermoelectric properties. However when looking within one study, assuming each sample was prepared with the exact same tin starting material results should be internally consistent. Another aspect to consider is that addition of new elements or phases may have affected the amount of oxygen within the structure, or even changed how easily oxidized the samples are, therefore improving or reducing the thermoelectric properties indirectly.

1.3.3 Alloying/Composites and Nano-Structuring

Another interesting method for improving the properties of thermoelectric materials is through creating composite or alloyed materials, and through nano-structuring.[1] Most often these techniques aim to increase phonon scattering, thereby reducing the lattice thermal conductivity. Addition of new phases, porosity, defects, new elements alloying can all be used to adjust various properties. A common and simple method for improving the properties is through grain refinement. Reducing the grain size increases phonon scattering, as well as increasing mechanical strength.[1] Two common methods for reducing the grain size are ball milling, and addition of new phases. An example of grain refinement leading to a 70 % increase in zT was demonstrated by Li et al.[55]

Transmission electron microscopy was used to inspect the polycrystalline sintered samples, and revealed that the addition of a tin sulfide phase greatly reduced the grain size. The areas of new SnS phase were on the nanoscale and only visible using the TEM method. Differing amounts of Se replaced by S were used ranging from 10 % to 40 % atomic amounts. The full range of sulfur alloying had a significant effect on the lattice thermal conductivity and the total thermal conductivity, increasing the zT to 1.35 with the composition $Na_{0.03}Sn_{0.97}Se_{0.7}S_{0.3}$.

Chapter 2: Materials and Methods

2.1 Sample Preparation

Sample preparation for making polycrystalline tin selenide samples include multiple steps, starting from the purification of tin, synthesis of the tin selenide doped samples, followed by a reduction process and finally sintering pellets and cutting into shapes suitable for thermoelectric property measurement.

2.1.1 Synthesis

The synthesis process began with purification of the tin starting material. Elemental tin (Sn) 99.6 % purity was first washed with 10 % HCl, then dried and loaded into an Argon filled quartz tube, evacuated to <0.001 mBarr, followed by melting at 1273-1323 K. After cooling, the surface of the ingots was washed with 10 % HCl, brought back into the Ar filled glovebox, and wiped clean before loading into a new quartz tube and repeating. Subsequent ingots progressively had less oxide residues, and were not exposed to the air or washed with 10 % HCl, but had the surfaces cleaned by sanding and or scrapping while inside the glovebox. The process was repeated until no visible residues formed after the melting step.

The tin ingots were then cut into chunks inside the glovebox for future use.

The simplest and most reliable method determined for synthesis of the tin selenide samples was a melt synthesis. A series of samples was prepared using a ball milling only synthesis, however it is likely that full reaction did not occur as evidenced by the poor thermal stability observed, with samples bubbling after high temperature property measurements such as thermal diffusivity and electrical conductivity.

For melt synthesis, the tin chunks (either purified or not) were weighed and loaded into a quartz ampule along with Se pellets while inside the glovebox with <0.1ppm O_2 and <0.1ppm H_2O. Ampules were then evacuated to <0.001mBarr, followed by melting at 1273-1323K for periods ranging from 30 minutes up to 12 hours. From the binary phase diagram of Sn-Se, it is clear that any melting synthesis attempt to prepare SnSe must surpass 1146K.[1]

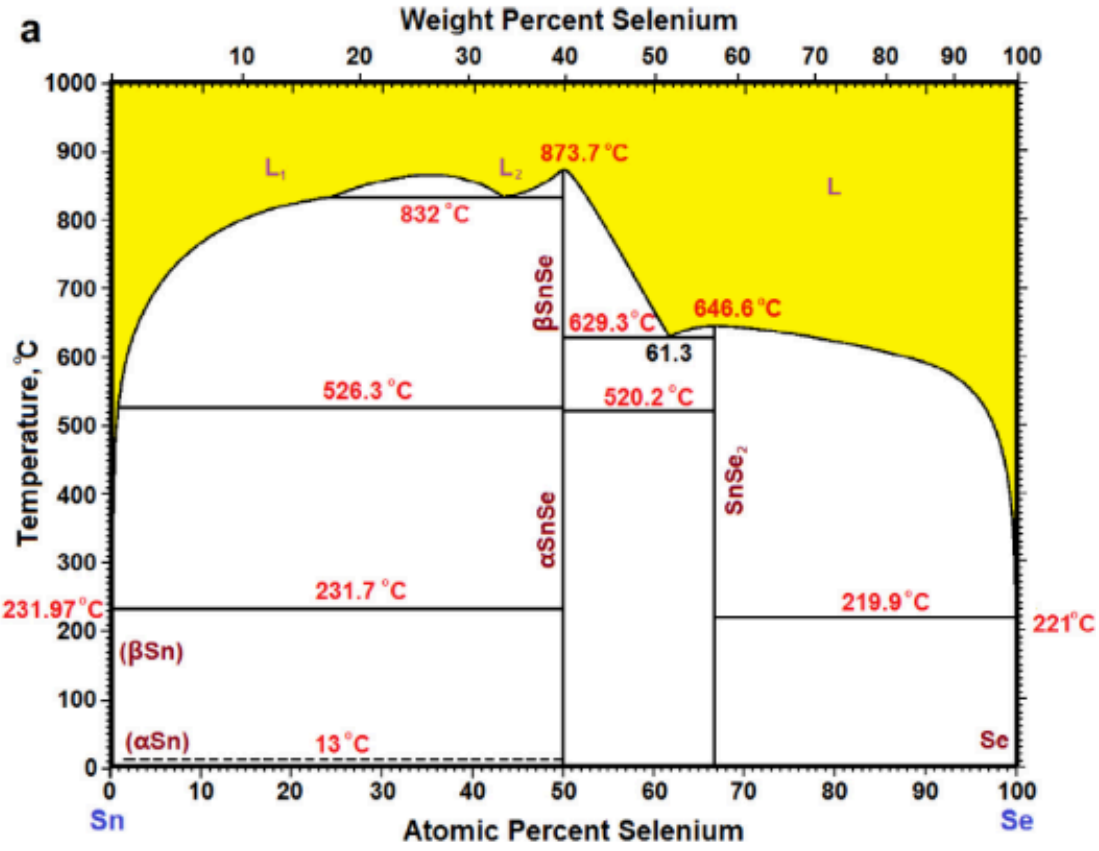

Figure 4. Phase diagram of Sn and Se.[1]

Testing with a lower temperature melt showed incomplete reactions of the tin metal. After melting, the ampules were either cooled inside the furnace, air cooled on a firebrick, or water quenched into room temperature water. Ampules were then brought into the

glovebox and cracked open. From this stage the samples were ready for either sintering or for the reduction process.

2.1.2 Reduction

For the reduction process the samples must be an adequately fine powder to ensure maximal surface area for the hydrogen gas to reduce any oxides present. The previously melted tin selenide samples are then ground in a mortar and pestle until they are a fine uniform powder. The powder can then be reduced immediately or ball milled into a finer powder. If ball milling, the powder is loaded into a zirconium oxide ball mill jar inside the glovebox, sealed with argon, and then ball milled at 600rpm for between 30 minutes and 8 hours depending on the particular sample. Then the fine powder is loaded into an alumina boat, and transferred quickly from the glovebox into the reduction furnace.

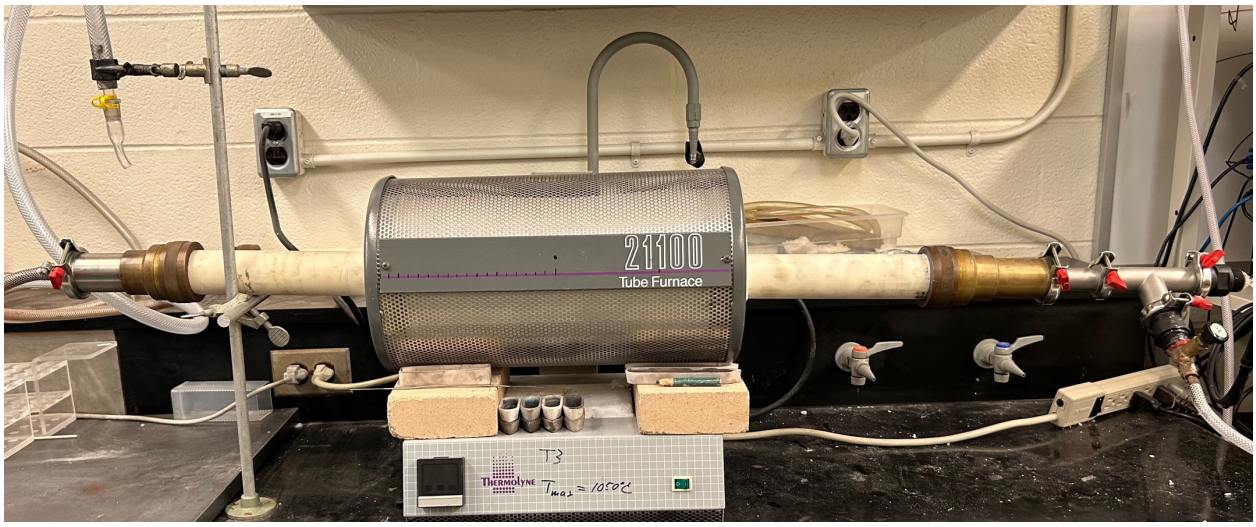

Figure 5. Tube furnace set up for reducing samples with 5 % H_2/Ar gas supply, and additional internal thermocouple.

The reduction furnace consists of a tube furnace with an alumina tube connected to a 5 % H_2/Ar gas supply, along with an additional thermocouple to precisely measure the actual sample temperature. Excess gas flow bubbles through water inside the fume hood to gauge the gas flow rate. The furnace was turned on after 10minutes of gas flow to prevent oxidation occurring as the temperature increases. Each reduction was completed for between 4-24 hours at temperatures ranging between 573 K and 823 K.

After reduction the samples are quickly transferred back into the glovebox.

2.1.3 Sintering and Sample Preparation

Regardless of if a particular sample was reduced or not, the process for sintering was the same. After visual inspection the fine tin selenide powder was loaded into a graphite die with graphite paper inserts to ensure it doesn't stick to the graphite plungers. The usual amount of sample needed for pressing was between 1.5 and 3g. Hot pressing (HP) was done with the OXY-GON Industries Hot Press Furnace.

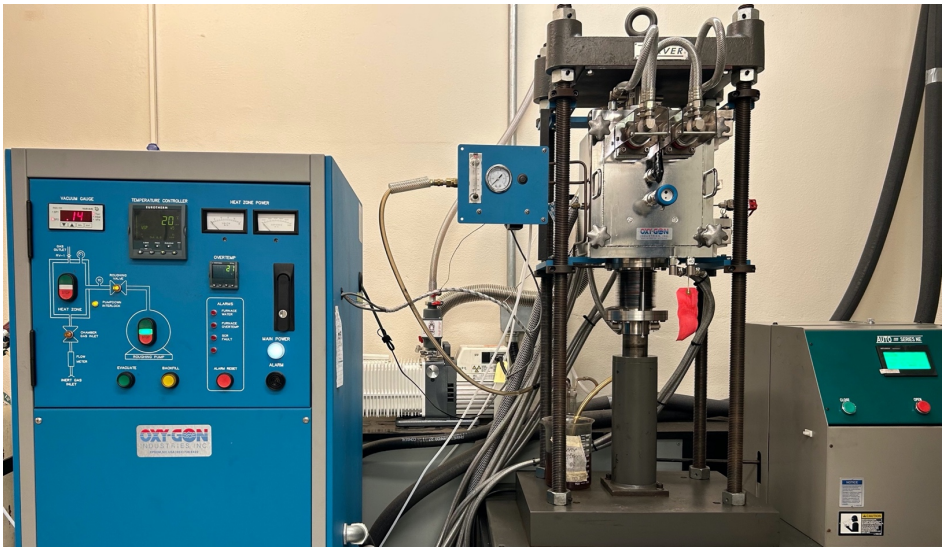

Figure 6. OXY-GON Industries Hot Press-Furnace.

Various hot pressing parameters were tested with temperatures ranging from 673 K up to 823 K, pressures ranging between 39.9 and 55.8 MPa, and sintering times between 10 minutes and 8 hours. All hot pressing was done after evacuation of the chamber, and under a 5 % H_2/Ar gas flow to ensure oxidation doesn't occur.

Samples which were spark plasma sintered (SPS) were brought to McMaster University and sintered at 773 K with a ramp time of 15 minutes, and a 5 minute hold time.

After sintering the samples were cut using a diamond coated copper cutting wheel with ethanol as the lubricant. Since some samples were noted to be sensitive to water.

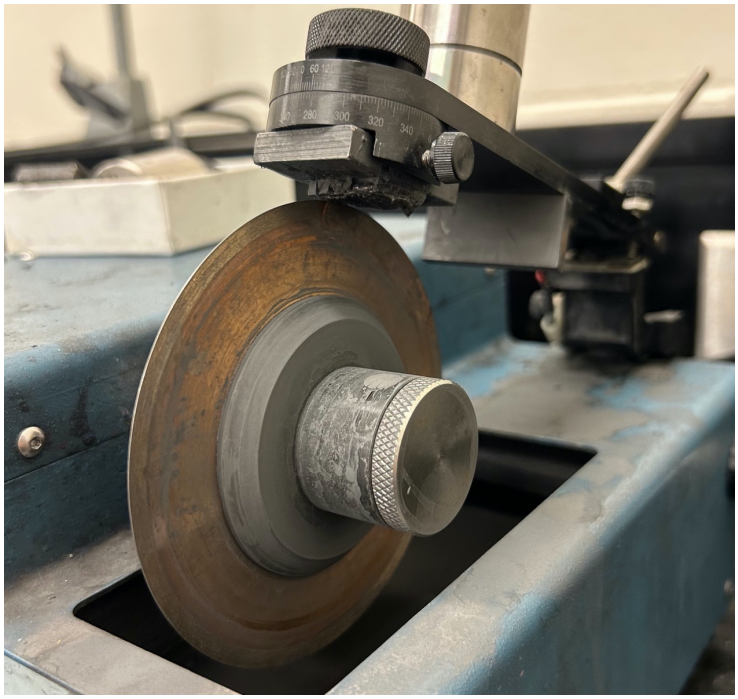

Figure 7. Diamond coated copper cutting disc setup. Samples are hot glued to the plate.

Samples were cut into disc shaped pellets for measuring the thermal diffusivity, and into bars approximately 10 mm $\times$ 2 mm $\times$ 2 mm for measuring the electrical conductivity and Seebeck coefficient.

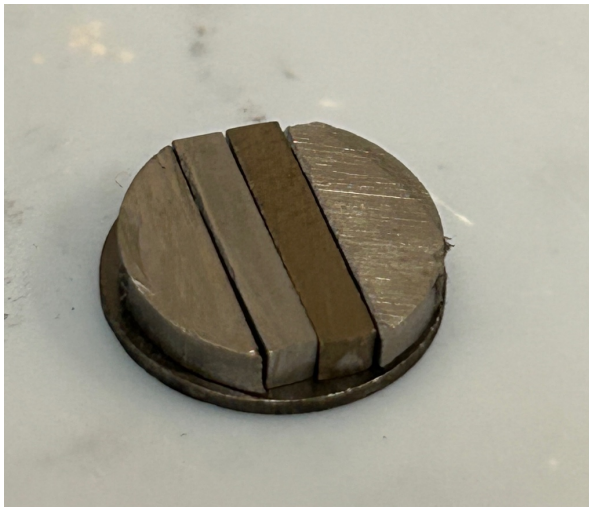

Figure 8. Typical sample cutting method used for samples in this thesis project.

2.2 Measurements

The standard measurements completed included powder x-ray diffraction (pXRD), scanning electron microscopy (SEM), laser flash thermal diffusivity (TD), and electrical conductivity and Seebeck coefficient determination using the Ulvac ZEM (ZEM) instrument.

2.2.1 Powder X-ray Diffraction

Select samples were analyzed using the INEL X-ray powder diffractometer with a position sensitive detector, and Cu alpha radiation source with an acceleration voltage of 30 kV and 30 mA. All of the powder patterns were completed at room temperature in an air atmosphere and with 2 theta values between 5° and 120°

Powder X-ray diffraction uses the phenomenon where X-ray beams are diffracted by electrons in crystalline solids. These X-rays are created by aiming a beam of high energy electrons at a target metal (copper in this case), where it dislodges core electrons in the atom, creating a vacancy. Electrons then fall from a high energy level into this vacancy, and in doing

so release corresponding energy electromagnetic radiation determined by the difference in electron energy levels. The electromagnetic radiation has a high energy and falls into the X-ray spectrum. The X-rays formed are selected to be monochromatic (a very narrow range of wavelengths), and target a crystalline material. The electrons within the crystal scatter the X-rays and the resulting diffracted X-rays are measured by the detector. Since the X-rays interact with the material in a 3-dimensional manner, the symmetry of the crystal can be determined.

For crystalline systems with repeating structural units, there exist repeating crystal planes, which are parallel to each other, and equally spaced, identified by the Miller indices (*h k l*). The separation between the crystal planes is referred to as the *d*-spacing (d_{hkl}). Incident X-rays which are diffracted off of different crystal planes have different path lengths which are determined by the angle (θ) of the incident beam, and the *d*-spacing (d_{hkl}). Bragg's Law uses the difference in path length to calculate when constructive interference and destructive will occur, where *n* is an integer, and λ is the wavelength of the X-ray.

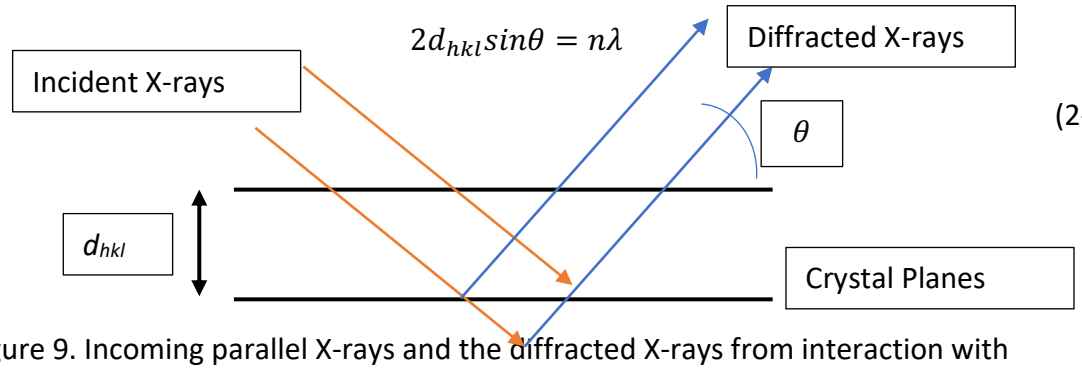

(2-1)

Figure 9. Incoming parallel X-rays and the diffracted X-rays from interaction with different crystal planes, and equation (2-1) Bragg's Law.

The resulting diffraction pattern peak intensities, shapes, and positions can give insight into the crystal structure of the material being analyzed.

2.2.2 Scanning Electron Microscope

Samples of particular interest were subjected to the scanning electron microscope (SEM). The FEI Quanta FEG ESEM instrument was used. The SEM creates thermionically emitted electrons, from a tungsten filament which are then accelerated by a high voltage field, and focused into a very small dot of approximately 50 Å – 500 Å on the surface of samples being analyzed. The electrons create secondary electrons which are detected to create images from the lighter elements in the sample, and backscattered electrons create images from the heavier elements in the sample. Energy dispersive X-ray analysis (EDAX) was also performed, this method works through the ejection of electrons from the inner shell of the samples atoms, followed by electrons falling from the outer shell into the vacancy created. This releases X-rays similarly to the method used for generating the X-rays in the pXRD instrument. The X-ray spectrum generated has characteristic peaks of particular atoms, which can be used to determine the composition of a localized spot of the sample being bombarded with electrons.

2.2.3 Thermal Conductivity Determination

After the pellet is cut into a disc between 0.6 mm and 1.5 mm thick with a diameter of 12.5 mm, the density is measured using the Archimedes principle with a Sartorius YDK01 density determination kit. To measure the density the weight of the pellet is determined in air, and then it is submerged in a suitable liquid (either water or ethanol) and weighed a second time while ensuring no air is trapped. The temperature is also taken to ensure the density of the liquid being used is accurate. The buoyancy of the pellet in air and the liquid is used to determine the volume of the pellet, and the corrected weight. Therefore the density of the pellet (P_p) can be calculated using the following equation.

$$P_p = \frac{M_a(p_L - 0.0012\ g\ cm^{-3})}{(M_a - M_L) * 0.99983\ g} + 0.0012\ g\ cm^{-3} \quad (2\text{-}2)$$

The density of the liquid the pellet is submerged into being P_L , M_a being the mass of the pellet when measured in air, and M_L being the mass of the pellet when measured while submerged in the liquid. The constant of +0.0012 g cm^{-3} is the correction for the density of air, and 0.99983 g is the correction factor associated with the wires of this particular density determination kit.

Once the density has been determined, and the pellet has been coated in an evenly sprayed on layer of graphite, it is ready for the thermal diffusivity (α) measurement using the TA-Instruments DLF-1200. The purpose of the graphite layer being to ensure the surface of the sample absorbs the laser flash effectively, as well as the top surface having the adequate emissivity. After the samples are loaded into the instrument, the chamber is evacuated, and

then refilled with argon gas, which continuously flows during the course of the measurements.

At each measurement the laser flash heats the bottom surface of the pellet, and the temperature of the upper surface of the pellet is recorded as a function of time (thermogram) as seen in Figure 10.

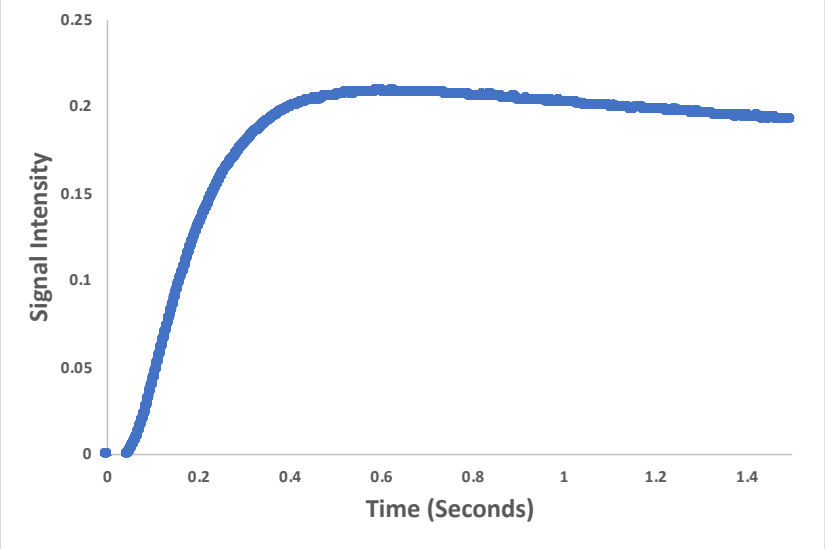

Figure 10. Thermogram example from a pure SnSe sample at room temperature.

The thermogram is used to calculate the time it takes to reach half of the maximum temperature ($t_{1/2}$) The thermal diffusivity is then calculated with the following simple formula;

$$\alpha = 0.1388 \frac{L^2}{t_{1/2}} \tag{2-3}$$

Where *L* is the thickness of the pellet, from here the total thermal conductivity is calculated using the following relation.

$$k_{total} = \alpha * C_p * \rho$$

(2-4)

Where C_p is the heat capacity, which is either calculated using the Dulong-Petit equation, or experimentally, and ρ is the density of the pellet. The experimental error for the thermal conductivity is estimated to be ±5 %.

2.2.4 Electrical Conductivity and Seebeck Coefficient Determination

From the sintered pellet, the bar of approximately 8-12 mm long by 1.5-2.5 mm thick by 1.5-2.5 mm is sanded, and the surface is cleaned to ensure good contact with the electrodes, and thermocouples of the Ulvac ZEM instrument. The sample bar is measured to 0.01mm accuracy, and placed between two current supply electrodes, and additionally two platinum thermocouples make contact with one side of the bar, as shown in the following figure. additionally graphite paper is used to ensure good contact between the electrodes, and thermocouples with the bar.

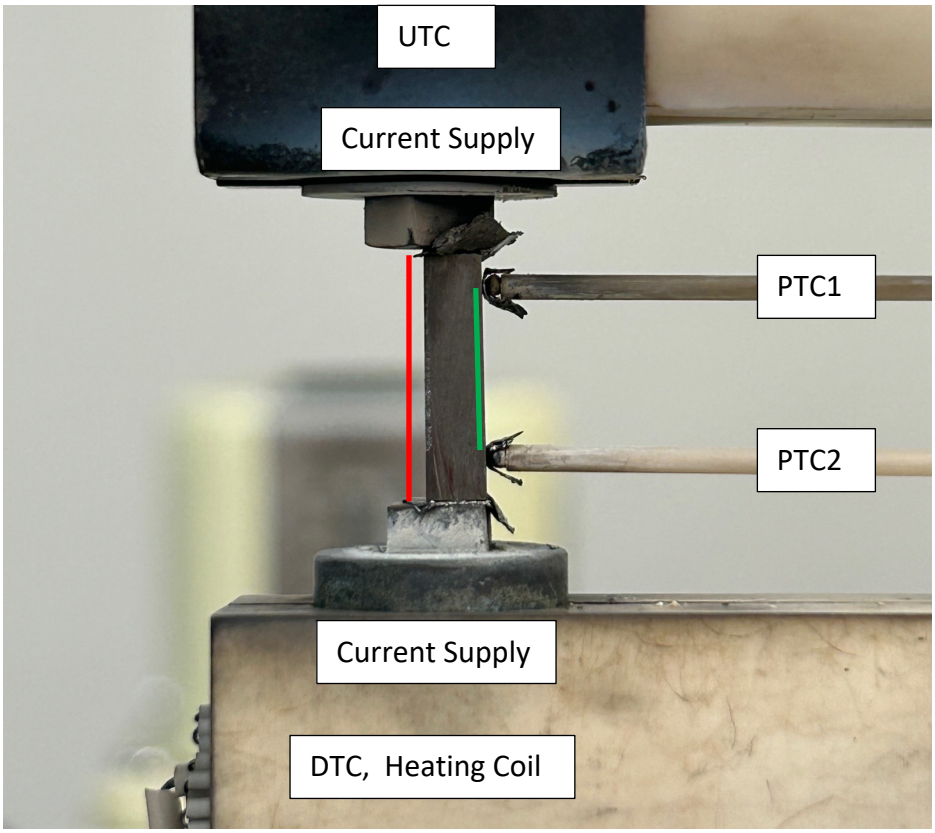

Figure 11. Properly setup sample for ZEM measurement with graphite paper covering the PTC1, and PTC2 thermocouples, current supply electrodes , and visible lower thermocouple (DTC), upper thermocouple (UTC), and heating coil. The calibration distance, and thermocouple separation are also indicated with the red and green lines respectively.

Additionally graphite paper is used to ensure good contact between the electrodes, and thermocouples with the bar. Finally the distance between the PTC1 and PTC2 thermocouples is recorded using the calibrated camera. The method used to calibrate the camera for each sample was as follows; the total sample length was measured using the micrometer, followed by placement of the sample. When the picture is taken, the calibration option is chosen first

to calibrate the magnification of the camera, and then the measurement of the thermocouple separation is recorded. Once this is completed, the chamber is evacuated, and refilled with ultra-pure helium gas (99.9995%). The sample is heated using an infrared furnace to the target temperature, while the lower heating coil near the bottom electrode and PTC2 thermocouple ensure the correct temperature difference for each measurement. At each target temperature, 4 measurements are taken, with one occurring with a delta T of 0, and followed by 3 successive measurements with increasing delta T (*dT*) in order to measure the Seebeck coefficient of the sample. The temperature differential that occurs between the bottom electrode and the top electrode being the set delta T, and the effective delta T being the temperature difference between PTC1 and PTC2. The thermal electromotive force (*dE*) is measured between the two PTC thermocouples which both contain the same type of wires, and this allows for a measurement of the change in voltage potential (*dV*).

Together with delta T, this is used to calculate the thermopower/Seebeck coefficient.

$$S = \frac{dV}{dT} \tag{2-5}$$

The electrical resistance was also measured using this four-probe method, where the lower and upper current supply electrodes supply a constant current, and the voltage difference (*dV*) is measured using the two PTC thermocouples. The total resistance is calculated from the current (I) and the voltage difference (*dV*).

$$R = \frac{dV}{I} \tag{2-6}$$

Finally using Ohm's law the resistivity and electrical conductivity of the sample is calculated with the following equation where *A* is the cross sectional surface area of the sample bar, and *D* is the distance between the PTC1 and PTC2 thermocouples.

$$p = R * \frac{A}{D} = \frac{1}{\sigma} \tag{2-7}$$

The experimental error is estimated to be ±5 % for both the electrical conductivity and the Seebeck coefficient. Together with the thermal conductivity measurement the total error of *zT* determination is estimated to be ±10 %.

2.3 Optimization of Synthesis Parameters

Prior to the optimization of composition, the synthesis process needed to be refined in order to generate reliable performance. Starting from the basic sample preparation outline of; melt synthesis, sample grinding, reduction, and sintering. Each of these steps individually has many parameters that can be changed. Herein the focus is on some of the parameters that have been shown to have the strongest effects on the properties of the final thermoelectric material.

2.3.1 Cooling Method from Melt

One of the first experiments completed in this project to optimize the synthesis of polycrystalline tin selenide was a comparison of different methods for cooling the sample after the melting step. As the sample cools down from the molten state, it crystallizes. The formation of the crystals is dependent on the temperature and rate of cooling. With a higher

cooling rate the expectation would be to have smaller crystallites, which would allow for decreased grain size. As well the possibility for more defects in the crystal structure as the rate of cooling is increased even further which might contribute to decreased thermal conductivity.

To test this hypothesis, two samples were prepared consisting of pure tin selenide with no dopants. The starting materials were BDH chemicals tin shot with 99.6 % purity, which was washed with HCl, and loaded into the glovebox, and Se shot from Central Research Laboratories 99.999 % purity which is also stored in the glovebox. After loading the quartz tubes with the tin and selenium in the appropriate ratios, the tubes of nominal compositions $Sn_{1.006}Se$ and $Sn_{1.002}Se$ were both melted at 1273 K for five hours. Then the $Sn_{1.006}Se$ tube was air-quenched by taking it out of the furnace at 1273 K and placing it onto a firebrick to rapidly cool down to room temperature. The $Sn_{1.002}Se$ tube was water-quenched by taking it out of the furnace at 1273 K and placing it into a bowl of water to cool down at an even higher rate. The samples were then taken into the glovebox opened and ground using the mortar and pestle until the particle size appeared consistent. Followed by loading into the ball mill jars and being ball milled for 5 cycles of 5 minutes at 600rpm with zirconium oxide ceramic balls in a 1:2 ratio respectively. Finally the samples were loaded into the graphite die and hot pressed with a ramp time of 60 minutes, a holding time of 480 minutes at 673 K and a pressure of 48 MPa.

The air quenched sample had a density of 6.06 g/cm^3 (98.1 %) and the water quenched sample had a density of 6.10 g/cm^3 (98.8 %).

The pellets were cut into discs for the thermal diffusivity measurement, and bars for the electrical conductivity and Seebeck coefficient measurements. For the thermal conductivity calculation, the Dulong-Petit method was used to estimate the heat capacity.

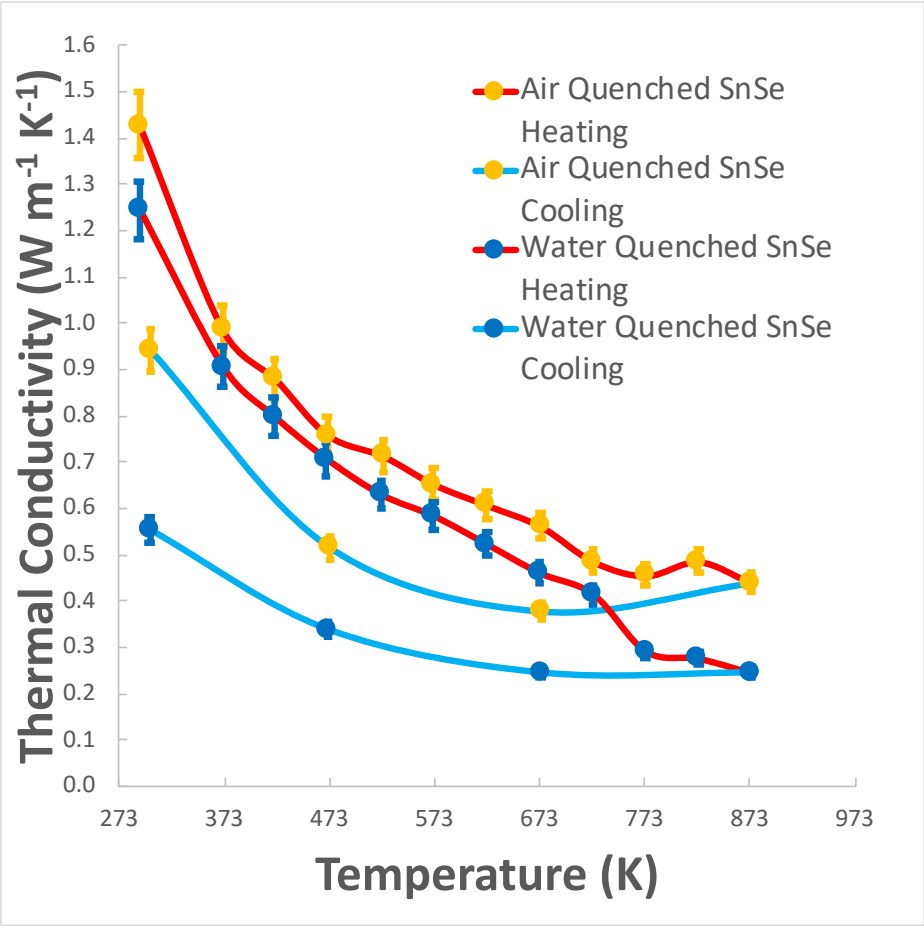

Figure 12. Total thermal conductivity of air-quenched and water-quenched tin selenide samples.

As seen in the above thermal conductivity measurement, during both the heating and cooling the water quenched sample had greatly reduced total thermal conductivity (K_{total}), averaging approximately 20 % lower throughout the whole measurement. However it was noted that the thermal conductivity significantly deviated from the heating to the cooling measurement.

A possible explanation was that as the samples reached the phase transition temperature near 800 K, the phase transition caused hysteresis of the thermal conductivity as well as grain growth due to the elevated temperature.[40,59]

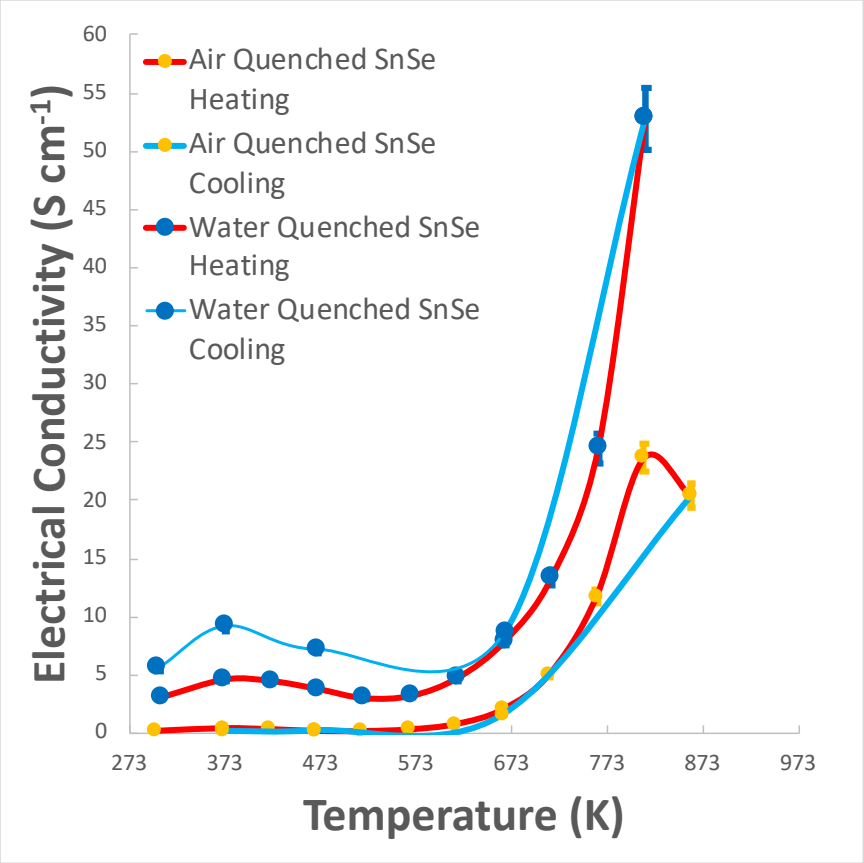

Figure 13. Electrical conductivity of air-quenched and water-quenched tin selenide samples.

Considering both samples were ball milled, and hot pressed at 673 K the grain size prior to the measurement was likely to have been on the nano scale, and the measurement temperature likely exceeded the maximum temperature at which the samples would've had ideal repeatability.

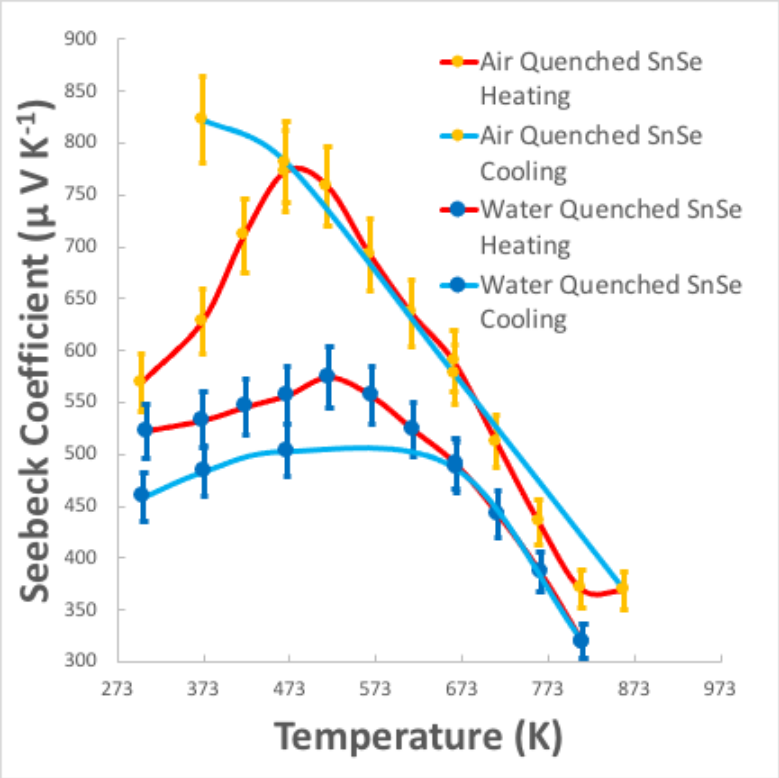

Figure 14. Seebeck coefficients of air-quenched and water-quenched tin selenide samples.

Both the electrical conductivity and Seebeck coefficients were also affected greatly by the cooling method used after the melt process. The electrical conductivity was significantly increased by water quenching, and the Seebeck coefficient was correspondingly reduced by water quenching.

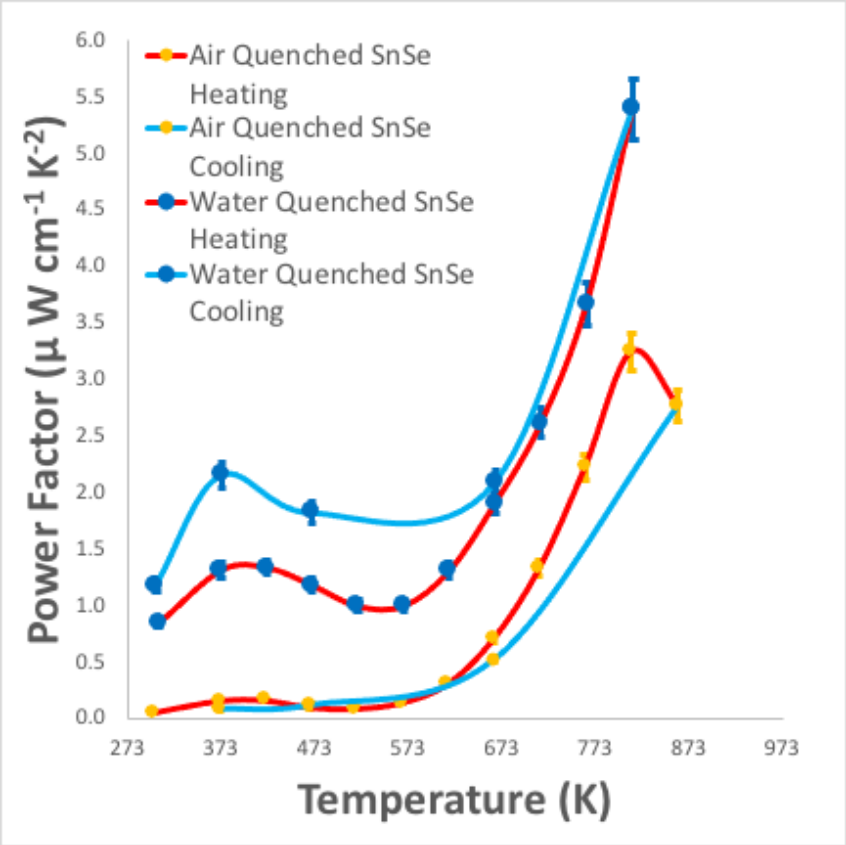

Figure 15. Power Factors of the air-quenched and water-quenched samples

However it is important to note that the increased electrical conductivity more than made up for the reduced Seebeck coefficient as can be seen in the Power Factor (PF), where the water quenched sample achieved a maximum of 5.4 µW cm^{-1} K^{-2} and the air quenched sample only reached a maximum of 3.25 µW cm^{-1} K^{-2} .

Considering the reduced total thermal conductivity of the water quenched sample with the enhanced electrical conductivity, the lattice thermal conductivity must have been significantly decreased by the water quenching cooling method when compared to the air quenching method.

Together the enhanced power factor and reduced total thermal conductivity significantly increased the maximum and average *zT* of the water quenched tin selenide sample (1.58 vs 0.61 peak *zT* respectively). Figure 16 shows this, significantly improved average *zT* starting from room temperature and much higher peak *zT* of the water quenched tin selenide sample. This suggests that future polycrystalline tin selenide samples would also benefit from increased cooling rates after the melting synthesis.

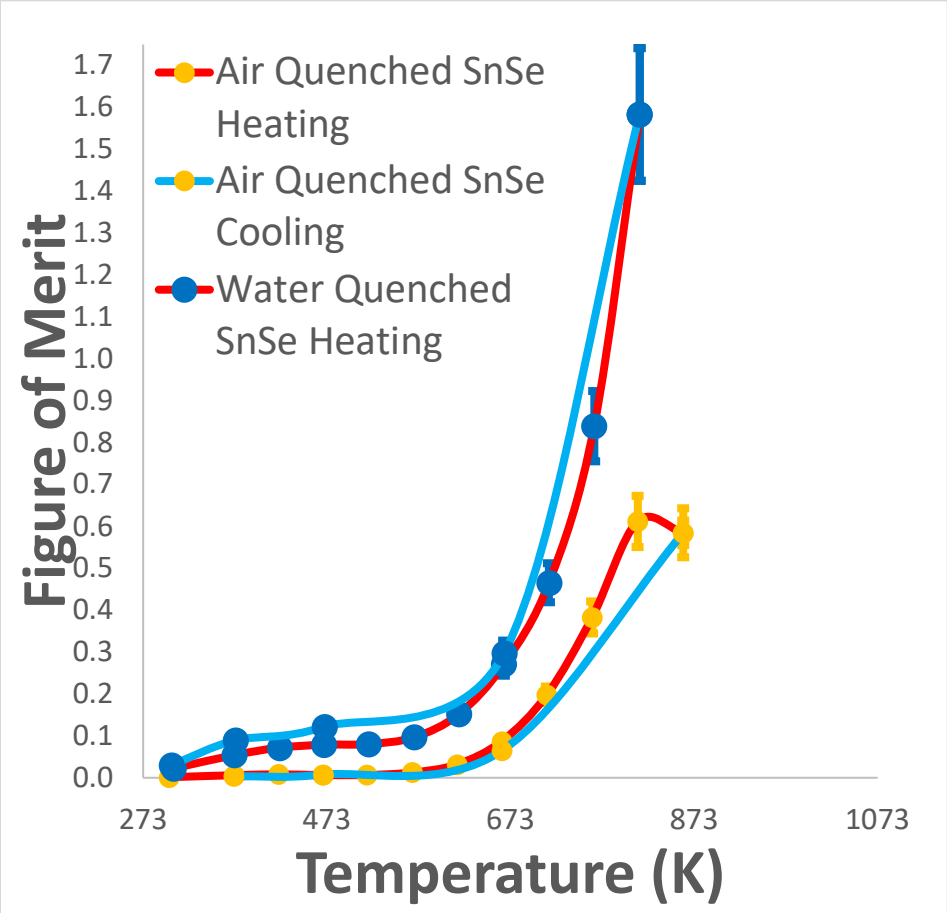

Figure 16. Figure of Merit of the water-quenched tin selenide is significantly greater than the air-quenched sample.

2.3.2 Hot Pressing compared to Spark Plasma Sintering

One of the next concerns was that many of the top papers reporting high *zT* results for tin selenide samples use the spark plasma sintering (SPS) process rather than conventional hot pressing (HP). The proposed benefits of spark plasma sintering is a reduced time for heating, lower temperatures, reduced grain size, and higher density. Supposedly the spark plasma sintering process heats the sample more effectively as the sample itself generates the heat rather than the heat coming from the exterior heating elements in a hot press. However if it is possible to hot press tin selenide samples with reduced holding time, and still achieve comparable density to the SPS samples then this would be beneficial because hot press methods are cheaper, and more reliable. Therefore in an industrial or consumer application hot pressing will be the more likely method used for manufacturing of thermoelectric materials when compared to spark plasma sintering.

First a series of samples was prepared starting from the same starting materials and same melt to ensure comparability in the results, as the compositions would be identical, as well as any amount of oxides present would also be the same between different samples. The tin metal used was the BDH chemicals 99.6 % purity tin which was acid washed with HCl, and subjected to the melt-purification process. Se was aquired from Central Research Laboratories 99.999 % purity, Ag 99.9 % from Alfa Aesar, Cu 99.9 % from Alfa Aesar, and Na 99.8 % from Thermo Fisher Scientific.

Reducing the time of hot pressing was the main objective, as this would allow for a sintering process that is more similar to the SPS methods used for the top performing samples.

Four samples were prepared from two melts, two samples with the composition $Na_{0.01}Cu_{0.01}Sn_{0.98}Se$, and two $Na_{0.01}Ag_{0.01}Sn_{0.98}Se$. From each pair, one was hot pressed, and one was spark plasma sintered.

Experiments with further reduced hot pressing time were also completed successfully, using two samples with the composition Na0.01Cu0.01Sn0.98Se: after hot pressing both samples reduced ramping time and holding time, high density (>99%) was achieved. reduced

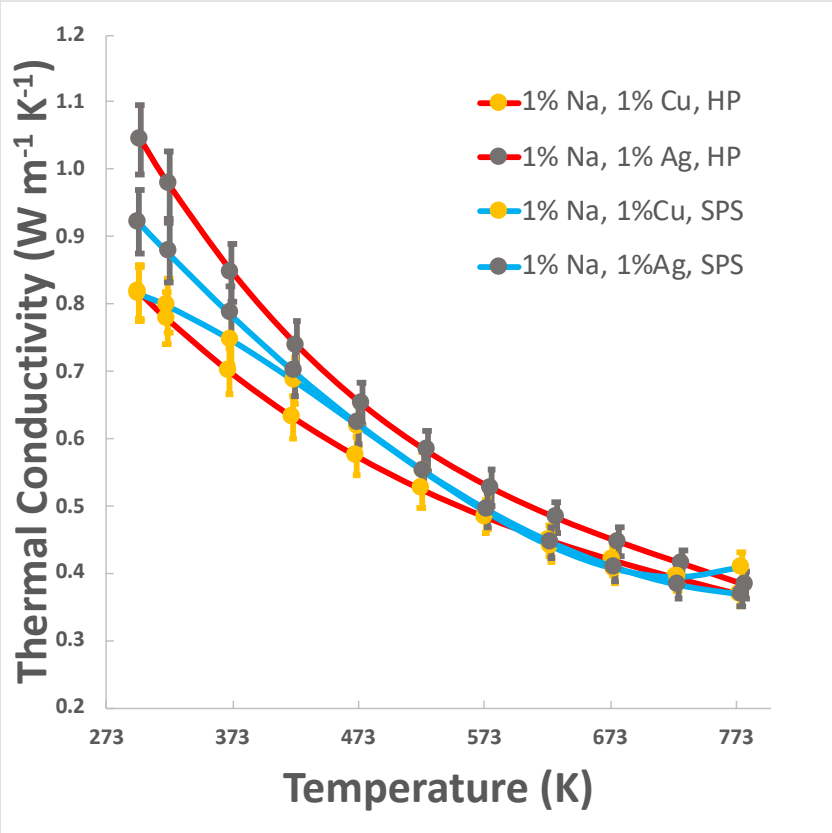

Figure 17. Total thermal conductivity of SPS vs HP Na/Cu double doped tin selenide samples.

From Figure 17, the Cu doped samples exhibited lower total thermal conductivity compared to the Ag doped samples, however there was no clear trend for whether the hot pressing or the spark plasma sintering led to lower total thermal conductivity since the Cu doped sample

exhibited increased thermal conductivity when SPS was used, and the Ag doped sample had decreased thermal conductivity when hot pressed.

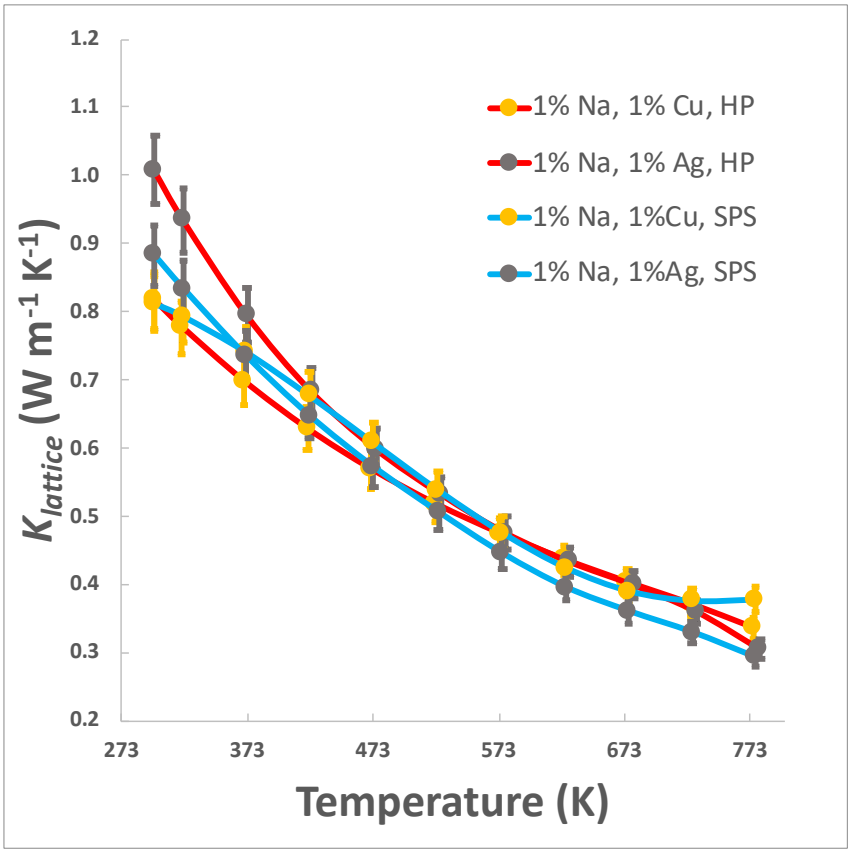

Figure 18. Lattice thermal conductivity of SPS and HP Na/Cu and Na/Ag doped tin selenide samples.

Comparing the lattice thermal conductivity,a very slight reduction in lattice thermal conductivity for both HP samples in the temperature range of 576 K – 726 K as shown in Figure 18. However the difference is minimal and not reflected at other temperatures.

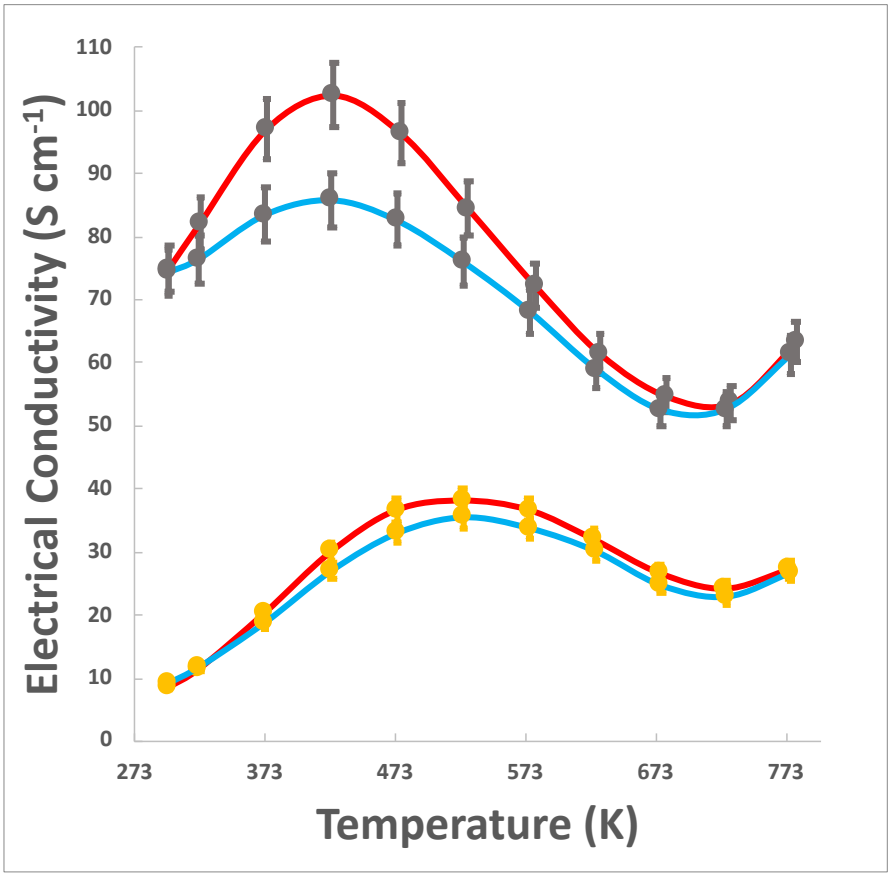

Figure 19. Electrical conductivity of SPS and HP Na/Cu and Na/Ag doped samples.

When comparing the electrical conductivity, the SPS samples show a very small reduction in electrical conductivity throughout the whole temperature range tested, with the largest difference occurring at the peak electrical conductivity for both the Na/Cu, and Na/Ag doped samples. The Ag double doped sample also shows a much greater electrical conductivity than the Cu double doped sample. All 4 samples showed the characteristic electrical conductivity trend for heavily doped SnSe samples, where at low temperatures they behaved as semiconductors with increasing conductivity as temperature increased, followed by a peak where the charge carrier mobility is maximized, and afterwards a metallic behaviour as the

dopant generated charge carrier mobility reduced, and finally thermal activation with the peak temperature and phase change leading to a small increase near 773 K.

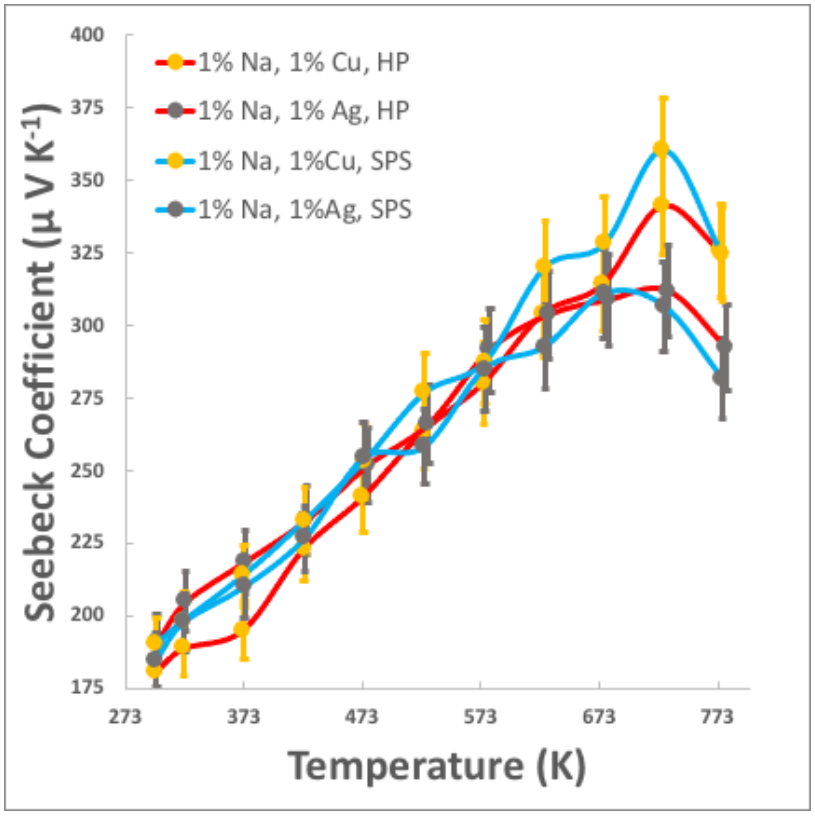

Figure 20. Seebeck coefficients of SPS vs HP, Na/Cu, and Na/Ag double doped tin selenide.

From Figure 20, it is clear the Seebeck coefficients were not significantly affected by the SPS or HP method. An interesting note is that both the Cu and Ag doped samples exhibit similar Seebeck coefficients throughout most of the temperature range despite the significant improvement in electrical conductivity for the Ag doped sample. This shows the doping efficiency of Ag in this system when using this particular sample preparation method is higher than that of Cu. The only significant difference occurring at the maximum temperature from 726-773 K where the Cu doped sample has a slightly higher Seebeck coefficient.

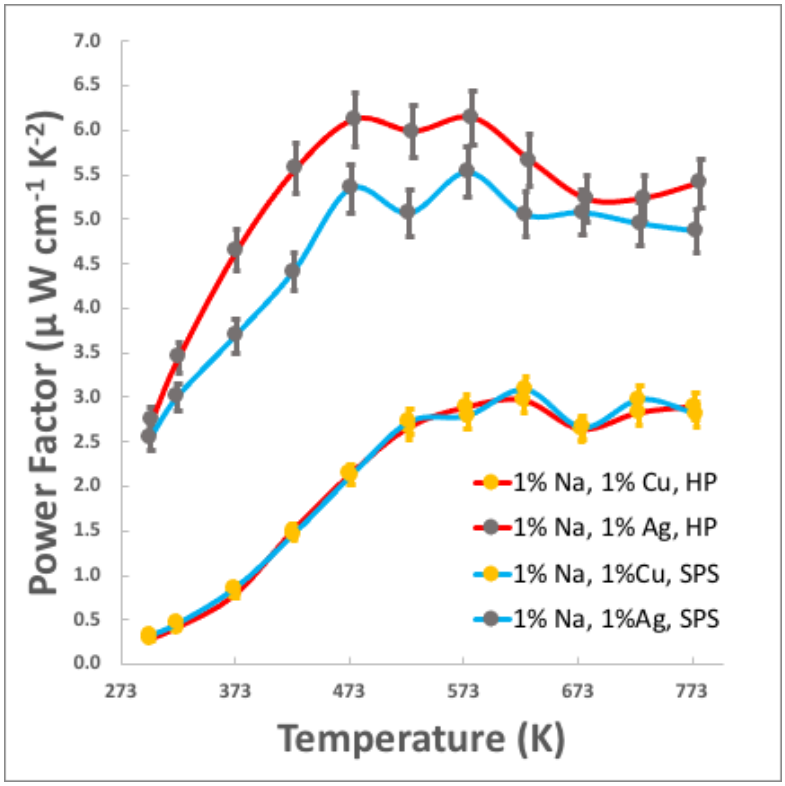

Figure 21. Power factor (PF) of SPS vs HP, Na/Cu, and Na/Ag double doped tin selenide.

In Figure 21. The overall effect of SPS on the electrical properties is shown through the power factor (PF), where the Na/Cu sample showed no effect, and the Na/Ag sample shows an increased power factor from hot pressing with the reduced time compared to the SPS method.

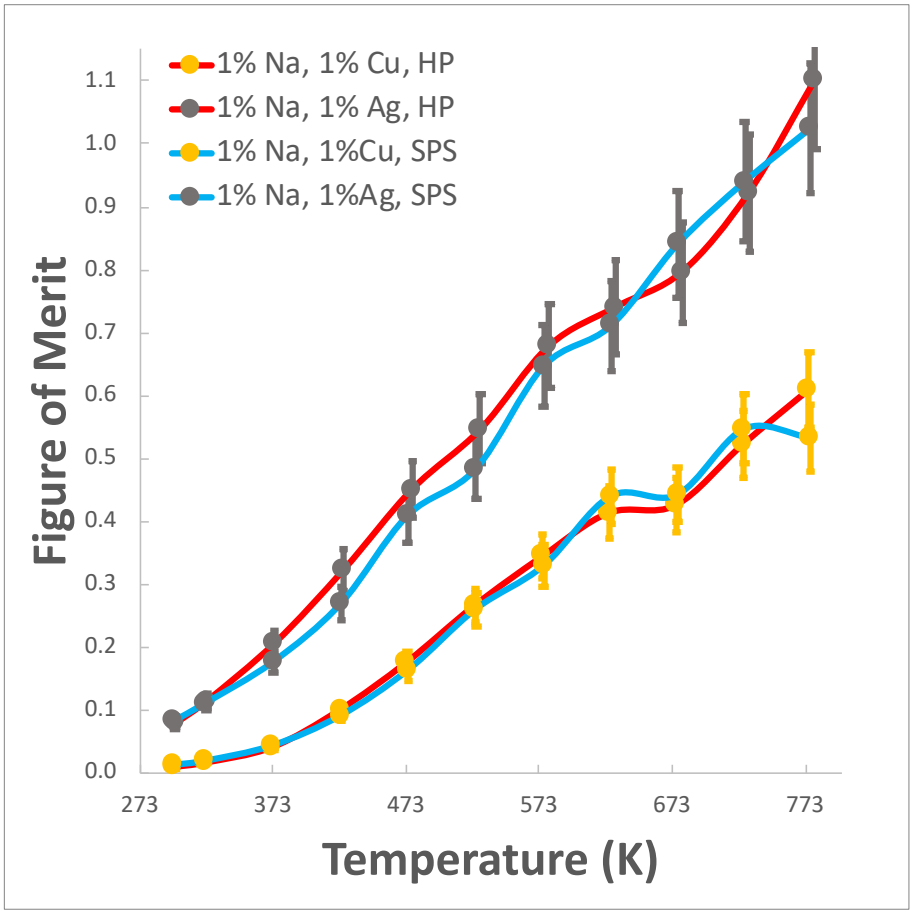

Figure 22. Figure of Merit (*zT*) of SPS vs HP, Na/Cu, and Na/Ag double doped tin selenide.

Despite the increased PF from the HP method used for the Na/Ag sample, the *zT* was not changed by either of the sintering methods due to the correspondingly affected thermal conductivity of the Na/Ag sample.

In conclusion, when adjusted effectively the HP method is just as effective for sintering tin selenide thermoelectric pellets as the SPS method despite previous claims that SPS sintering is much better than HP sintering.[1] Reducing the HP holding time is important to realizing this, as for materials which can be sintered at a high enough temperature, the holding temperature is more significantly associated with the density than the holding time.

Conventionally HP methods may use times of 6-24 hours at temperature, not only is this possibly causing grain growth, but it is also not time effective or power usage effective when compared to shorter holding times. In Figure 23, further reduced HP times were tested for high density, and subsequently the total thermal conductivity. Both the 30 minute and 15 minute holding times were effective in achieving high density of the samples.

However it must be noted, reducing the ramping time and the holding time too much will reach a point where the sintering is not as effective. Although this point was not reached in the course of this thesis project, reducing the ramping time to 773 K below 20 minutes, and the holding time below 5 minutes is not recommended due to both the output power used for the HP, and the possibility that the heat of the sample is does not reach the full temperature when ramped for such a short time. The HP thermocouples are not located within the sample, so the actual temperature of the sample may be lower than expected if the times used are reduced too far.

Through further reduced HP times, as shown in Figure 23, the thermal conductivity was shown to have been slightly reduced, likely due to less grain growth.

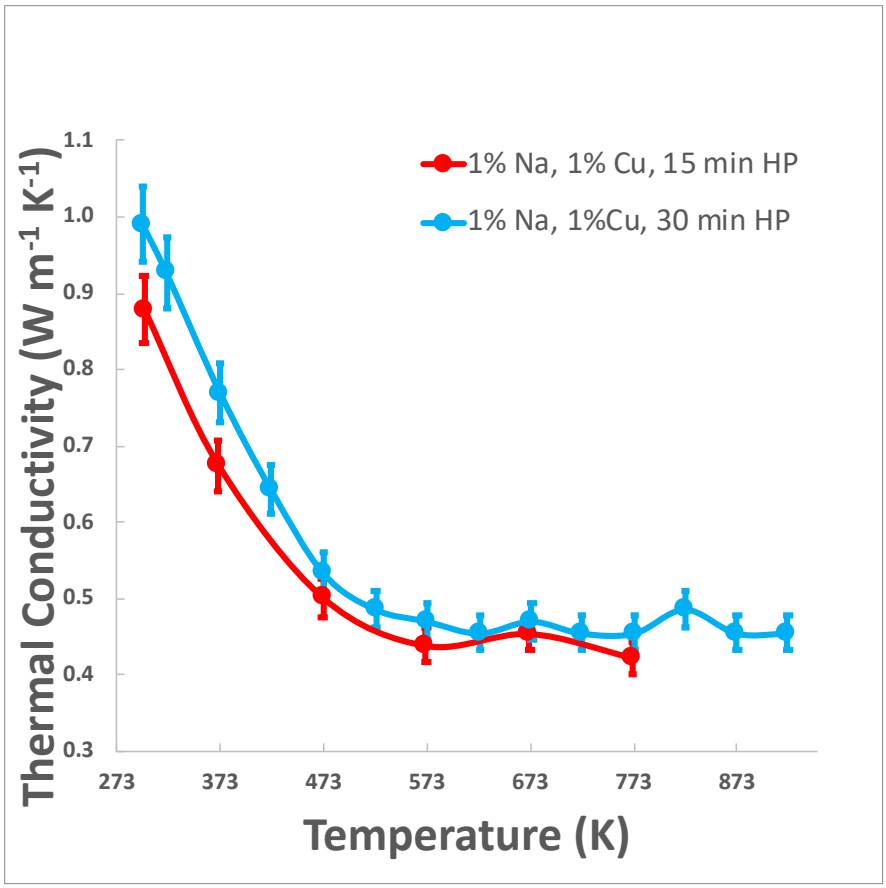

Figure 23. Comparison, of total thermal conductivity of 30 minute and 15 minute holding time for HP Na/Cu double doped tin selenide samples.

Although the electrical conductivity was reduced by the reduced HP holding time, the Seebeck coefficient was improved enough to counteract this, resulting in very similar power factors between the 15 minute HP sample and the 30 minute HP sample. Even though the 15 minute HP sample had its ZEM measurements taken in December 2022, and the ZEM instrument was down from March 2022 until August 2022, the room temperature air exposure to the sintered 15 minute sample did not seem to significantly affect the properties negatively.

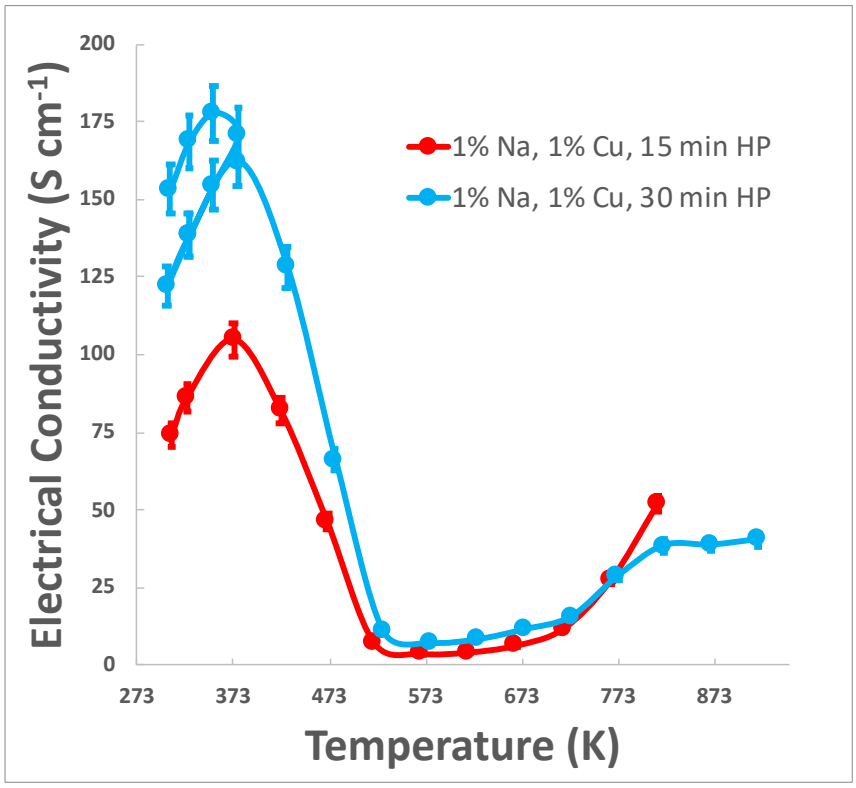

Figure 24. Electrical conductivity of 15 min and 30 min HP Na/Cu doped samples.

Ultimately, the reduced hot press times resulted in significantly reduced thermal conductivity, as well as a slight improvement in power factor due to an improved Seebeck coefficient as seen in Figures 23-26, resulting in an improved figure of merit at most temperatures (Figure 27).

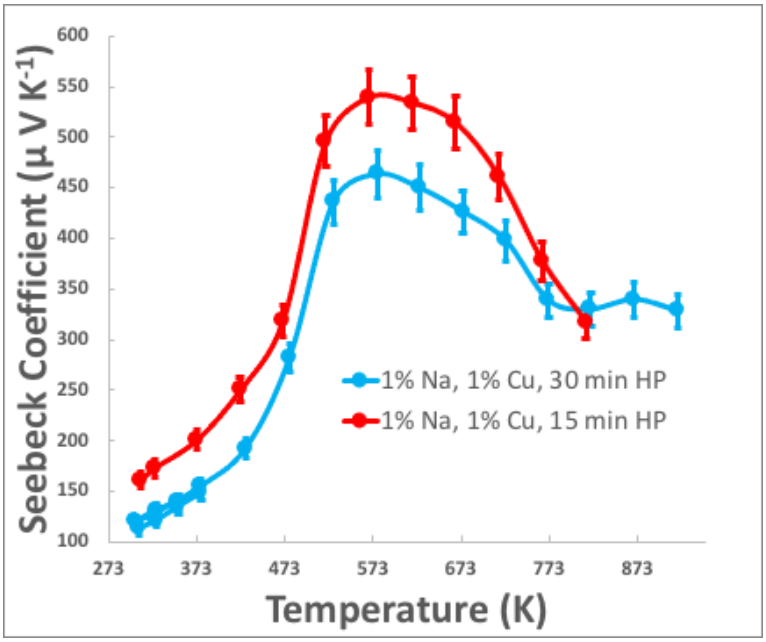

Figure 25. Seebeck coefficients of 15 min and 30 min HP Na/Cu doped samples, with the 15 minute HP sample exhibiting significantly improved Seebeck coefficient.

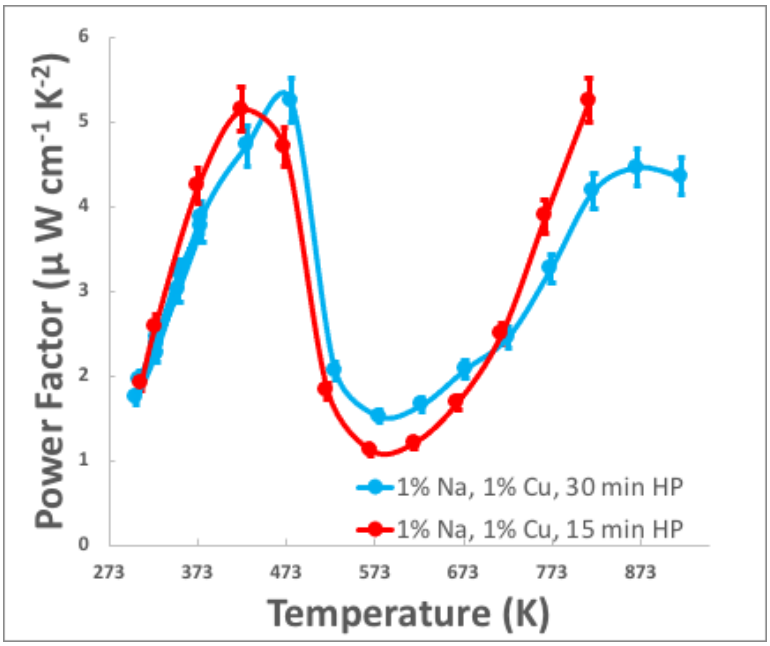

Figure 26. Power Factors of 15 min and 30 min HP Na/Cu doped samples, with the 15 minute HP sample exhibiting a slight increase in PF at low temperatures, and at very high temperatures.

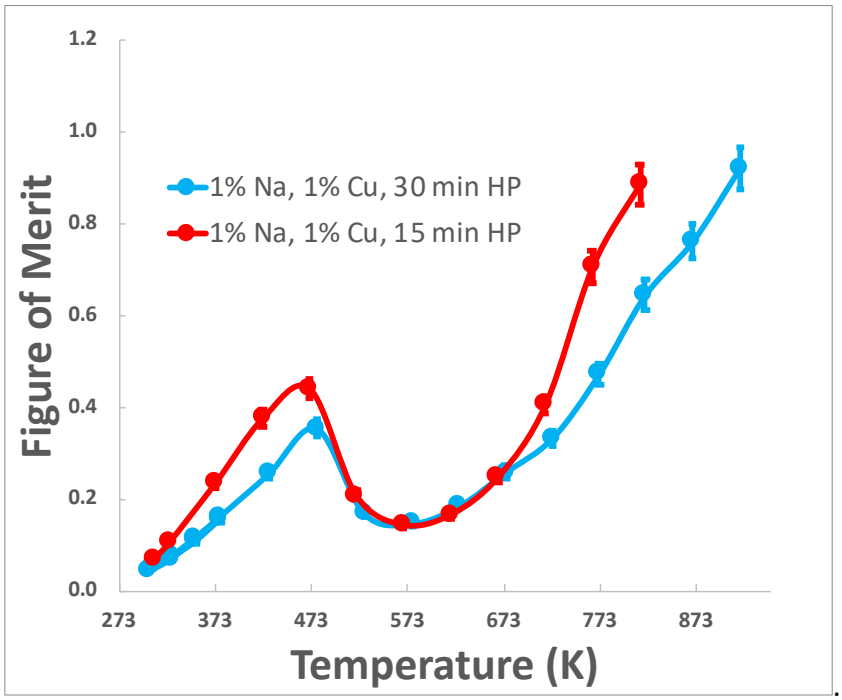

Figure 27. Figure of Merit (*zT*) of 15 min and 30 min HP Na/Cu doped samples, with the 15 minute HP sample exhibiting an increased *zT* throughout the entire temperature range.

With the hot press testing results, the method used for sintering chosen for the rest of the project was HP with a significantly shorter holding time than conventionally used (reduced from 6-24 hours to 5-30 minutes.

Chapter 3: Double Doping *p*-type Optimization

3.1 Procedure

Tin metal was prepared from the BDH chemicals tin shot, by washing with HCl, followed by the melting purification procedure described in section 2.1. The tin was brought into the glovebox and weighed out along with the Se from Central Research Laboratories 99.999 % purity, Cu 99.9 % from Alfa Aesar, and Na 99.8 % from Thermo Fisher Scientific into quartz tubes. Twenty 3g samples were weighed out with compositions ranging within ($0<x<0.033$, $0<y<0.016$) for the set of samples 1A-20A, $Na_xCu_ySn_{1-x-y}Se$. The quartz tubes were subsequently evacuated, and sealed. Melting was completed for 18-20 hours at 1273 K, followed by cooling in air. Air cooling was chosen despite the prior found benefit of water quenching because of the number of samples being prepared, and the risk for tube breakage increasing when water quenching.

After cooling, the samples were reheated to 773 K and annealed for 48 hours. Then the samples were ground with the mortar and pestle until uniform inside the glovebox, followed by the reduction process, between 673 K and 773 K for 18 hours. After grinding the samples a second time, they were hot pressed with a ramping time of 20-30 minutes to 773 K and a holding time of 5-10 minutes with a pressure of 48 MPa. All of the samples achieved densities greater than 96 %, except for samples 19A ($Na_{0.0125}Cu_{0.002}Sn_{0.9855}Se$), and 20A ($Na_{0.03}Cu_{0.008}Sn_{0.962}Se$) which only reached 92 % and 93 % respectively.

From each of the pellets produced, a disc and two bars were cut out, for the thermal diffusivity measurement, as well as the electrical and Seebeck coefficient determination. Selected samples with notable properties were also analyzed on SEM.

3.2 Thermal conductivity

The total thermal conductivity was calculated from the thermal diffusivity using the Dulong-Petit method for all 20 samples, followed by calculating the electrical contribution to the thermal conductivity from the Wiedemann-Franz law using the Lorenz number calculated from the Seebeck coefficient as shown in Equation 1-6. Error bars were not included in this chapter to ensure legibility of the figures.

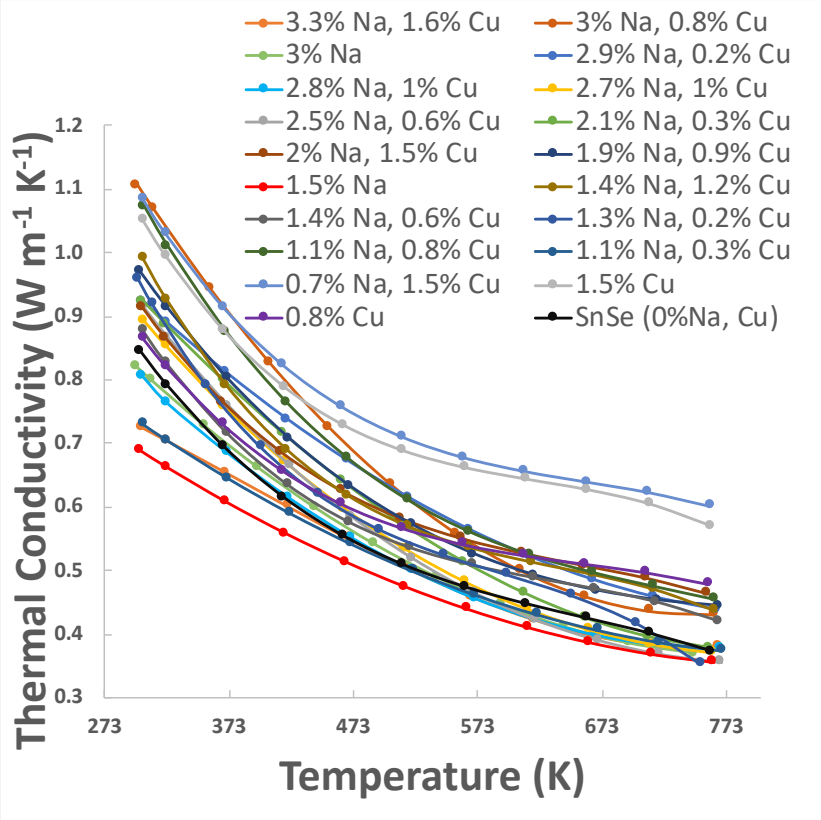

Figure 28. Total thermal conductivity of Na/Cu doped samples.

As shown in Figure 28, the expected decreasing total thermal conductivity of *p*-type tin selenide samples was seen for all of the samples. Notably, the two samples with the highest Cu content relative to their Na content with the compositions $Na_{0.007}Cu_{0.015}Sn_{0.977}Se$, and

$Cu_{0.015}Sn_{0.985}Se$, both had highly increased total thermal conductivity throughout the whole temperature range. The three samples with the lowest total thermal conductivity were all doped with Na, and had less Cu than Na, with the compositions $Na_{0.015}Sn_{0.985}Se$, $Na_{0.033}Cu_{0.016}Sn_{0.961}Se$, and $Na_{0.011}Cu_{0.003}Sn_{0.99}Se$.

Another interesting trend is as the temperature increases to the maximum recorded, the total thermal conductivity formed into three groups of samples, with two samples having a high thermal conductivity and also having high Cu content, a group of medium thermal conductivity and correspondingly average levels of Na, and Cu, and finally a low thermal conductivity group with high amounts of Na. Despite the starting room temperature thermal conductivity for some samples being relatively high, as the temperature increased the trend of reducing total thermal conductivity was high enough in those samples they could be in the lower range of resulting total thermal conductivity. The lattice thermal conductivity (Figure 29) shows this stratification of high temperature thermal conductivity to a higher degree: samples with lower Na/Cu ratios were more likely to have higher lattice thermal conductivity. A notable exception is the sample of nominal composition Na0.033Cu0.016Sn0.961Se, which had the lowest lattice thermal conductivity in the range from 322 K up to 564 K, and a lowest lattice thermal conductivity at 766 K of 0.336 W m^{-1} K^{-1} . This sample had the highest amount of Na, as well as the highest amount of Cu. Considering some of the other samples results such as $Na_{0.02}Cu_{0.015}Sn_{0.965}Se$ which ended up having the fourth highest lattice thermal conductivity at 758 K of 0.44 W m^{-1} K^{-1}, it is reasonable to conclude that the increasing Na content greatly reduces the lattice thermal conductivity, as well as that when not balanced with the addition of Na, the Cu doped samples found

increased lattice thermal conductivity compared to the undoped samples. It may be reasonable to also conclude that it is specific to the synthesis process used, as a prior paper using solvothermal synthesis found decreased total thermal conductivity with increasing Cu doping up to 11 %.[54] Considering the results from that paper along with the results found here, it is likely that copper selenide formed during the synthesis in extremely small quantities, however enough to increase the lattice thermal conductivity significantly.

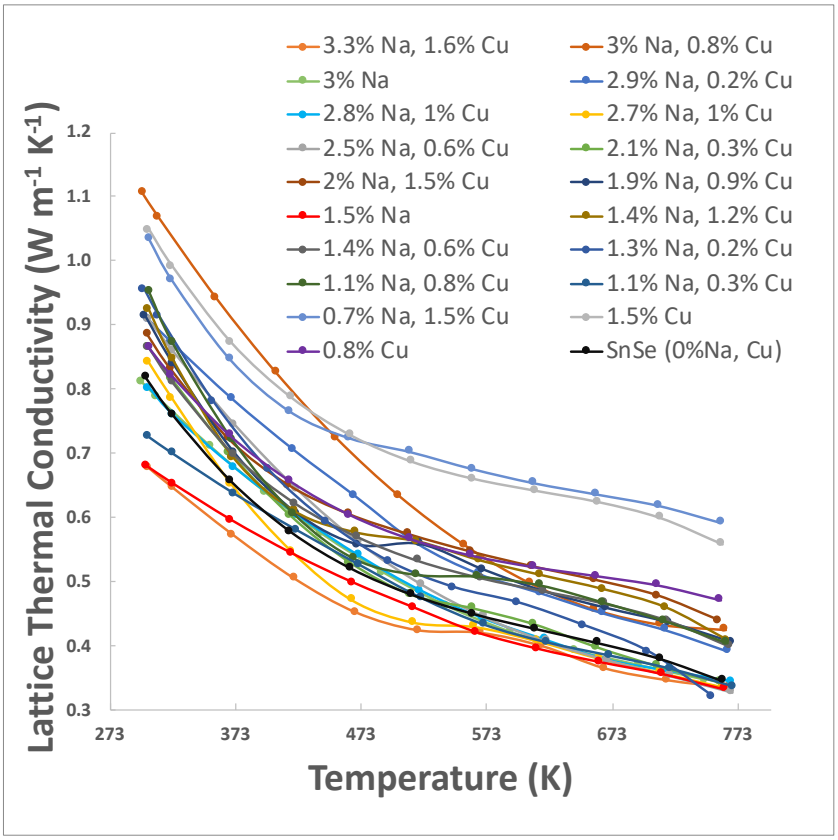

Figure 29. Lattice thermal conductivity of Na/Cu doped samples.

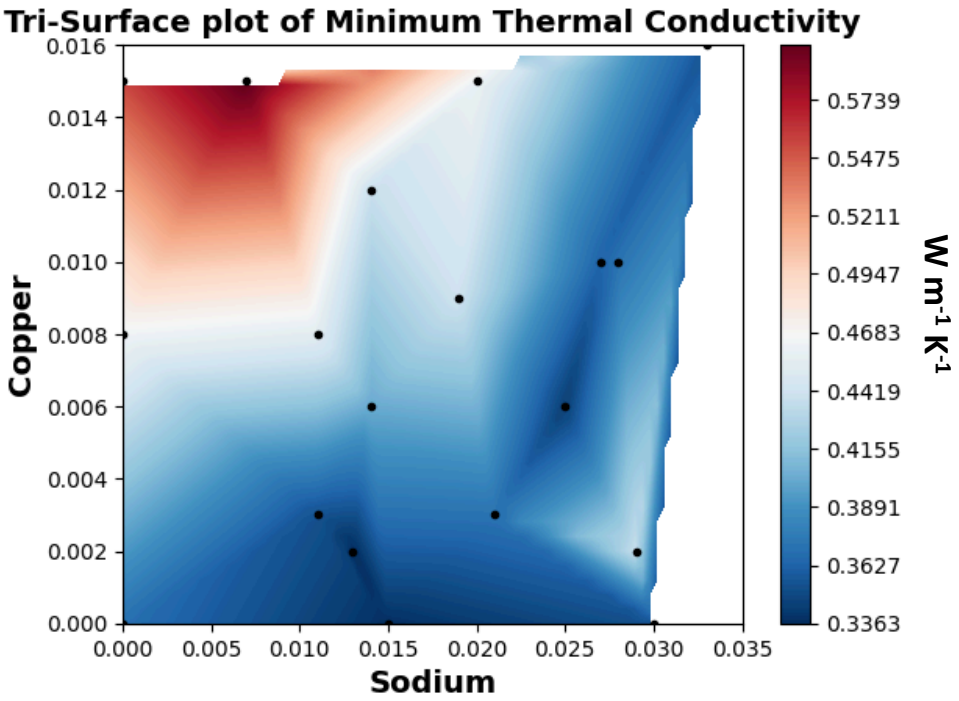

Figure 30. Linear triangular interpolation surface plot of the lowest thermal conductivity point for each sample plotted versus Na and Cu content.

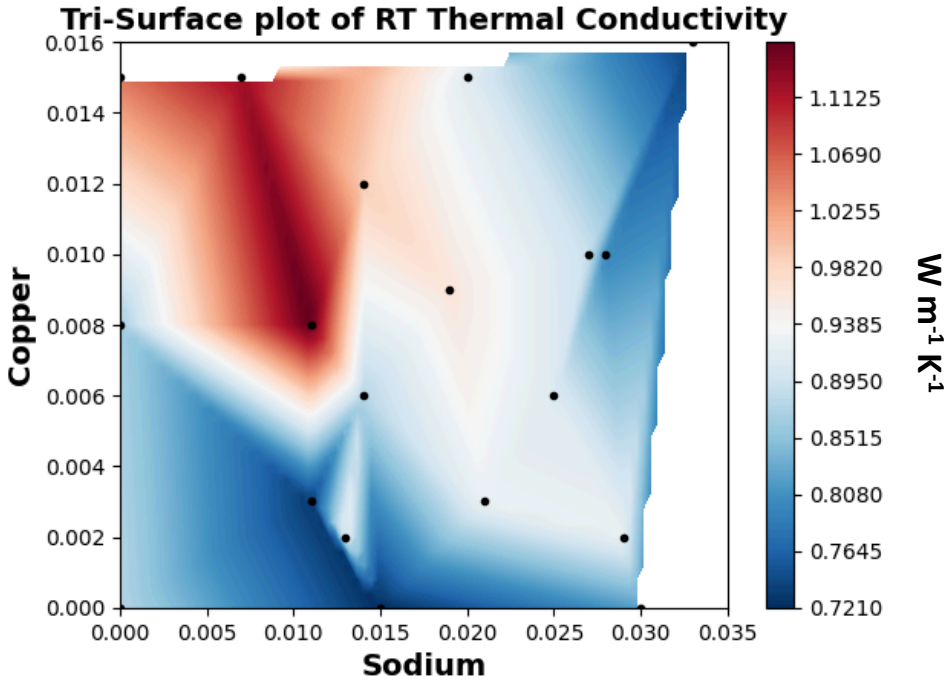

Figure 31. Linear triangular interpolation surface plot of the highest thermal conductivity point for each sample plotted versus Na and Cu content.

Using a linear triangular interpolation, the key properties of each sample were plotted relative to the Na, and Cu content of each sample. Comparing the thermal conductivity surface plots in Figures 30, 31, 32 shows the trend for increasing lattice thermal conductivity with increasing Cu when not paired with increasing Na content. At room temperature in Figure 31, the standout feature is the large peak at 0.8% Cu, however this is due to the high electrical conductivity of that particular sample, and when comparing with the minimum lattice thermal conductivity surface plot, this feature is removed. It is also interesting to note that with the increasing Na content, the amount of Cu that can be added without negatively impacting the lattice thermal conductivity increases as well.

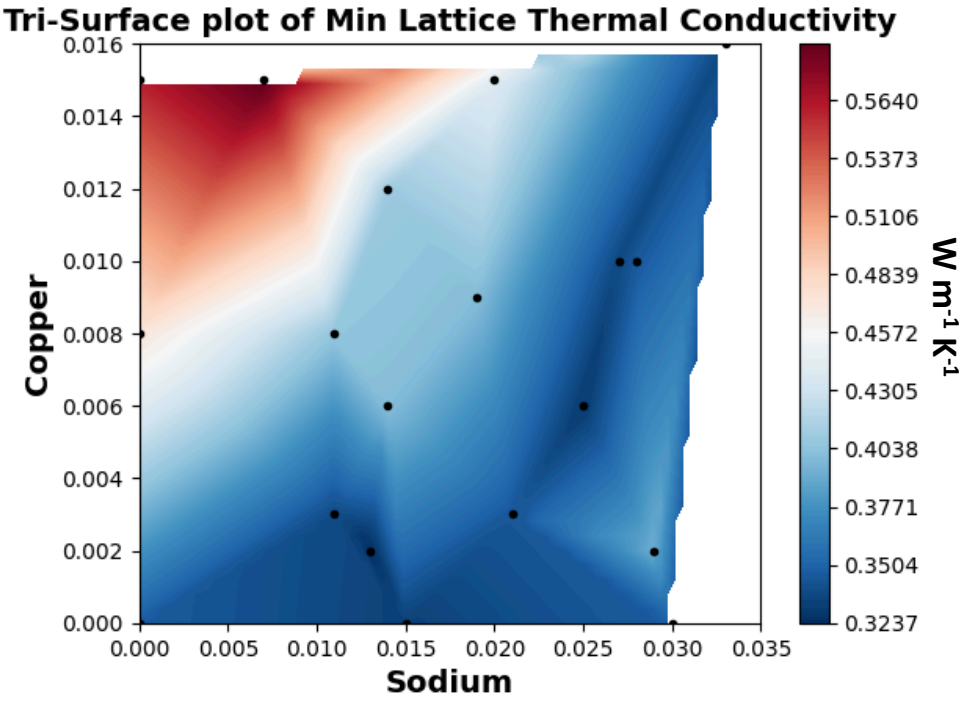

Figure 32. Linear triangular interpolation surface plot of the lowest lattice thermal conductivity point for each sample plotted versus Na and Cu content.

When looking further into the data in Figure 33, with the density plot, the trend for density follows as well with increasing Na reducing the density. The one sample with low density at 0.2% Cu, 1.3% Na is apparent in the density plot, however it did not seem to significantly affect the other plots results.

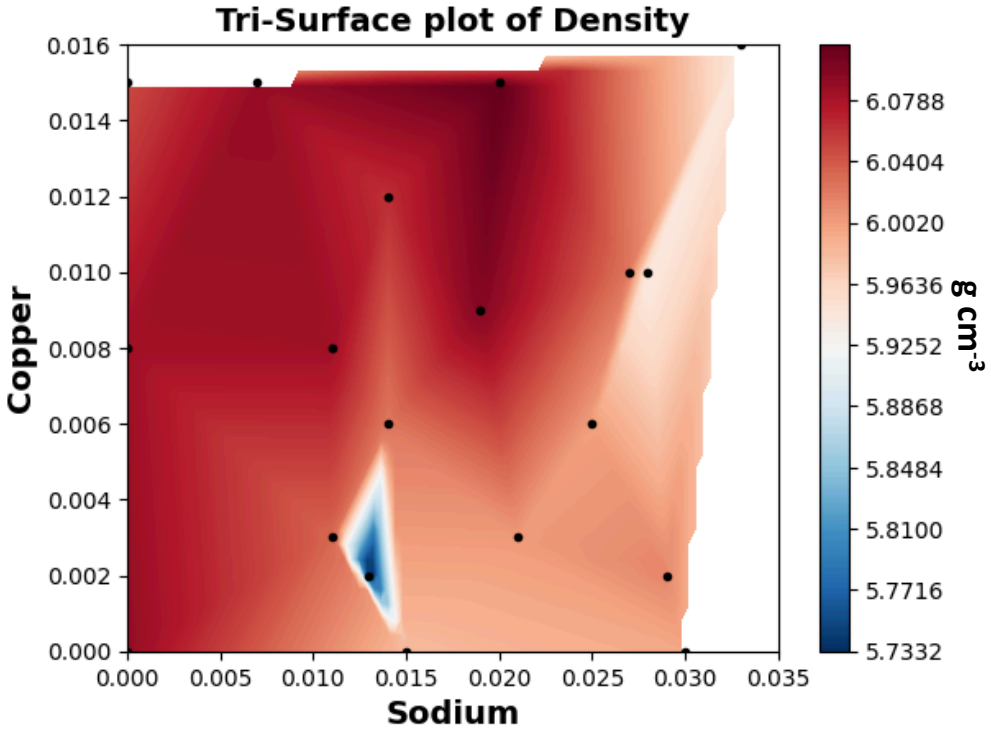

Figure 33. Linear triangular interpolation surface plot of the density for each sample plotted versus Na and Cu content.

3.3 Seebeck Coefficient, Electrical Conductivity, Power Factor

Using the Ulvac ZEM instrument, all 20 *p*-type samples were analyzed from room temperature (RT) up to 773 K for the Seebeck coefficient and electrical conductivity.

Plotted below is the electrical conductivity during the first heating cycle (Figure 34), followed by the electrical conductivity during cooling (Figure 35).

Doping with Na and Cu increased the electrical conductivity in the lower temperature range between RT and up to approximately 573 K significantly as expected due to the increased carrier concentration. However this effect was seemingly inconsistent despite meticulous preparation of samples, as for example the sample with the doping of 3 % Na, and 0.8 % Cu had a lower electrical conductivity than the sample doped with 0.8 %

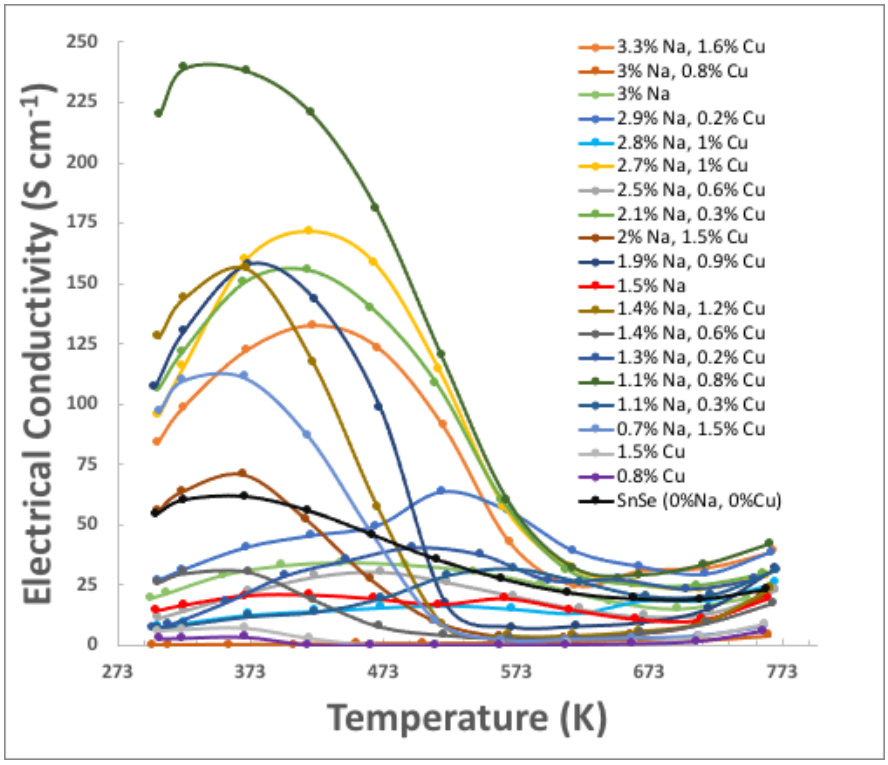

Figure 34. Electrical Conductivity of Na/Cu doped samples on first heating cycle.

Cu, while the sample with 3.3 % Na, and 1.6 % Cu had an electrical conductivity almost 100x higher than either of the two previously mentioned. Some possible explanations for this inconsistency are:

The tin metal used for preparation had inconsistent amounts of oxides present, since samples 1A-14A were prepared from one batch of tin, and samples 15A-20A were prepared from a second batch of tin, this explanation may have some power as one of the unexpectedly poorly performing samples was from the second batch of tin (15A-20A) which had the samples with the compositions; $Cu_{0.015}Sn_{0.985}Se$, $Cu_{0.007}Sn_{0.992}Se$, $Na_{0.015}Sn_{0.985}Se$, $Na_{0.03}Sn_{0.97}Se$, $Na_{0.013}Cu_{0.002}Sn_{0.986}Se$, $Na_{0.03}Cu_{0.008}Sn_{0.962}Se$. However this explanation is not

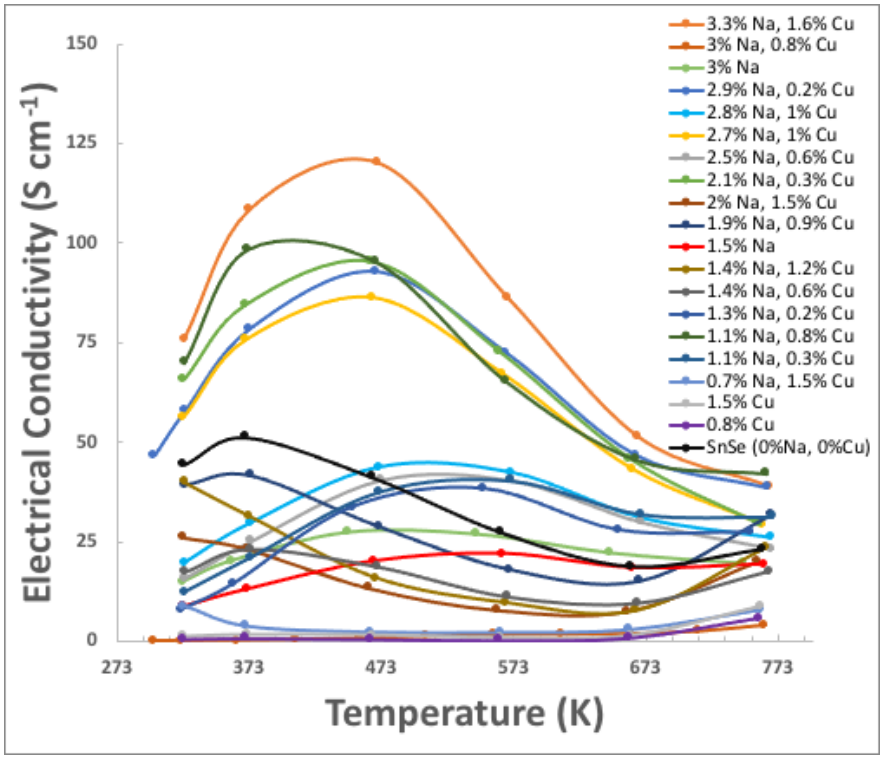

Figure 35. Electrical Conductivity of Na/Cu doped samples during cooling.

very strong since only the one sample $Na_{0.03}Cu_{0.008}Sn_{0.962}Se$, is unusually low performance compared to the other samples of similar compositions.

Another possibility is that the exact temperature during the reduction process was not the same for all of the samples, as they were sequentially loaded into the reduction oven in batches of up to 6 samples, it is possible the reducing environment of the samples was not exactly the same throughout the process due to uneven heat distribution, as well as the hydrogen gas flow having reacted with the samples which it comes into contact with first.

Since measuring the exact temperature with an additional thermocouple located within the reduction oven, the variation in temperature between the different sample positions is negligible, ranging up to 15 K maximum difference when the reducing temperature is 773 K.

One of the last possible explanations is an inconsistency in the mortar and pestle grinding process before hot pressing, which may have influenced the grain size of the samples, and is subject to human error.

Additionally, the reactivity of the Cu to form copper selenide rather than successfully doping in the tin site, may have had some inconsistency from sample to sample. In general it was the samples with higher Cu levels without additional sodium which had poor electrical conductivity.

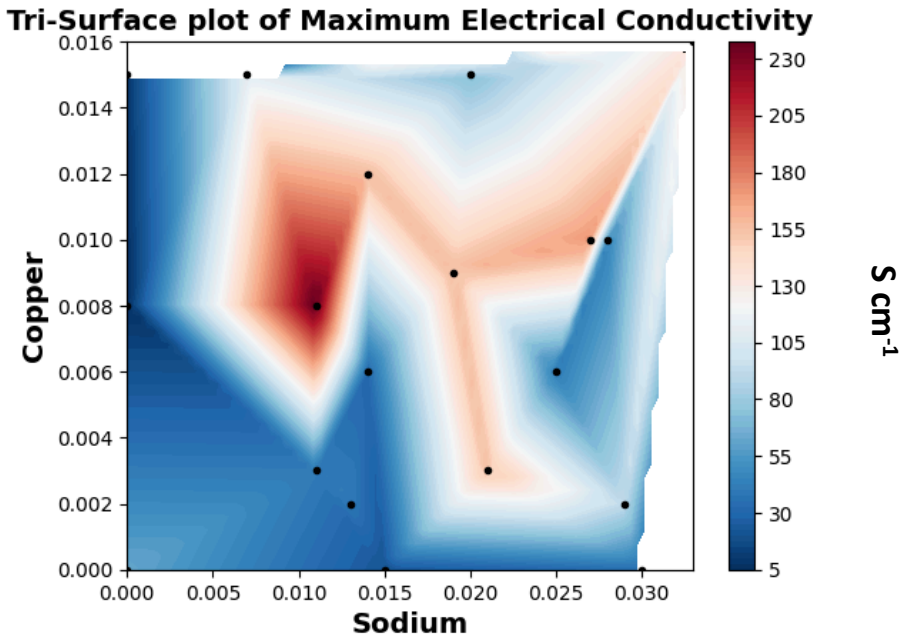

Figure 36. Linear triangular interpolation surface plot of the maximum electrical conductivity for each sample plotted versus Na and Cu content.

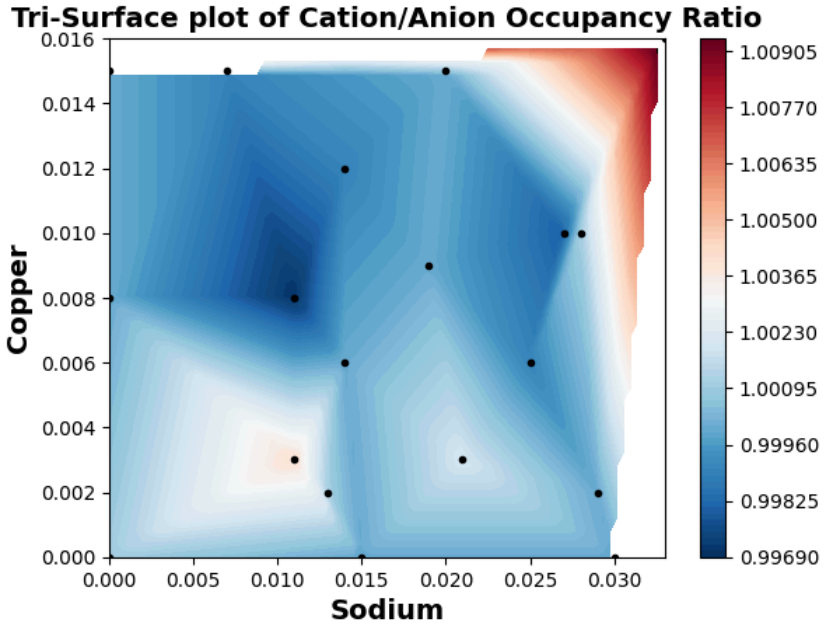

Figure 37. Linear triangular interpolation surface plot of the cation/anion ratio for each sample plotted versus Na and Cu content.

When looking at the peak electrical conductivity however, increasing Cu content is not a clear negative, rather when balanced with Na, the peak conductivity is increased compared to only increasing Na or only increasing Cu. Another possibility for error in the results is the ratio of the cation to anions, in Figure 37, it was calculated by the molar ratio of the sum of the cations weighed out (Na, Cu, Sn) divided by the Se content. The deviation from 1 is very small with a range of approximately 0.997-1.009. The sample with the highest electrical conductivity ($Na_{0.011}Cu_{0.008}Sn_{0.978}Se$) did have an unusually low relative ratio compared to the other samples at 0.997. It is possible this very slight excess of Se increased the effective *p*-type carrier concentration of holes to increase the electrical conductivity significantly. The other extreme sample with a ratio of approximately 1.009, $Na_{0.033}Cu_{0.016}Sn_{0.96}Se$ however also had one of the highest electrical conductivities, and during the cooling cycle had the most consistent electrical conductivity; enough to make it the most electrically conductive during cooling. It is possible there is a very small loss of Se or some instability during the maximum temperature of the measurement, as well as oxidation during the ZEM measurement. Either of these two factors may have not affected samples with a slight Se deficiency as much.

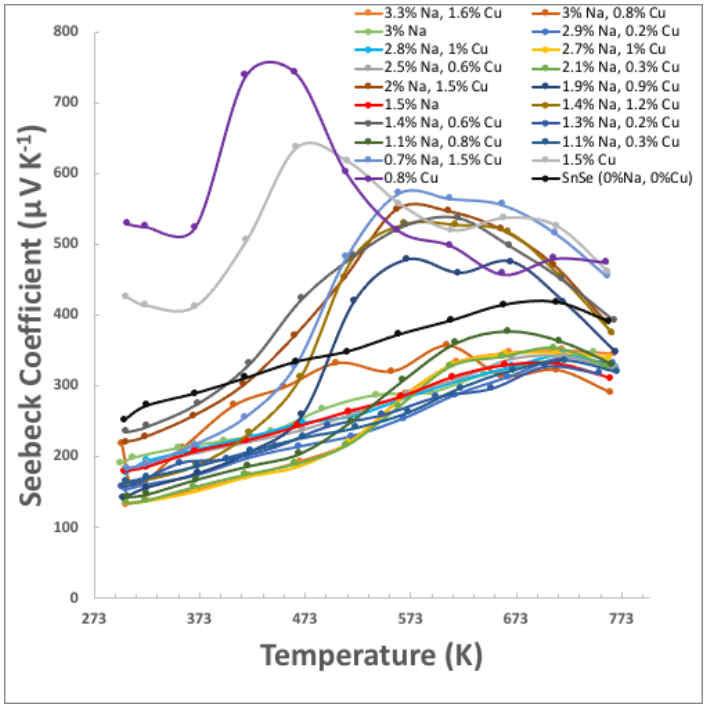

Figure 38. Seebeck coefficients of Na/Cu doped samples during heating.

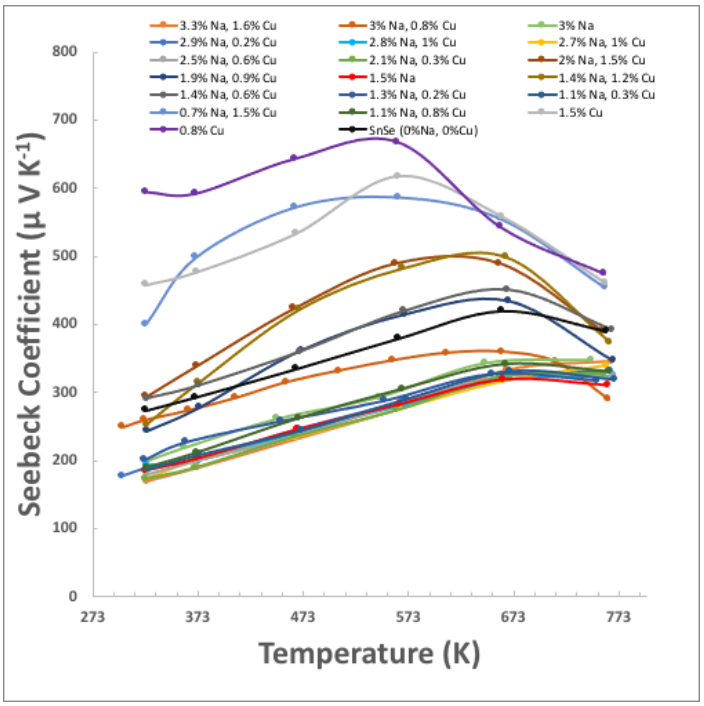

Figure 39. Seebeck coefficients of Na/Cu doped samples during cooling.

For most of the samples the Seebeck coefficient was consistent from heating to cooling, with the exception of the samples with a large amount of Cu (>0.8 %). Additionally during the first heating cycle the low temperature Seebeck coefficients were much lower than when re-measured during cooling. It appears the Cu content causes some hysteresis, as well as oxidation during the ZEM measurement contributing to increased Seebeck coefficients during cooling, as shown in Figures 38, 39. On the surface plot (Figure 40) of the average Seebeck coefficient for each sample, the trend for increased Seebeck with increased Cu is clear, as well as a trend for decreasing Seebeck coefficient with an increasing Na content. Comparing Figures 37 and 40, the small variation in cation/anion ratio has no clear trend with the average Seebeck coefficient.

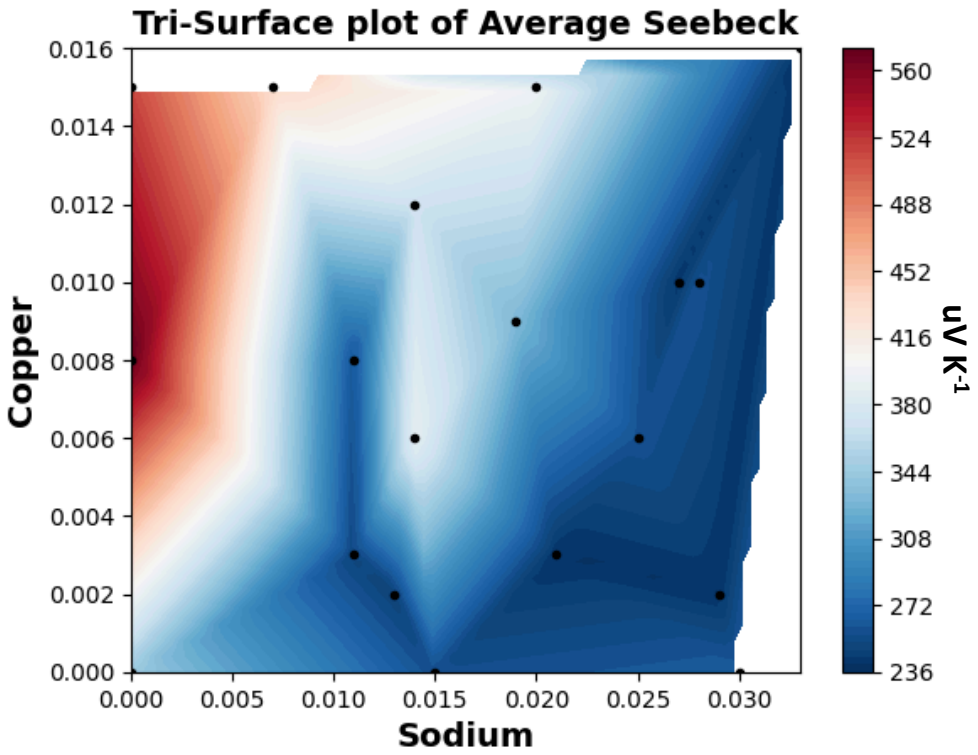

Figure 40. Linear triangular interpolation surface plot of the average Seebeck coefficient plotted versus Na and Cu content.

During heating, the resulting power factor of the $Na_{0.011}Cu_{0.008}Sn_{0.978}Se$ sample was the most improved with a peak value of 7.67 µW cm^{-1} K^{-2} at 419 K. This sample also showed a high average power factor of 5.42 µW cm^{-1} K^{-2} throughout the entire temperature range. However during cooling the power factor of this sample dropped slightly as shown in Figures 41, 42. Impressively the sample $Na_{0.033}Cu_{0.016}Sn_{0.961}Se$ showed an improved power factor during the cooling cycle, with the highest power recorded during cooling of 6.66 µW cm^{-1} K^{-2}. When plotting the results for peak and average power factors on the surface plot, there appears to be a trend of higher power factors when both Na and Cu are matched in a ratio of approximately 2 : 1, respectively with the exception being the $Na_{0.011}Cu_{0.008}Sn_{0.978}Se$ sample.

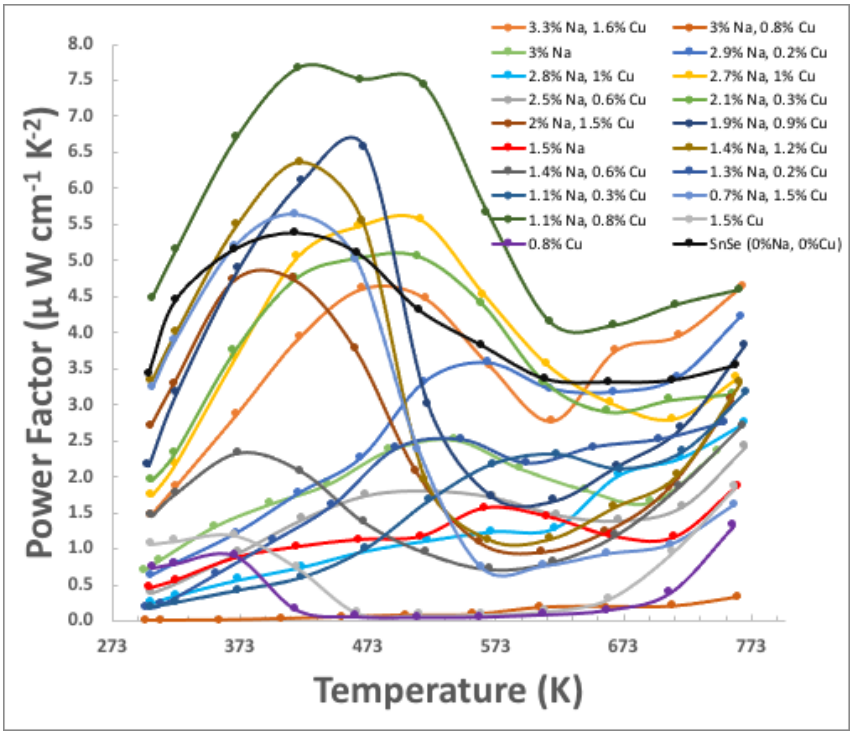

Figure 41. Power Factor of each sample during heating.

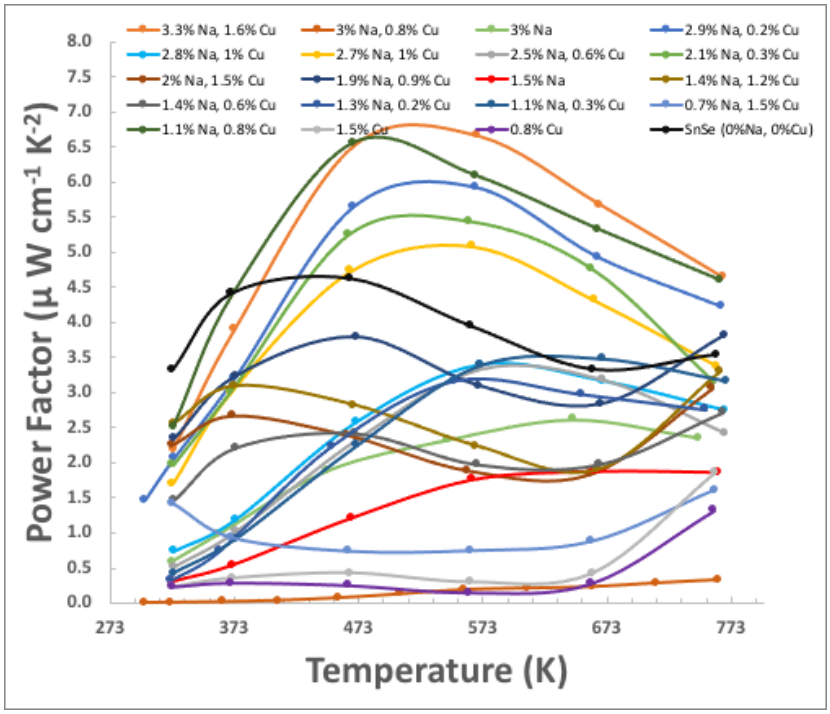

Figure 42. Power Factor of each sample during cooling.

The suspected cause of the increased power factor for this exceptional sample is the cation/anion ratio being slightly lower than 1. This resulted in an increased carrier concentration beyond what was achieved by simply doping with Na and or Cu.

This type of cation/anion ratio was also used for the record breaking tin selenide sample with a composition of $Na_{0.03}Sn_{0.965}Se$ whose peak *zT* reached 3.08, as this sample also had a similar ratio of 0.995 compared to the sample prepared here with a ratio of 0.997. Impressively this sample exceeded the reported electrical conductivity of the record breaking sample, with a maximum of 239 S cm^{-1} compared to 181 S cm^{-1}

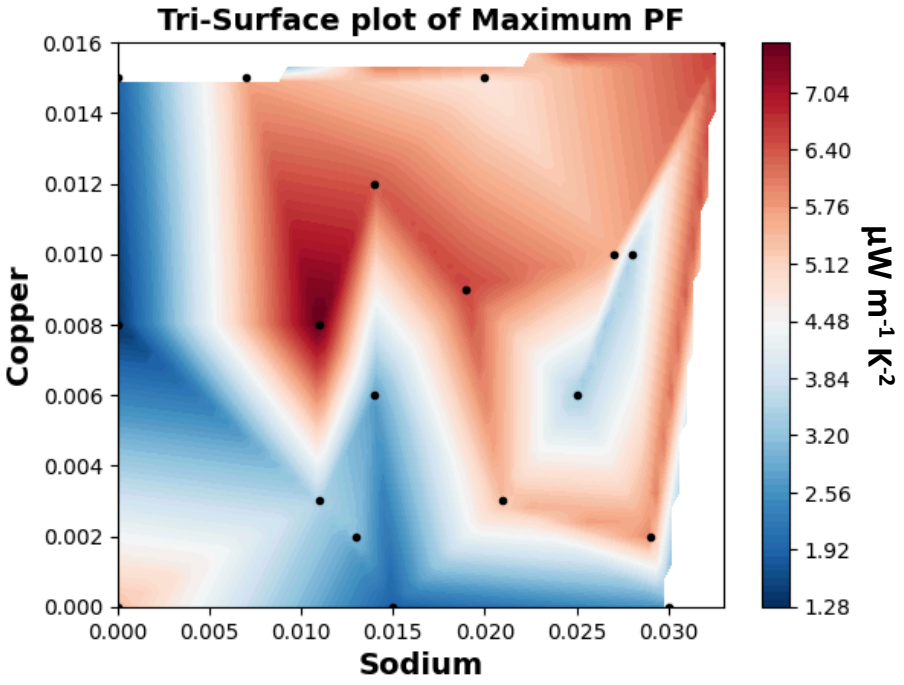

Figure 43. Linear triangular interpolation surface plot of the maximum PF plotted versus Na and Cu content.

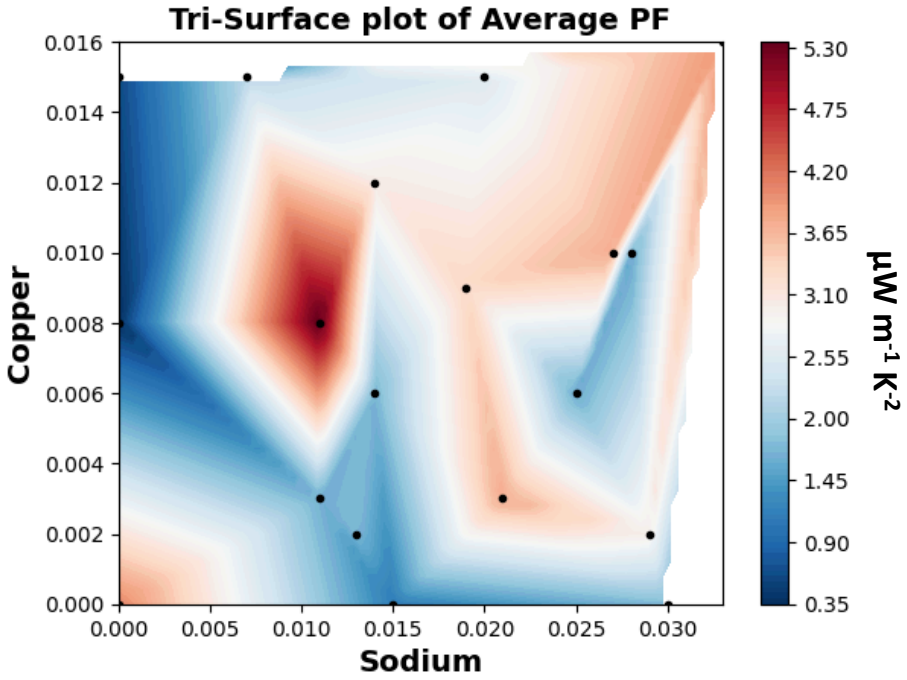

Figure 44. Linear triangular interpolation surface plot of the average power factor plotted versus Na and Cu content.

3.4 Thermoelectric Figure of Merit

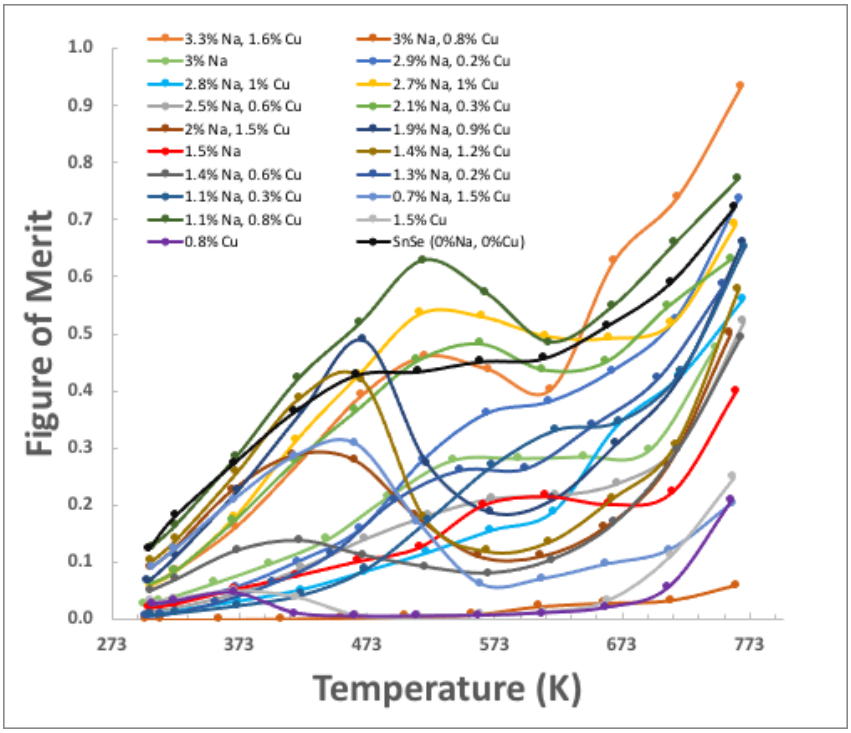

Figure 45. Figure of Merit (*zT*) of each sample during heating.

Two of the prepared samples gained significantly improved peak values of *zT*, and average thermoelectric figure of merit when compared to the undoped tin selenide sample. The compositions which exhibited this improvement were; $Na_{0.033}Cu_{0.016}Sn_{0.961}Se$, and $Na_{0.011}Cu_{0.008}Sn_{0.978}Se$, both showing an average *zT* of 0.452 compared to 0.393 for the undoped sample. One of the more interesting effects was the hysteresis caused improved *zT* through the mid temperature range for the majority of samples during the cooling phase, where the electrical conductivity increased between approximately 523 and 673 K during cooling.

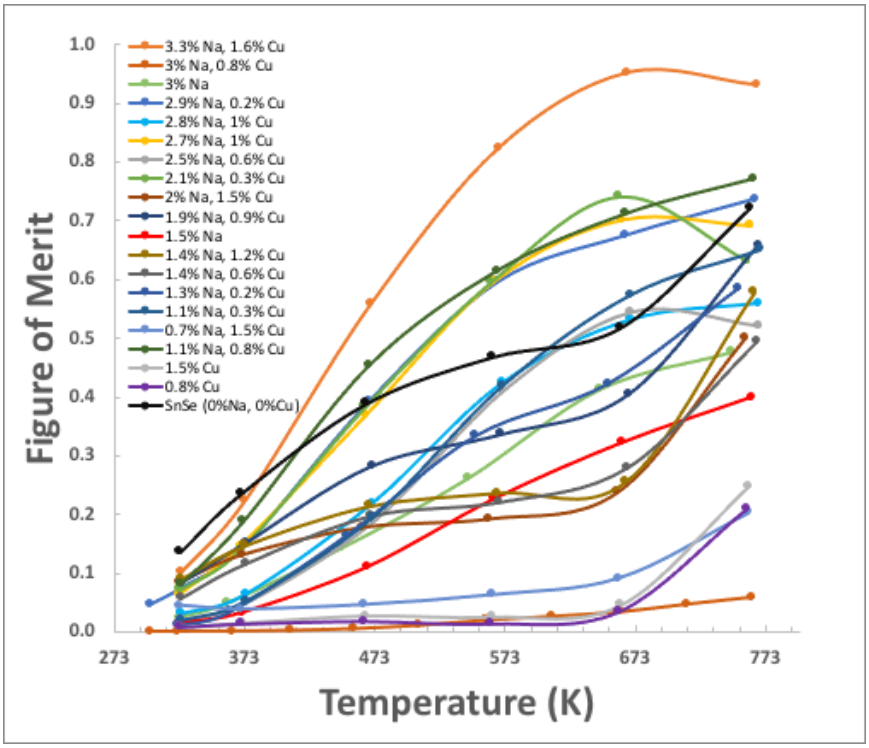

Figure 46. *zT* of each sample during cooling.

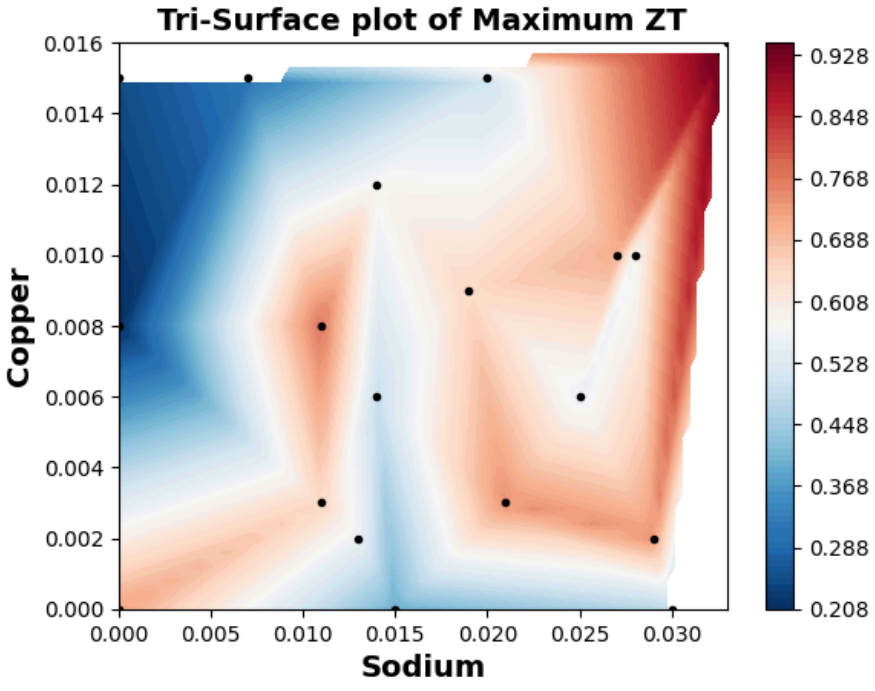

Figure 47. Linear triangular interpolation surface plot of the maximum *zT* plotted versus Na and Cu content.

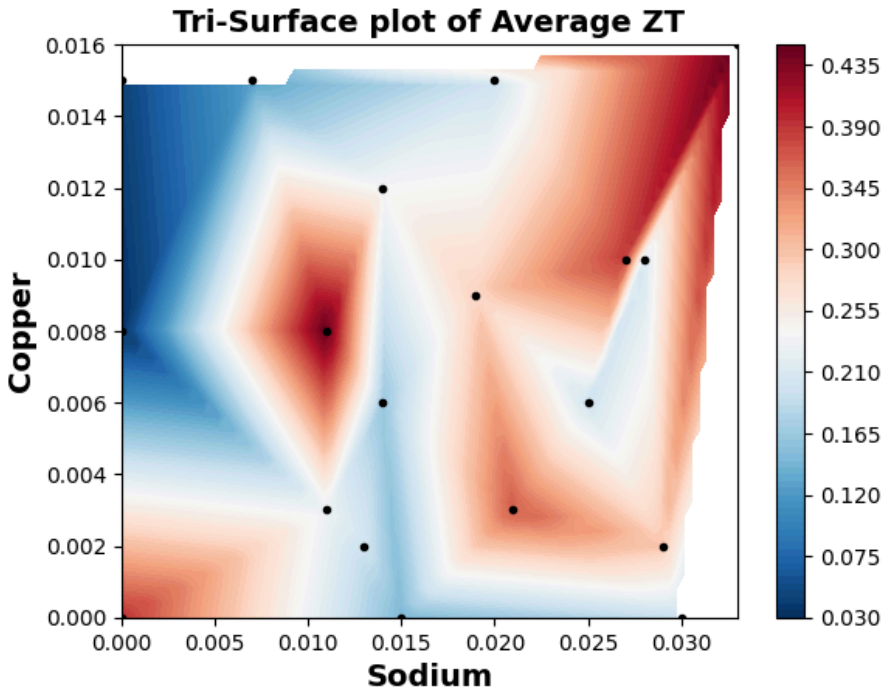

Figure 48. Linear triangular interpolation surface plot of the average *zT* plotted versus Na and Cu content.

3.5 Scanning Electron Microscopy

SEM was completed for some of the samples with notable properties ; $Na_{0.011}Cu_{0.008}Sn_{0.978}Se$ (highest PF), SnSe (undoped control), and $Na_{0.028}Cu_{0.010}Sn_{0.963}Se$ (unexpectedly poor performing sample for the composition). The poorly performing sample was also noted to be extremely fragile during handing, as well as reactive to ethanol and water, giving off a reddish residue, as well as turning water basic when tested with a pH strip. This indicated the Na was reactive still, as well as possibly Se loss due to the reddish color of the contaminated liquids. SEM was completed for un-measured bars from each of these samples, as well as bars which were measured on the ZEM instrument.

Although the quantitative EDAX results for oxygen contamination are not accurate since it is a surface analysis technique, they do confirm the suspected oxidation that was occurring during the ZEM measurement. Despite multiple attempts, and some success in solving the leak on the ZEM instrument, there was still some oxidation occurring during the measurements at higher temperature, thus some of the reduction in electrical conductivity during cooling of the samples. All three samples showed almost double the amount of oxygen according to EDAX after the ZEM measurement (from 14 atomic % to 25 %). Obviously this amount is not quantitatively accurate as the samples would have been highly oxidized even before the measurement, and considering the properties of the samples the actual level of oxygen must be significantly lower. However the increased amount after the measurement is logical considering the visual appearance of the samples. The oxidation from ZEM measurement is not only on the surface of the samples as well since all the bars were sanded and polished prior to SEM and EDAX, and the surfaces of bars which were not sanded after ZEM had visible discoloration due to oxidation. Further oxidation at room temperature was not found to occur in quantity sufficient to change these results.

The poorly performing sample also showed regions of very high Na and Cu, apparent on the back scattered images, as well as regions of microcracks, likely all together leading to the poor performance, as well as physical weakness, (Figures 49-53).

The undoped, and high performing samples (SnSe, $Na_{0.011}Cu_{0.008}Sn_{0.978}Se$) showed no signs of microcracks or any regions of high Na or Cu content, (Figures 54-57).

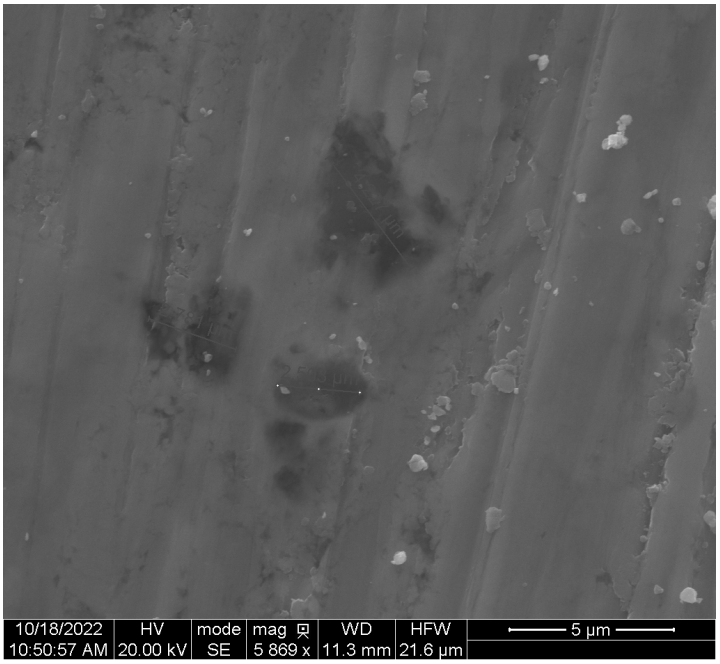

Figure 49. $Na_{0.028}Cu_{0.010}Sn_{0.963}Se$, dark areas showed a high level of Na and Cu localized (9.6 %, 1.8 % respectively) as well as corresponding significant tin deficiency.

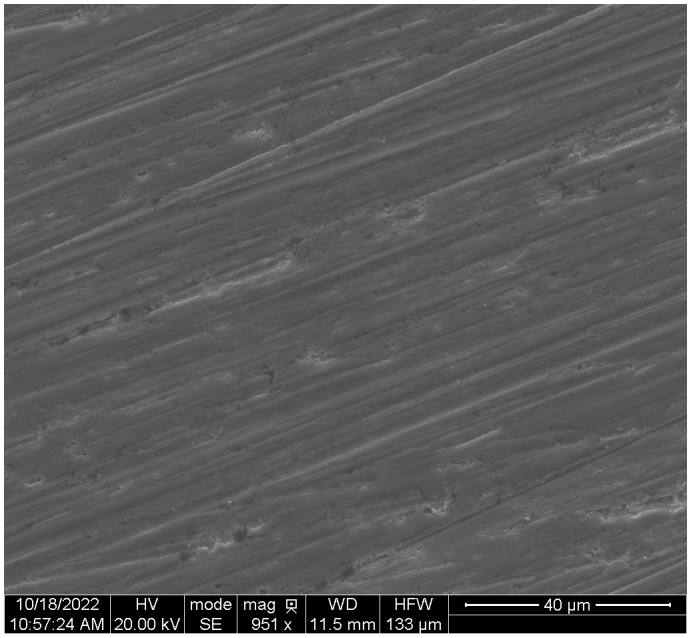

Figure 50. $Na_{0.028}Cu_{0.010}Sn_{0.963}Se$, showed a region of very high Cu and Na localized (20.6 %, 4.3 % respectively) as well as corresponding significant tin deficiency, with no visible changes in the regular SEM image, the region becoming visible in Figure 51.

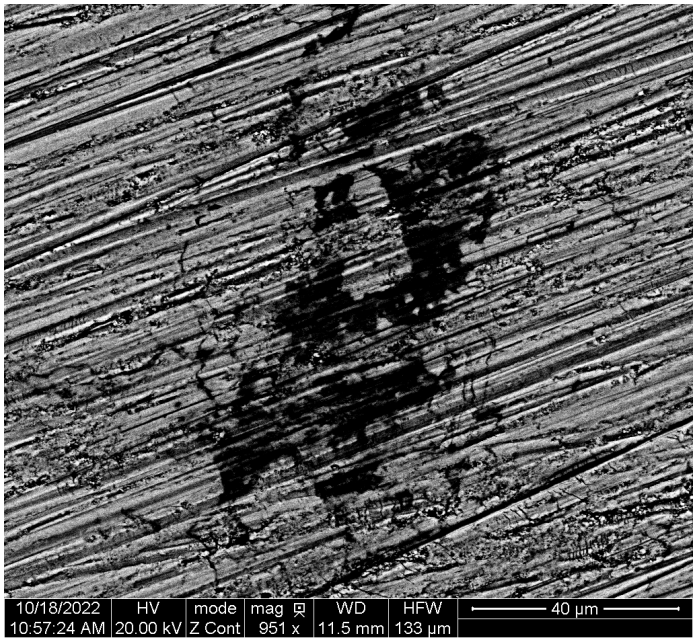

Figure 51. $Na_{0.028}Cu_{0.010}Sn_{0.963}Se$, showed a region of very high Cu and Na localized (20.6 %, 4.3 % respectively) as well as corresponding significant tin deficiency, with a large darker area due to these lighter elements on the backscattered image.

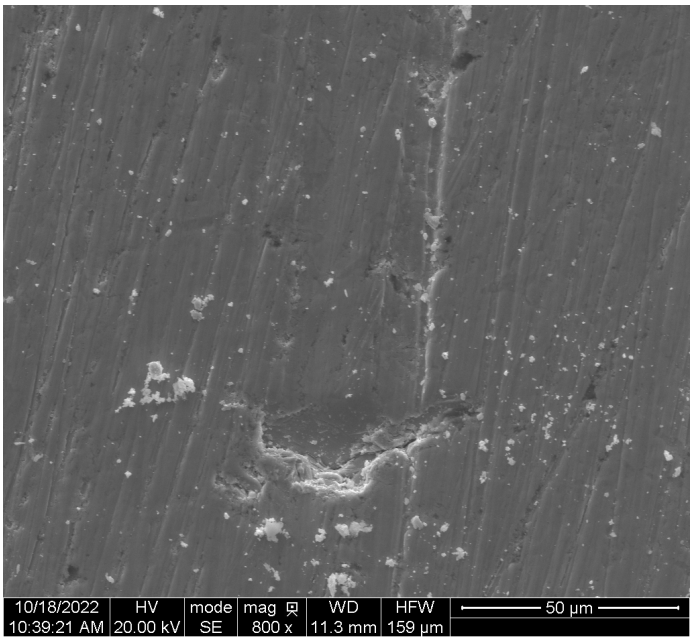

Figure 52. $Na_{0.028}Cu_{0.010}Sn_{0.963}Se$, microcracks visible.

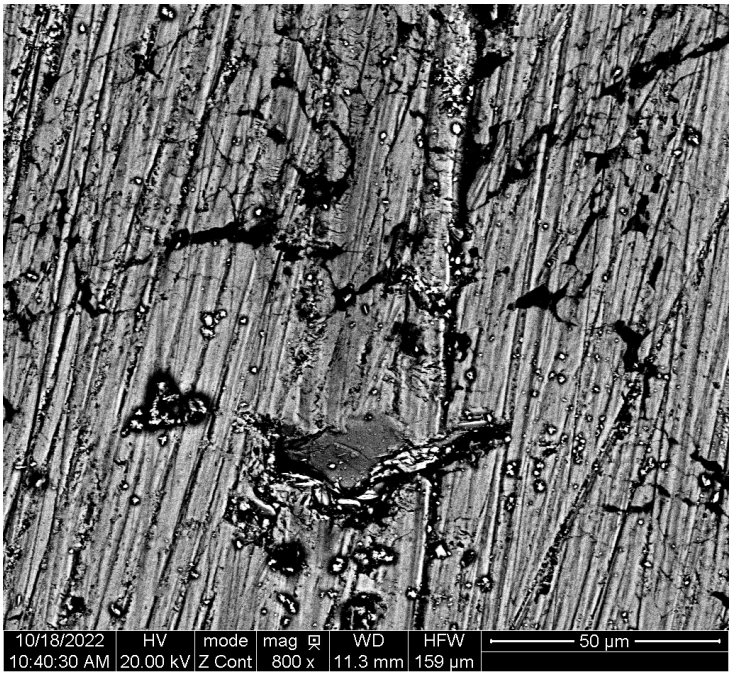

Figure 53. $Na_{0.028}Cu_{0.010}Sn_{0.963}Se$ backscatter image showing a large number of cracks and regions of differing composition.

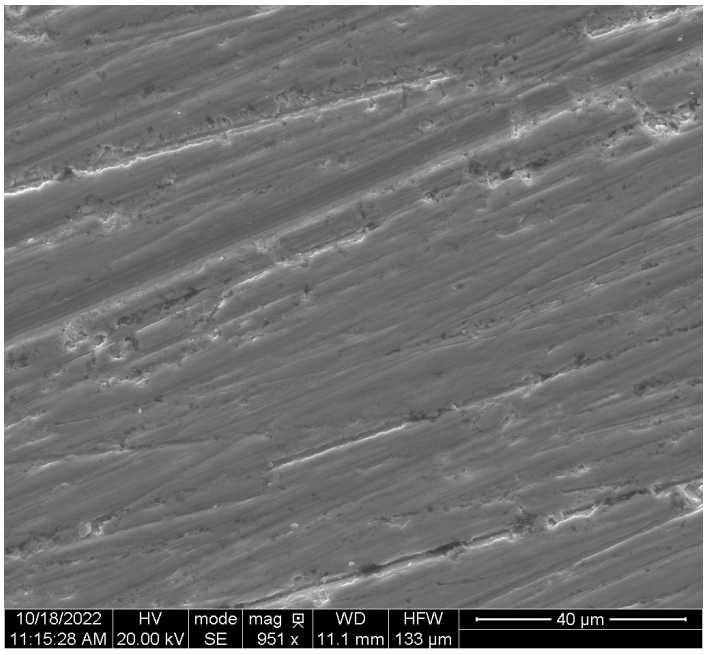

Figure 54. $Na_{0.011}Cu_{0.008}Sn_{0.978}Se$ showing no microcracks, and with no areas of localized high concentrations of Na and Cu.

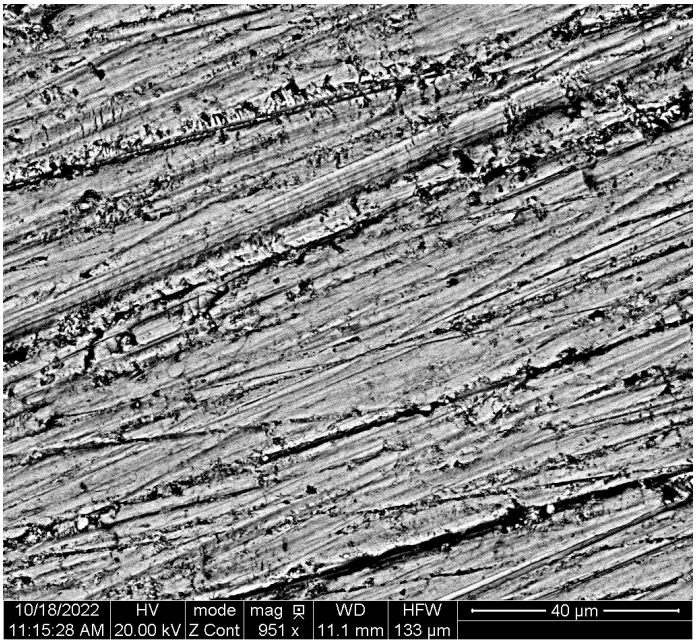

Figure 55. $Na_{0.011}Cu_{0.008}Sn_{0.978}Se$ showing no microcracks, and with no areas of localized high concentrations of Na and Cu, backscattered image.

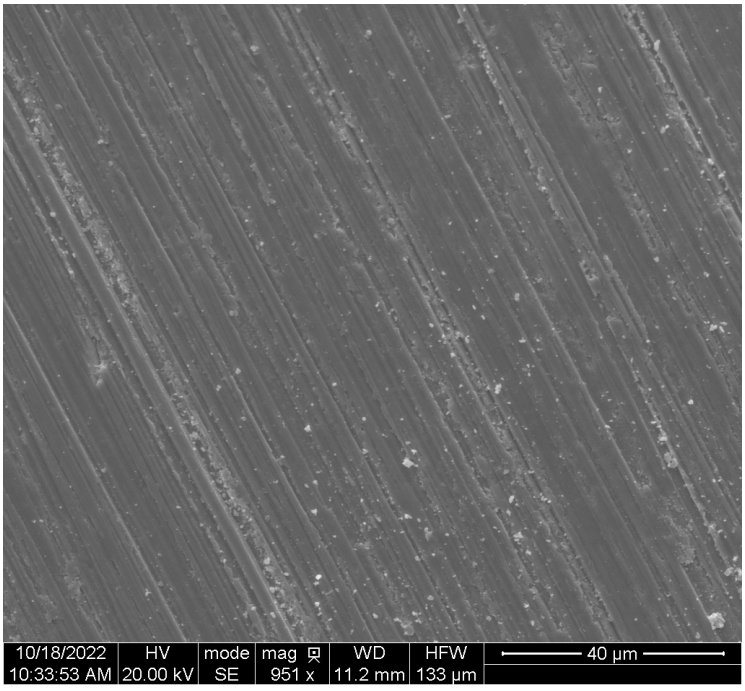

Figure 56. Undoped SnSe SEM image.

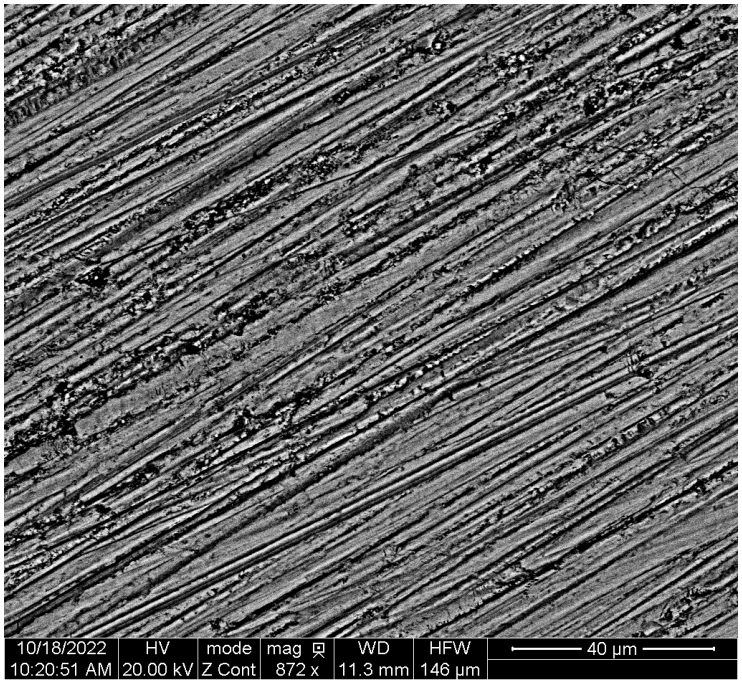

Figure 57. Undoped SnSe backscattered image.

From the SEM images these regions of inhomogeneity and microcracks occurring in samples rich in Cu and secondarily Na are most likely due to the cooling method employed being air cooling, which may have had an inconsistent speed, allowing some samples (particularly those high in Cu) to crystallize forming copper selenides and sodium rich regions. As well the possibility of this inhomogeneity being caused by the grinding method (mortar and pestle) not being sufficient to ensure homogenous samples before hot pressing. It is most likely that all three factors (cooling, stoichiometry, and grinding) contributed to these inconsistencies.

3.6 Powder x-ray Diffraction

Powder X-ray diffraction refinements were completed to verify the correct phase was present for the double doped samples. Figure 58 shows an example of the Rietveld refinement on a sample of nominal composition $Na_{0.029}Cu_{0.02}Sn_{0.969}Se$.

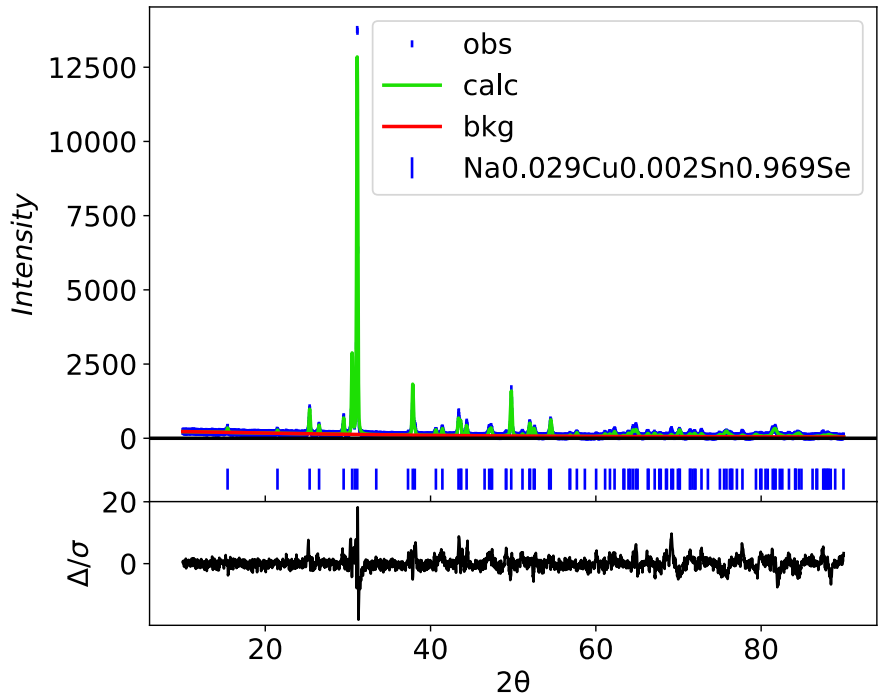

Figure 58. pXRD of $Na_{0.029}Cu_{0.002}Sn_{0.969}Se$.

GSAS II refinement showed unit cell dimensions of a = 11.499 Å, b = 4.149 Å, c = 4.440 Å. The sample exhibits a highly preferred orientation along the (400) plane with an increased unit cell parameter from a = 11.42 Å , as well as a slightly reduced unit cell volume due to the substitution of Na for Sn from V = 213.4 Å^3 to V = 211.9 Å^3.

3.7 Conclusions

Concluding, double doping is a successful method for *p*-type tin selenide when using Na and Cu, when comparing to the undoped sample the average *zT* was significantly improved for two of the samples $Na_{0.011}Cu_{0.008}Sn_{0.978}Se$, and $Na_{0.033}Cu_{0.016}Sn_{0.961}Se$, which both had an average *zT* of 0.45, an increase of 15 % compared to the undoped sample prepared using the same method. However care must be taken during the synthesis procedure as the addition of Cu significantly increases the sensitivity to any changes in the procedure as demonstrated by the poorly performing $Na_{0.028}Cu_{0.010}Sn_{0.963}Se$, which only had an average *zT* of 0.20; due to localization of Cu and Na, extreme tin deficient areas, microcracks, fragility, and higher sensitivity to oxidation. When comparing to other samples the poor performance of some of the samples could not be explained by the composition alone, and must have been due to non-homogeneous pellets. Despite taking care to prepare the samples as consistently as possible the high sensitivity of Na/Cu double doped tin selenide makes it a difficult material to work with.

Chapter 4: Double Doping *n*-type Optimization

4.1 Procedure

Tin metal was prepared from the BDH chemicals tin shot, by washing with HCl, followed by the melting purification procedure described in section 2.1. The tin was brought into the glovebox and weighed out along with the Se from Central Research Laboratories 99.999 % purity, Bi , and tin(II) bromide (309257-10g) from Sigma Aldrich into quartz tubes. Twenty two 3g samples were weighed out with compositions ranging within ($0<x<0.061$, $0<y<0.061$) for the set of samples 1B-22B, $Sn_{1-x}Bi_xSe_{1-y}Br_y$. The quartz tubes were subsequently evacuated, and sealed. Melting was completed for 24 hours at 1273 K, followed by cooling in air. Water quenching was chosen as the method of cooling, as through subsequent practice, in holding the tube level as it is submerged into the water, tube breakage was prevented. It is important to do so, because if the tube is kept vertical, as the tin selenide solidifies the thermal expansion during the phase transition will break the tube, exposing the sample to the air during one of the most critical phases of synthesis.

After cooling to room temperature, the samples were annealed at 773 K for 48 hours, followed by ball milling at 600rpm for a total of 4 hours. The samples were then reduced at 773 K under 5 % H_2/Ar for 12 hours, followed by grinding with the mortar and pestle and finally hot pressing with a ramping time of 30 minutes to 773 K with a 10 minute holding time. After the pellets were sintered, the density was measured, with all of the samples except for 4 achieving >96 % density. The four samples which didn't achieve the desired density had the following compositions and densities respectively; $Sn_{0.983}Bi_{0.006}Se_{0.977}Br_{0.023,}$ 4.94 g cm^{-3} (80 %), $Sn_{0.985}Bi_{0.005}Se_{0.98}Br_{0.02,}$ 5.62 g cm^{-3} (91 %), $SnSe_{0.96}Br_{0.04,}$ 5.67 g cm^{-3} (92 %), and

$Sn_{0.972}Bi_{0.029}Se_{0.97}Br_{0.03}$ 5.74 g cm^{-3} (92 %). Two possible explanations arise for the lower density of these samples. One being the ball milling process, as when the powder is so fine, as the graphite die is loaded, the powder may not pack down consistently, as well as the ratio of cation to anion in the composition as shown in Figure 59.

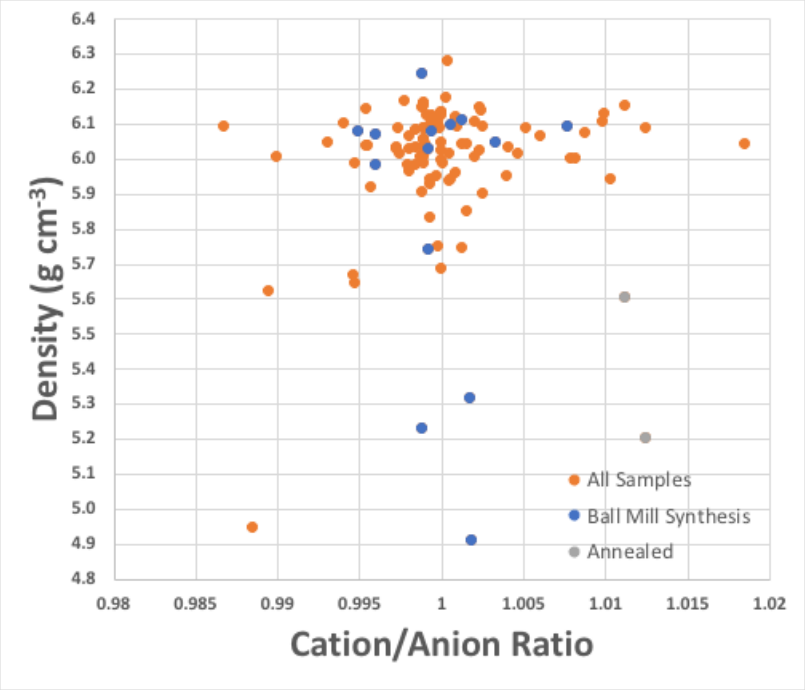

Figure 59. Density plotted against the cation/anion ratio, with the exception of poorly synthesized samples, having a deficiency in cations was associated with lower density. Pictured are all of the samples prepared throughout the thesis project.

When weighing out the elements, the margin for error is very small especially when preparing samples which are only 3g total. The range of values shown is only within 0.985 up to 1.005, further evidence of how sensitive the synthesis is. If the relative amount of Se site atoms is too high compared to the amount of tin site atoms, the excess Se can vaporize during the hot

pressing or measurement stages. This vaporization creates bubbles of varying sizes, and is not necessarily consistent, however it can greatly reduce the density of the sample.

Shown in Figure 60 is an example of a tin selenide sample with a high degree of bubbling due to Se vaporization during subsequent heating, resulting in this reduced density.

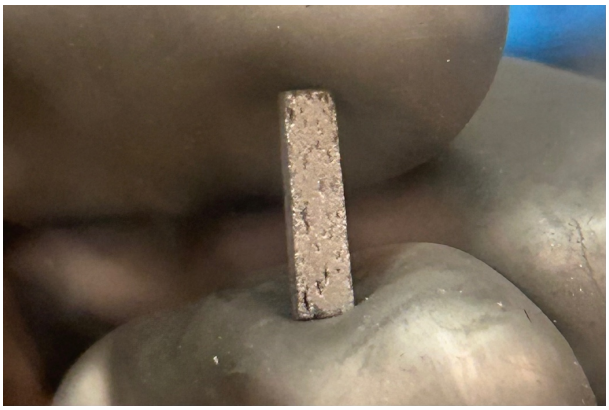

Figure 60. Se vaporization can cause this type of bubbling, only visible during sample cutting, and by the reduced density.

The density of this sample was only 5.20 g cm^{-3} (84 %). Further evidence of this loss of Se was the condensation of red Se on various instruments such as the ZEM seen in Figure 61.

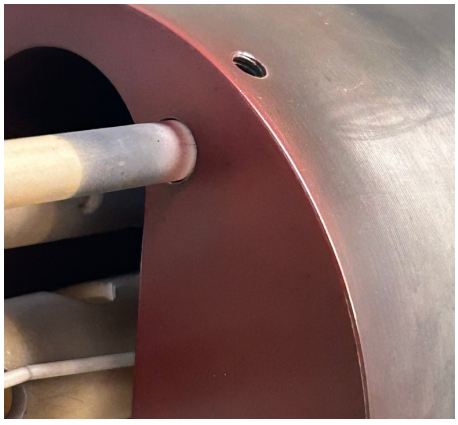

Figure 61. Se condensation in the ZEM instrument, characteristic result of measuring unstable samples with excess Se.

When compiling the data from all of the tin selenide samples made in this project, the trend is more clear as seen in Figure 59, as the only samples with a ratio of cation atoms to anion atoms that had poor densities were two ball milled samples, which did not react fully thus leading to the same Se loss, and two samples which were annealed to too high a temperature after hot pressing and thus had the same issue.

With the samples prepared by ball milling, and the samples which were annealed at too high a temperature labelled, this sensitivity with tin selenide sample preparation is quite apparent.

Another interesting factor in the Br doped samples was that as the tubes were taken from the furnace and quenched, a gas was visually apparent above the molten tin selenide, likely consisting of tin(II) bromide, which has a boiling point of 912 K, as well as when the samples solidified inside the quartz tubes, there appeared to be boiling occurring most likely due to the reducing solubility as the tin selenide solidified. However as shown later, the Br doping was successful, so this observation may not have a large effect.

From each of the samples prepared, two bars, and one disc for electrical and seebeck coefficient determination, and thermal diffusivity measurement were cut respectively.

4.2 Thermal conductivity

The total thermal conductivity was calculated from the thermal diffusivity using the Dulong-Petit method for all 22 samples, followed by calculating the electrical contribution to the thermal conductivity from the Wiedemann-Franz law using the Lorenz number calculated from the Seebeck coefficient as shown in Equation 1-6. Error bars were not included in this chapter to ensure legibility of the figures.

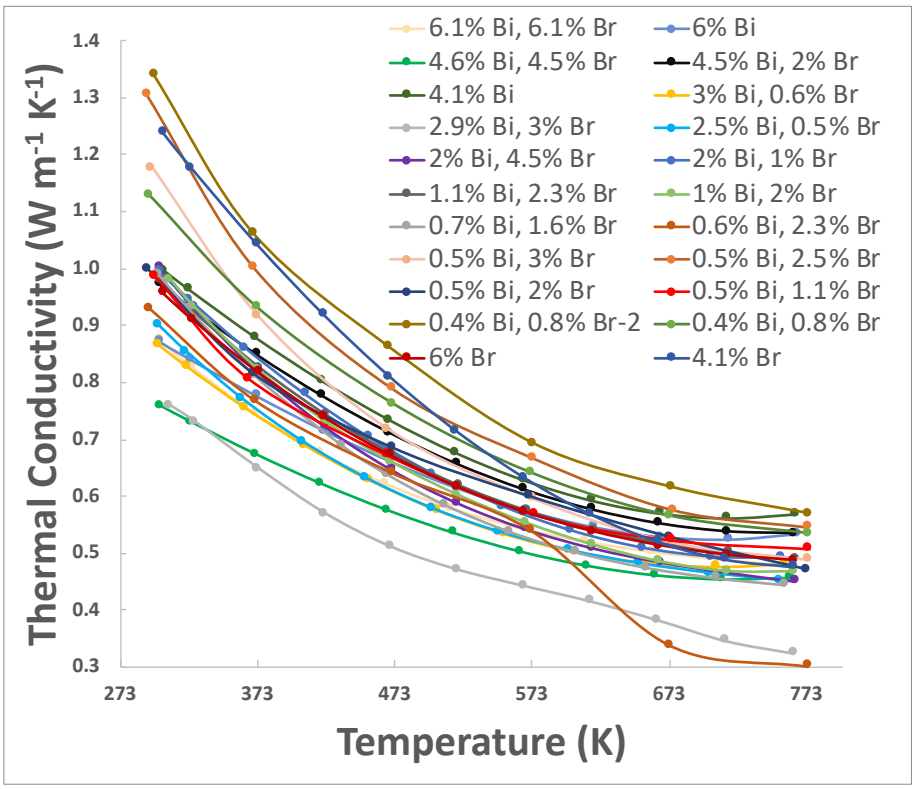

Figure 62. Thermal conductivity of Bi and Br doped samples.

The most important observation was that during both the heating and cooling the Bi/Br doped samples exhibited remarkable consistency in their thermal conductivity compared to the Na/Cu doped samples, with the exception of the sample $Sn_{0.983}Bi_{0.006}Se_{0.977}Br_{0.023}$ which is the outlier in Figure 62, and exhibits a low density shown in Figure 67. As well as a

cation/anion ratio of less than 1. This sample showed a large decrease in thermal conductivity at 673 K, due to bubbling caused by excess Se, resulting in the outlier which can be seen in Figures 62-67.

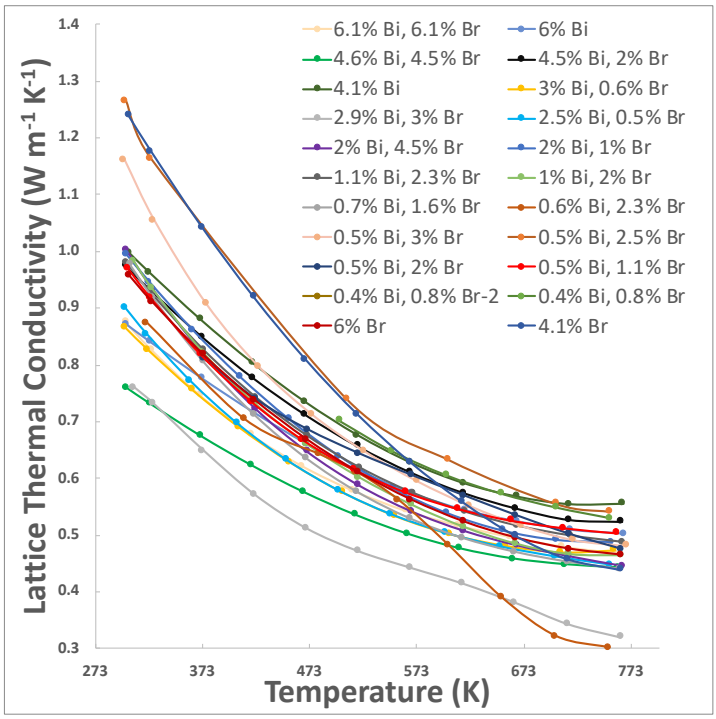

Figure 63. Lattice thermal conductivity of Bi and Br doped samples.

All of the samples showed similar total thermal conductivity results, and using a conventional plot as seen in Figures 62, 63 makes visualizing the effects of the Bi and Br doping difficult to trace. The surface plots from selected key points more clearly show the effects of the Bi and Br doping.

Firstly considering Figure 67. The $Sn_{0.983}Bi_{0.006}Se_{0.977}Br_{0.023}$ sample with the lowest density showed very low thermal conductivity compared to all the other samples as expected with the low density. More interestingly is the sample with 4.5 % Bi, 4.5 % Br doping, which shows

a low RT and low minimum thermal conductivity attributed to reduced lattice thermal conductivity as seen in Figures 64-66.

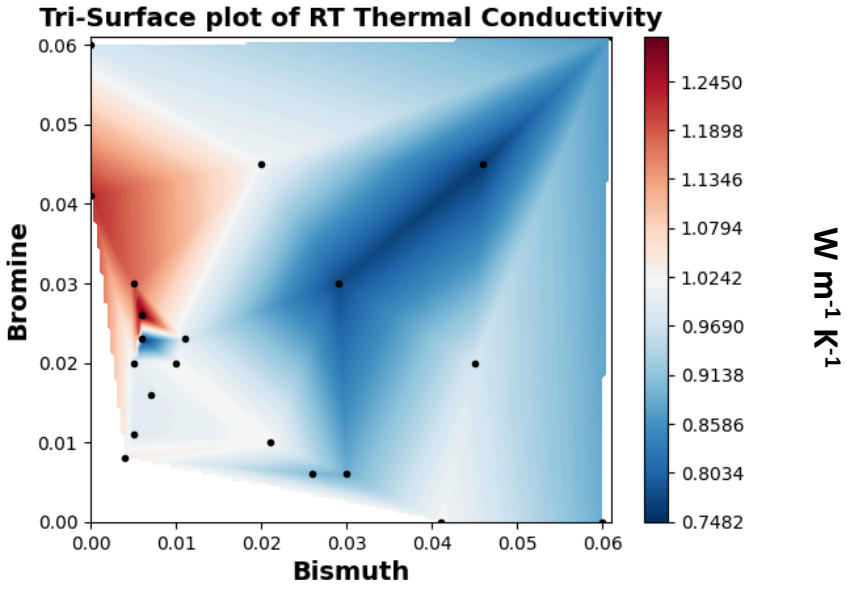

Figure 64. Linear triangular interpolation surface plot of the RT thermal conductivity plotted versus Bi and Br content.

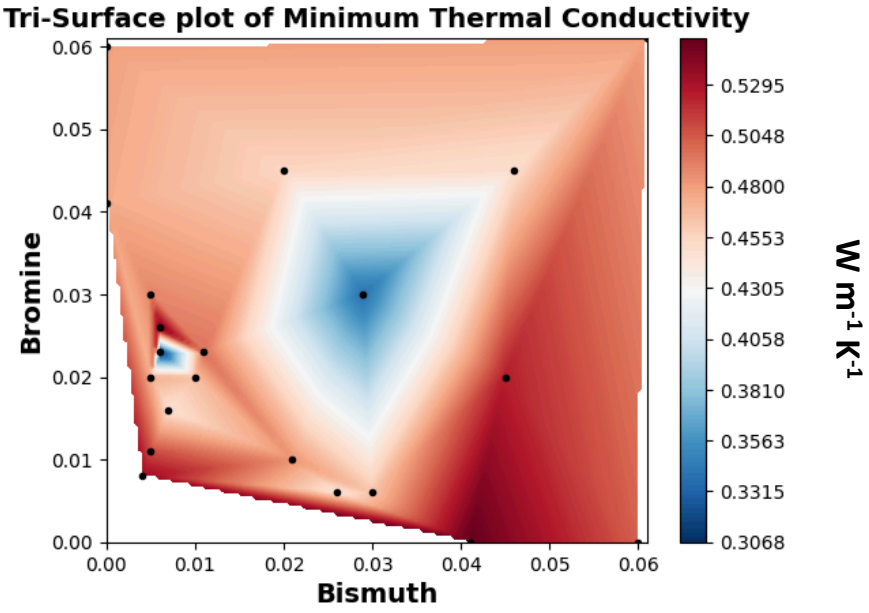

Figure 65. Linear triangular interpolation surface plot of the minimum thermal conductivity plotted versus Bi and Br content.

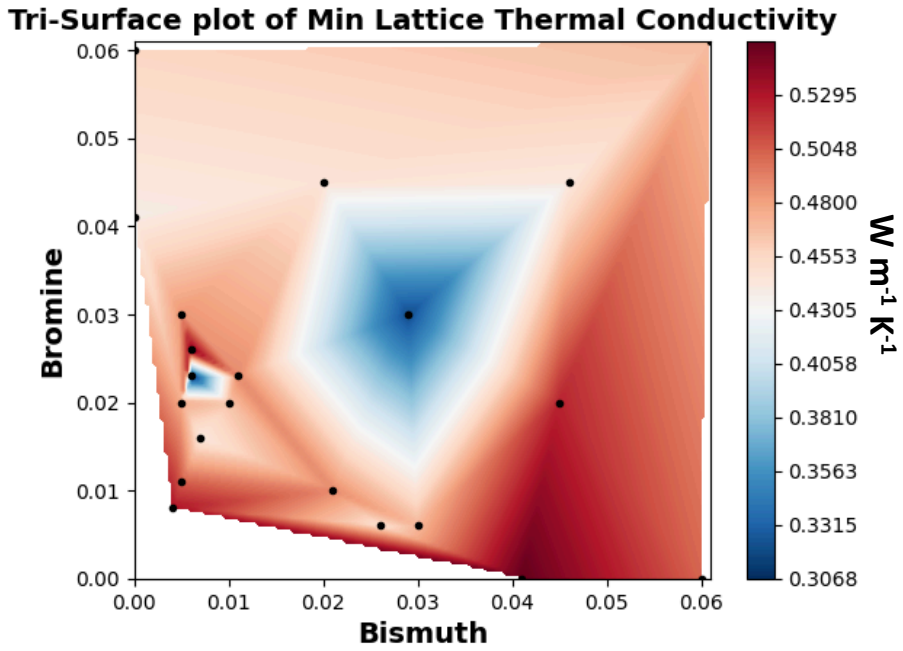

Figure 66. Linear triangular interpolation surface plot of the minimum lattice thermal conductivity plotted versus Bi and Br content, the outlier doesn't change the conclusions.

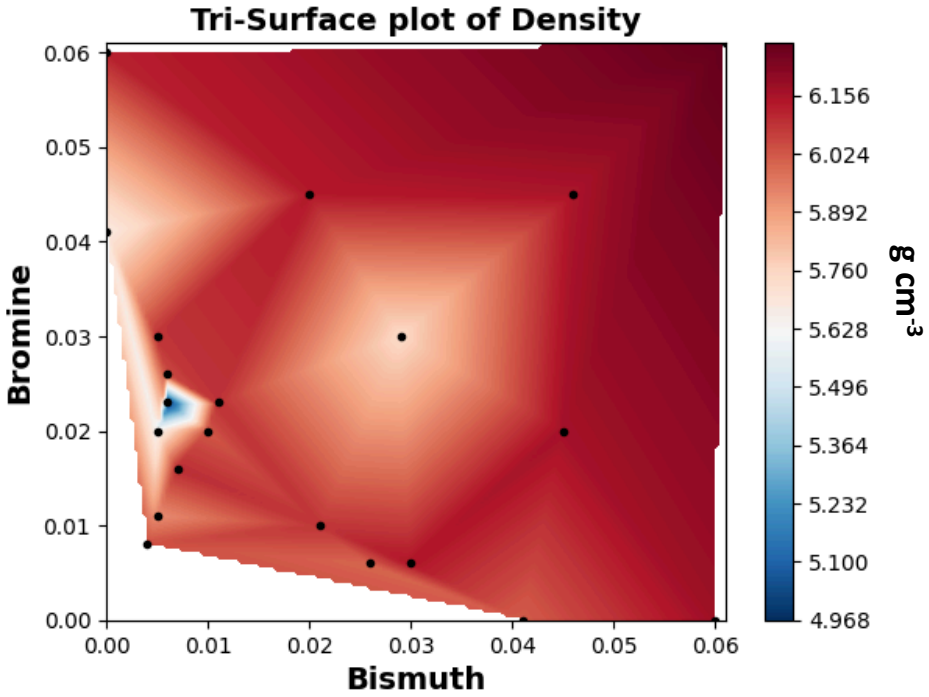

Figure 67. Linear triangular interpolation surface plot of the density plotted versus Bi and Br content.

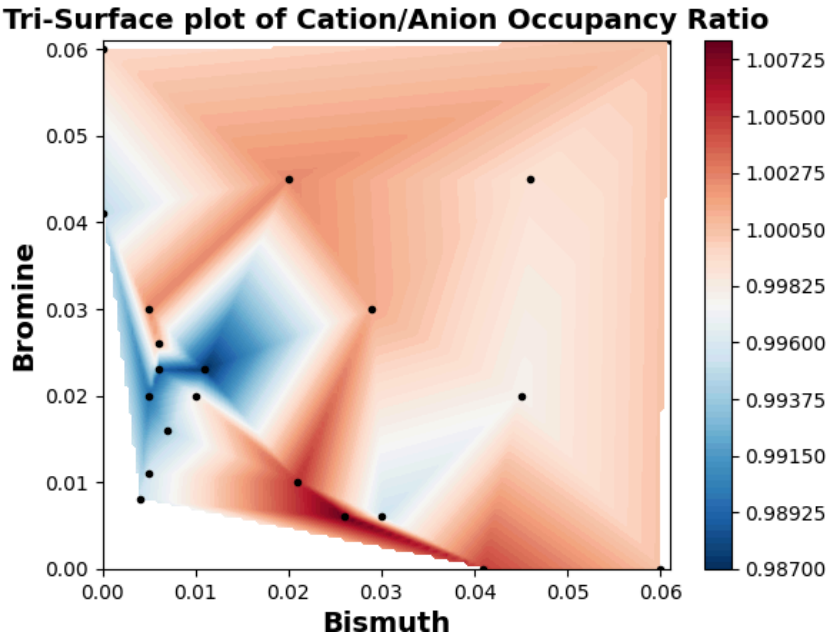

Figure 68. Linear triangular interpolation surface plot of the cation/anion ratio plotted versus Bi and Br content, due to an error during the weighing, some of the samples near 1 % Bi and 2 % Br did not have the correct amount of tin, leading to a small deficiency.

The surface plot of minimum lattice thermal conductivity shows a decreased lattice thermal conductivity with increasing Br doping, and an increased lattice thermal conductivity with Bi doping between 0-4 %, and a slight decrease at 6 % Bi. The 4 % Br sample also showed a high RT thermal conductivity almost entirely caused by a high lattice thermal conductivity. This sample also had a cation/anion ratio of less than 1, which lowered the density of the sample due to the excess Se, causing bubbling after the maximum temperature of the TD measurement. The cause for the increased lattice thermal conductivity of this sample in the lower temperature range

The mechanism for the general trend in the reduced lattice thermal conductivity with increasing Br doping is due to the increased atomic mass of Br when compared to Se, causing increased phonon scattering.

4.3 Electrical Conductivity, Seebeck Coefficient, and Power Factor

The electrical conductivity for all of the Bi and Br doped samples was measured on the ZEM instrument up to approximately 773 K, with the exception of the 6 % Br sample which was further measured up to 873 K. Remarkably the electrical conductivity and Seebeck coefficients of these *n*-type SnSe samples was consistent from heating and cooling, as well the samples exhibited very little softening at the maximum temperature as well as much less oxidation visually.

Likely, addition of these more electronegative elements reduced the reactivity of the tin selenide to oxygen, as well as increasing the physical strength by increasing the strength of the bonding.

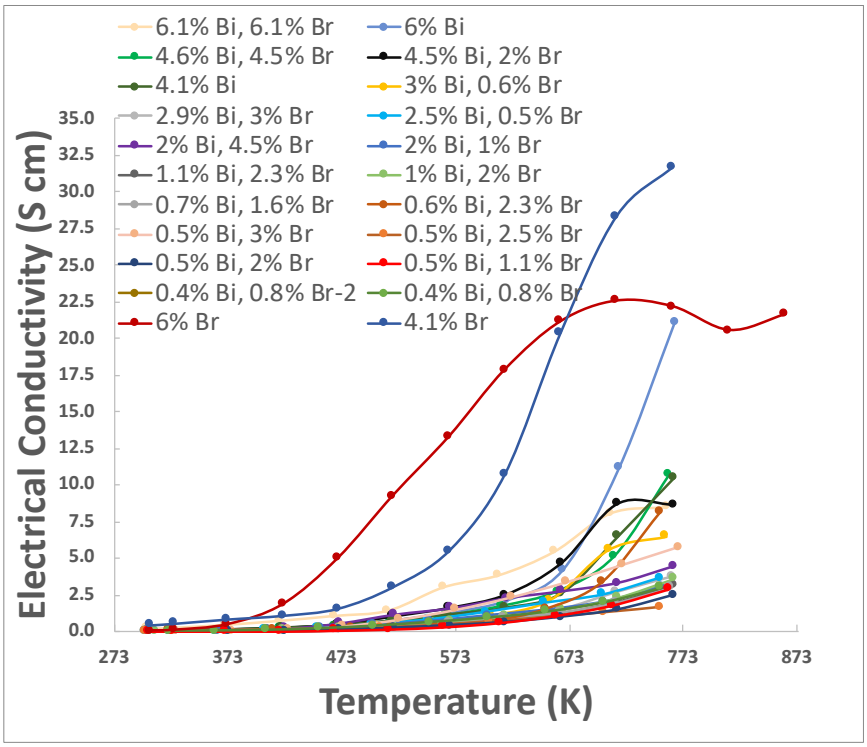

Figure 69. Electrical conductivity of Bi and Br doped samples.

The electrical conductivity of these *n*-type samples was much lower than the *p*-type samples from Chapters 2, 3, as the *n*-type doping has to overcome the natural *p*-type character of the undoped tin selenide material. Both Bi and Br successfully increased the electrical conductivity, of *n*-type tin selenide, as shown in Figures 69, 70.

Figure 70, shows the Br doping was more effective in increasing the electrical conductivity than the Bi doping. It is also important to note that the combination of Bi and Br doping together did not increase the electrical conductivity further than either doping individually, and appears to reduce the doping efficiency in increasing the carrier concentration.

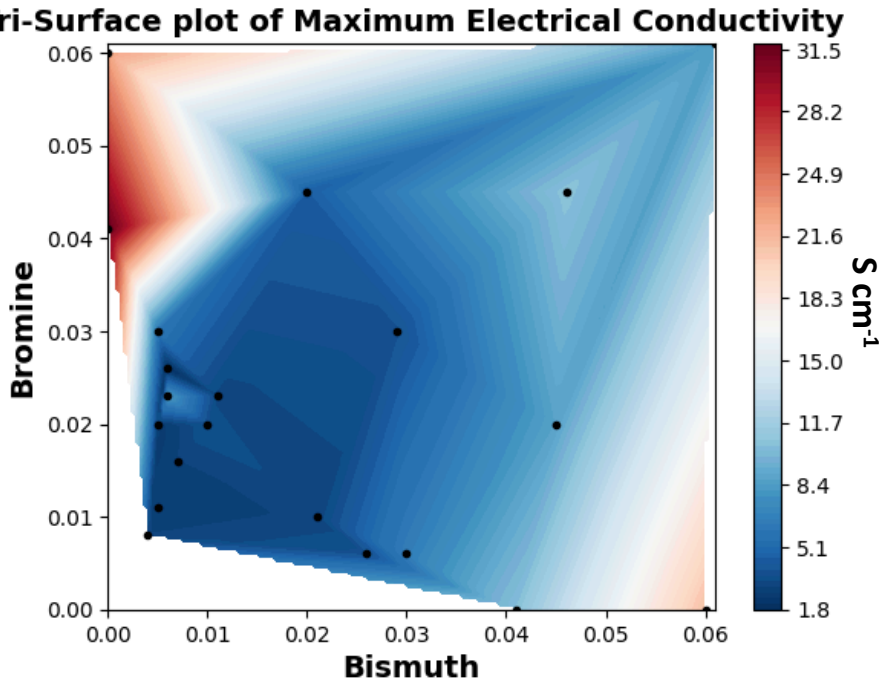

Figure 70. Linear triangular interpolation surface plot of the maximum electrical conductivity plotted versus Bi and Br content.

The Seebeck coefficients of the Bi and Br doped samples were also reduced by the doping as expected with the increasing carrier concentration. However the reduction in Seebeck coefficient for the Bi doped samples was more significant than for the Br doped samples. Samples with a high Bi content also showed a strong trend for reducing Seebeck coefficient with temperature, while samples with a high Br content showed nearly flat correlation with temperature.

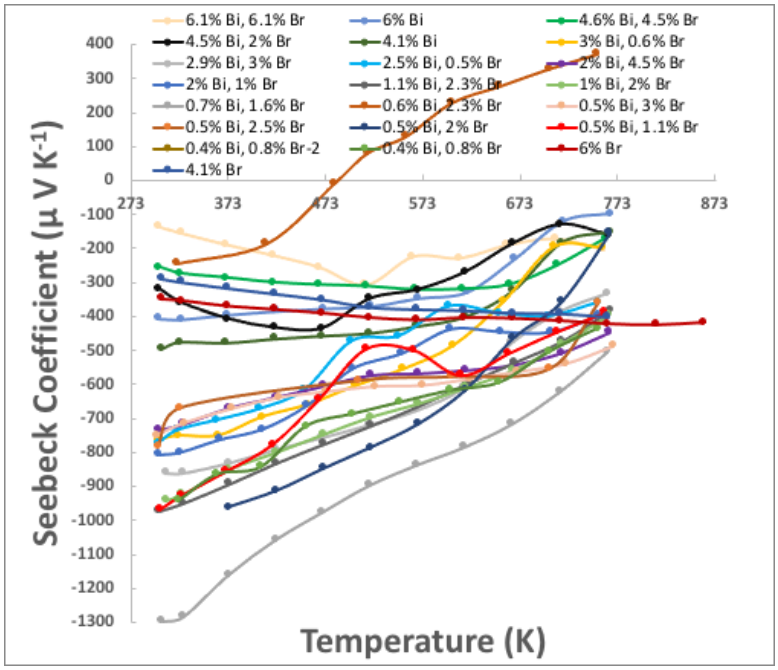

Figure 71. Seebeck coefficients of Bi and Br doped samples.

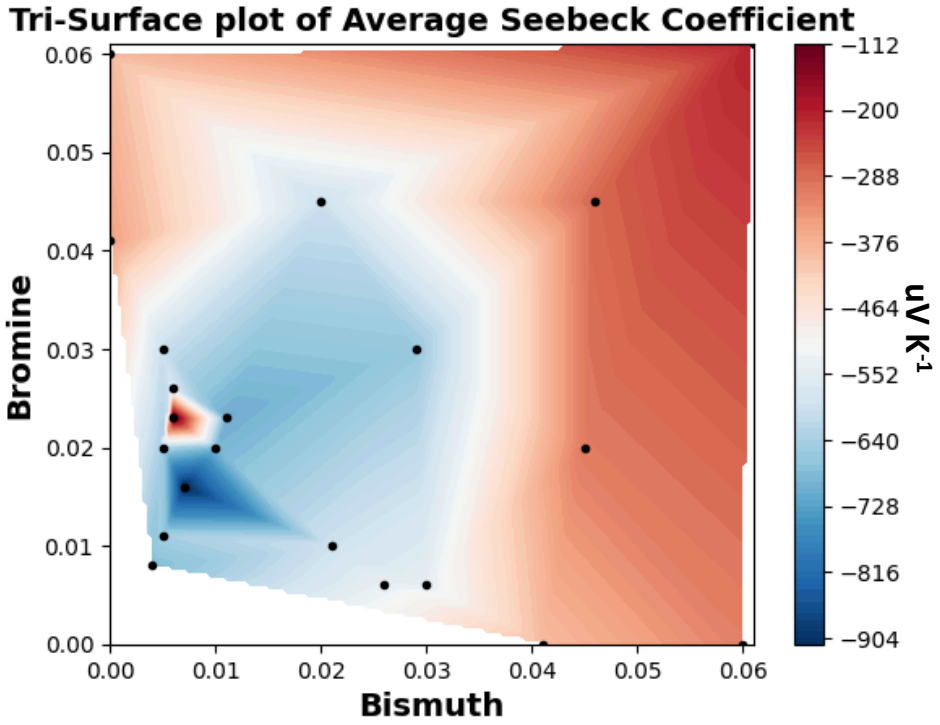

Figure 72. Linear triangular interpolation surface plot of the average Seebeck coefficient plotted versus Bi and Br content.

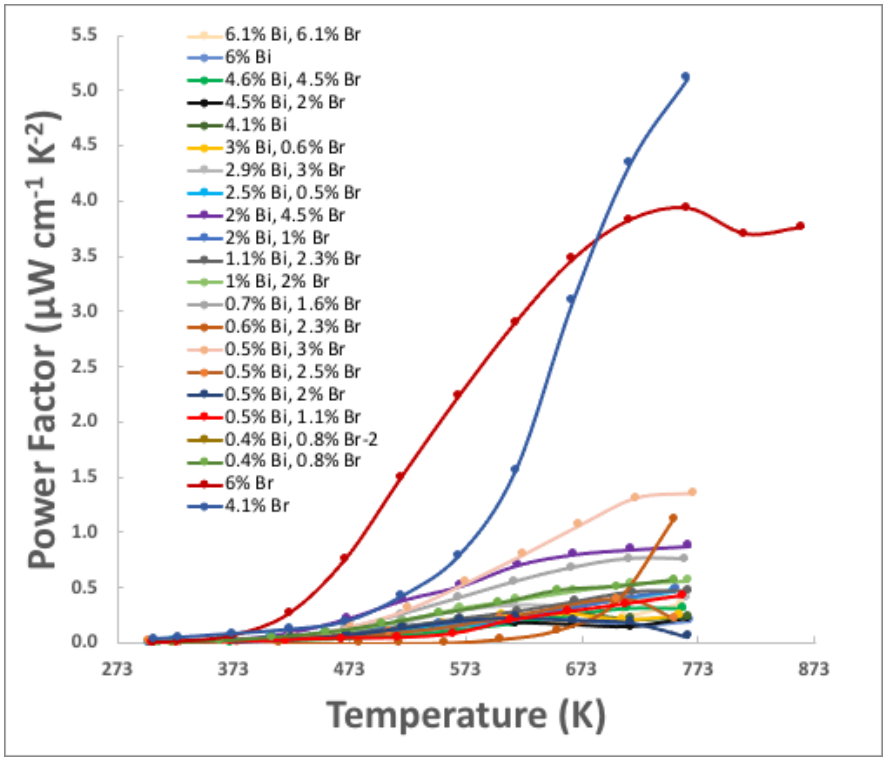

Figure 73. Power Factors of Bi and Br doped samples.

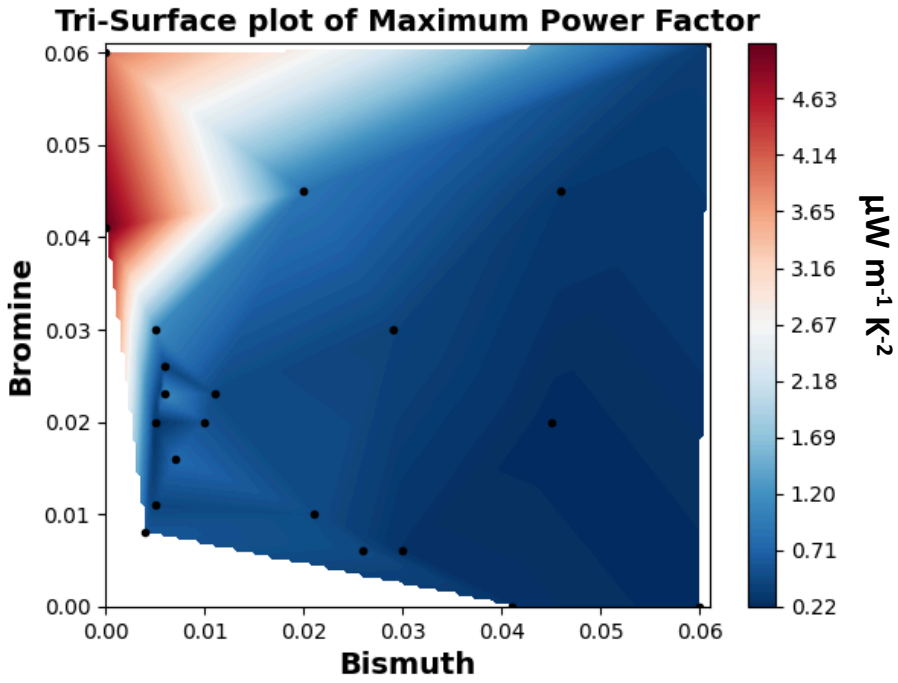

Figure 74. Linear triangular interpolation surface plot of the maximum power factor plotted versus Bi and Br content.

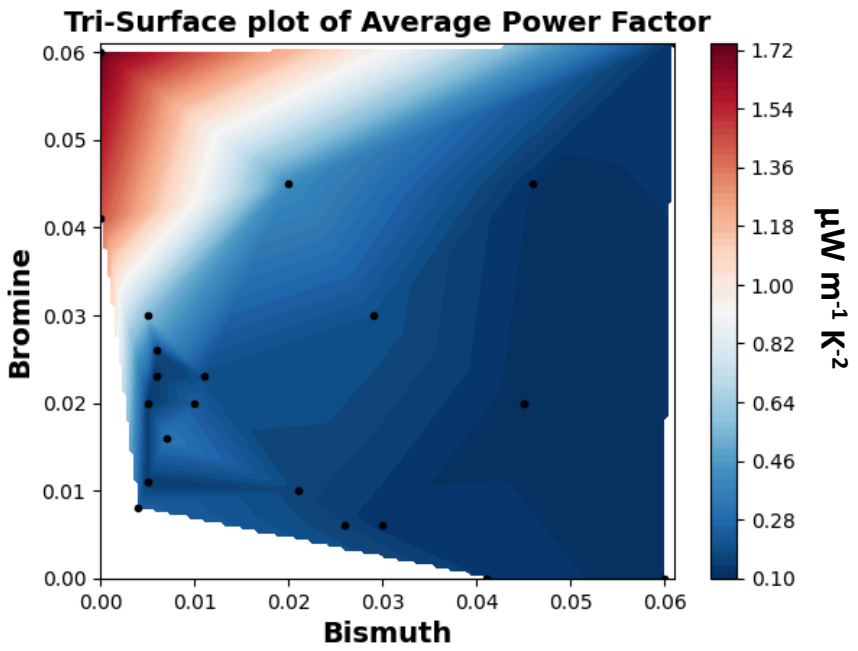

Figure 75. Linear triangular interpolation surface plot of the average power factor plotted versus Bi and Br content.

Finally when combining the Seebeck coefficients with the electrical conductivity, the power factor plots in Figures 73-75 were created. These plots clearly show that the power factor of the samples high in Br were increased, while the samples with increasing Bi content did not show any improvement in maximum or average power factor. The highest average power factor sample prepared had 6 % Br doping, followed by the 4 % Br doped sample. Surprisingly the sample with 6.1 % Br, and 6.1 % Bi for a total of 12 % doping content did not show a high average or peak power factor, and only had a slightly increased maximum electrical conductivity compared to samples with lower doping levels.

4.4 Thermoelectric Figure of Merit

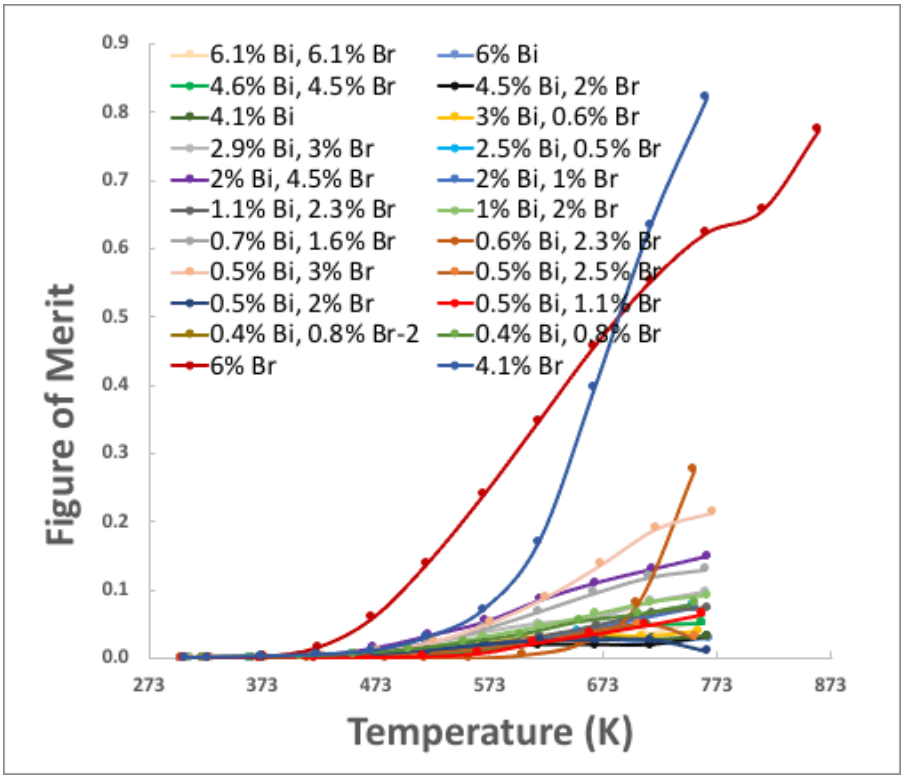

Figure 76. Figure of Merit (*zT*) of Bi and Br doped samples.

Using the power factor and the total thermal conductivity data, the *zT* was plotted for each of the Bi and Br doped samples. The results from Figures 76-78 show a substantial improvement in peak and average *zT* by increasing the carrier concentration using Br doping, with a high correlation to the PF, and very little resemblance to the thermal conductivity plots. This is likely because the lattice contribution to the total thermal conductivity of these *n*-type samples is the main component, and the electrical contribution is very small due to the low electrical conductivities.

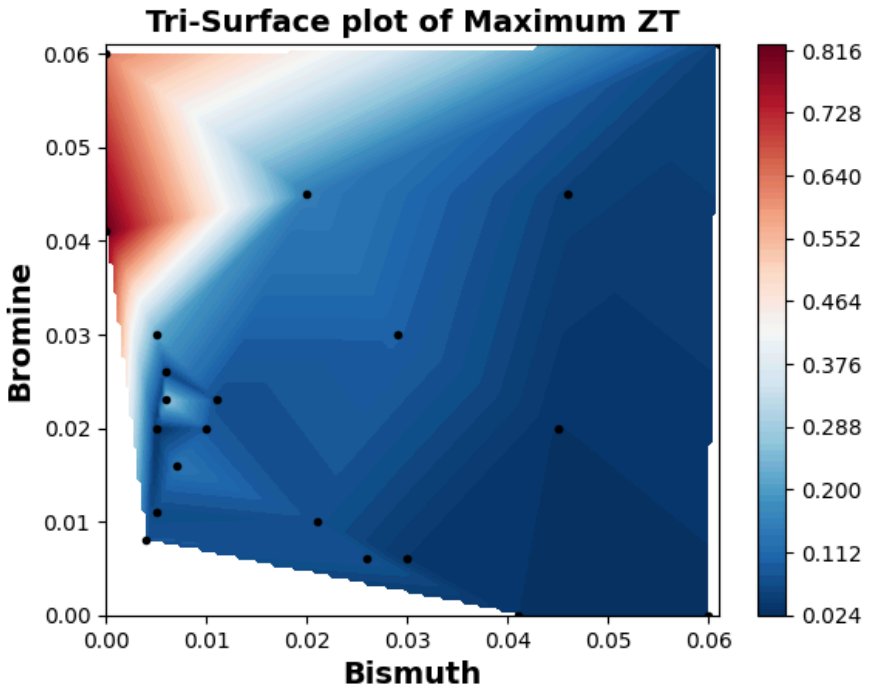

Figure 77. Linear triangular interpolation surface plot of the maximum *zT* plotted versus Bi and Br content.

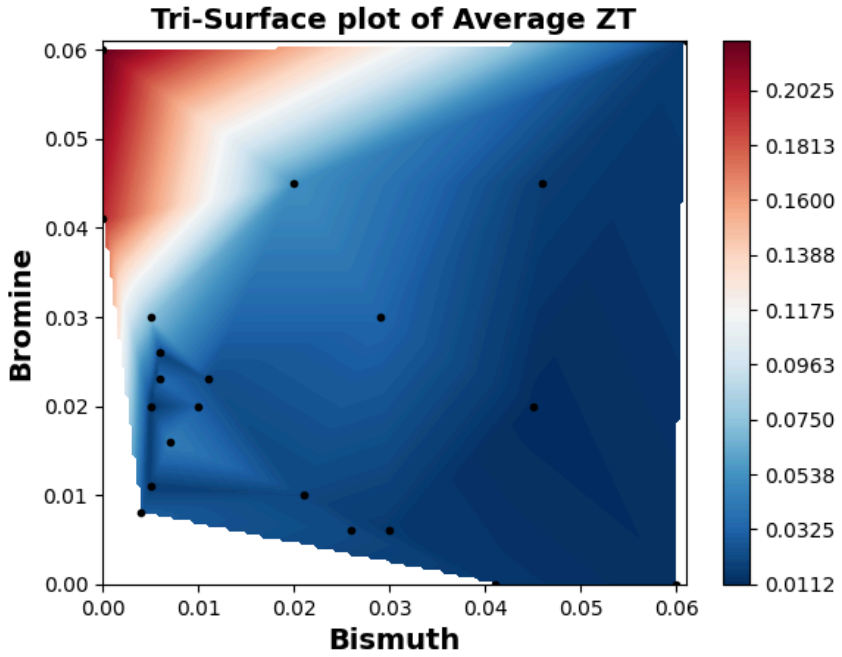

Figure 78. Linear triangular interpolation surface plot of the average *zT* plotted versus Bi and Br content.

4.5 Conclusions

The final results from this method, clearly demonstrated that doping Bi, and Br together does not yield improved properties relative to doping the elements individually. The highest performing samples were those doped with Br due to the increased Seebeck coefficient when compared to samples doped with a similar amount of Bi.

Perhaps using a different synthesis method may yield higher performance of *n*-type tin selenide using both Bi and Br doping simultaneously. A possible study doing so may prepare two individual samples such as $Sn_{0.8}Bi_{0.2}Se$, and $SnSe_{0.8}Br_{0.2}$through the melt synthesis method, followed by ball milling the resulting powders together for a long enough time for homogeneity to occur, and resulting in a sample with the composition $Sn_{0.9}Bi_{0.1}Se_{0.9}Br_{0.1}$. The proposed method may avoid the issue of the tin and Se reacting individually, and the tin bromide reacting with the Bi which likely influenced the poor electrical properties of the double doped samples. Attempting double doping with dopants on both the cation site and the anion site was found to be difficult due to this effect.

As discussed earlier in section 4.1, the appearance of gaseous tin bromide may have also contributed to the inconsistent results of increasing Br doping from 4 % to 6 %. As when cooled and loading the ball milling jars, and scraping all of the contents from the quartz tube, it was not always possible to get all of the residues out, and therefore some preferential loss may have occurred. Despite this, the trend in results was quite clear with increased Br doping leading to higher electrical conductivity as well as maintaining a high Seebeck coefficient when compared to Bi doping or double doping with Bi and Br, which were only able to increase the electrical conductivity, but resulted in significantly reduced Seebeck coefficients.

Chapter 5: Comparison of doping elements polycrystalline Tin Selenide

5.1 Comparison of Different Elements

Using the previously determined optimal compositions from Chapter 3, and 4, five samples were prepared to compare the different doping elements for *p*-type samples (Cu, Ag, and Au), and *n*-type samples (Br and Cl). The five compositions chosen were; $Na_{0.033}Sn_{0.96}Cu_{0.015}Se$, $Na_{0.033}Sn_{0.96}Ag_{0.015}Se$, $Na_{0.032}Sn_{0.96}Au_{0.015}Se$, and $SnSe_{0.94}Br_{0.06}$, $SnSe_{0.94}Cl_{0.06}$. Double doping for the *n*-type samples was not chosen due to the poor prior results of using double *n*-type doping discussed in chapter 4.

The starting materials included; tin metal prepared from the BDH chemicals tin shot, by washing with HCl, followed by the melting purification procedure described in section 2.1, Se from Central Research Laboratories 99.999 % purity, tin(II) bromide (309257-10g) from Sigma Aldrich, Cu 99.9 % from Alfa Aesar, Na 99.8 % from Thermo Fisher Scientific, and Au 99.9 % from Alfa Aesar. All five samples were prepared from the same batch of tin metal to ensure any tin oxide contamination was consistent between samples. The elements were weighed out in the glovebox into quartz tubes, and vacuum sealed, followed by melting at 1373 K for 30 minutes, and water quenching. The samples were then annealed for 48 hours at 803 K, and ball milled for a total of 4 hours at 600 rpm, followed by reducing under 5 % H_2/Ar at 773 K for 24 hours. The samples were then mortar-pestle ground, and sieved to <63 um prior to hot pressing.

All five samples were then hot pressed with a ramping time of 30 minutes to 773 K, and held for 10 minutes with a pressure of 48 MPa; subsequently the densities measured all exceeded 98.5 %.

5.1.1 Thermal Conductivity

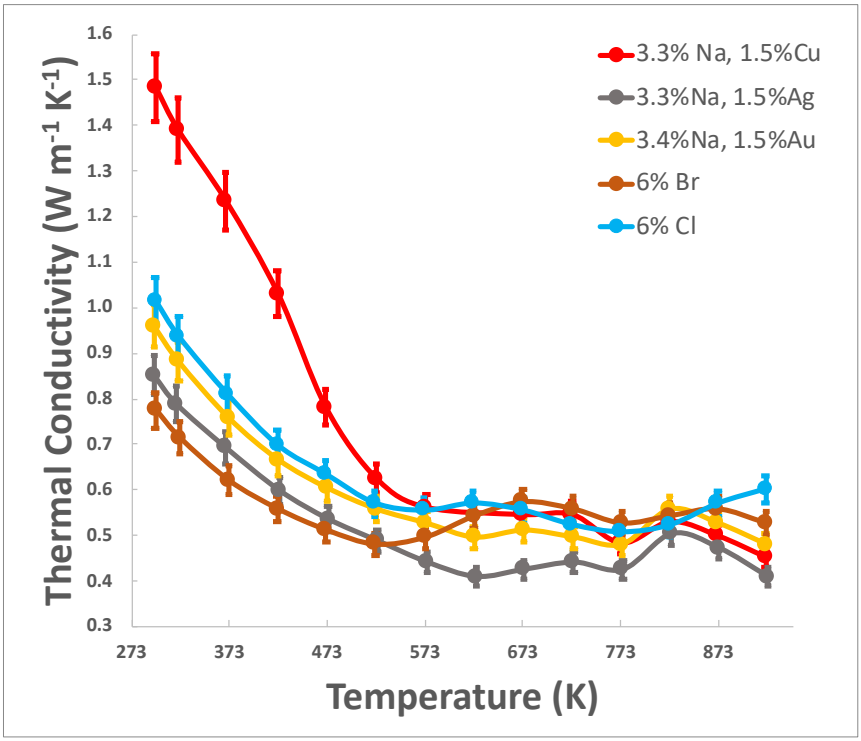

Figure 79. Thermal Conductivity of Na/Cu, Na/Ag, Na/Au doped *p*-type SnSe samples, and Cl, and Br doped *n*-type SnSe samples.

The total thermal conductivity of all five samples was measured starting from RT up to 923 K, and back down to RT. Pictured in Figure 79. is the thermal conductivity during the heating phase to 923 K after the first heating and cooling cycle up to 773 K. The *p*-type doped samples were not stable at the maximum temperatures, and became softened, as well as permanently expanding after the measurement, causing the thermal conductivity during the final cooling phase from 923 K to be greatly reduced. Breaking the thermal diffusivity discs revealed greatly increased grain size, which was visually apparent, when compared to the initial as hot pressed grain size as seen in Figure 80.

Figure 80. Grain growth visible from TD measurement (left is before, right pieces are after TD).

The phase transition is also noted to have occurred at 773-823 K where the thermal conductivity of the *p*-type samples was found to have experienced an increase. The *n*-type samples doped with 6 % Br, and 6 % Cl did not experience the same degree of thermal instability, and the discs appeared unchanged after the measurement. All of the *p*-type samples experienced reduced thermal conductivity during the cooling phase, and this was attributed to the expansion from the grain growth changing the sample dimensions, as well as Se vaporization causing internal bubbling. This effect was most significant with the Cu doped sample, comparing to the Ag and Au doped sample which were significantly more thermally stable. All of the samples except for the Cu doped sample had very low room temperature thermal conductivity in the range from 0.75-1.05 W m^{-1} K^{-1}, which is most likely caused by the increased phonon scattering from the increased number of grain boundaries since the grain size from the ball milling and sieving processes was reduced.

Through the higher temperature range from 573 K up to 923 K all five samples exhibited low total thermal conductivities between 0.4-0.6 W m^{-1} K^{-1}. This is higher than expected since the previously prepared sample from Chapter 3, $Na_{0.033}Cu_{0.016}Sn_{0.96}Se$ had lower thermal conductivity of 0.382 W m^{-1} K^{-1} at 773 K compared to 0.482 for the same composition sample in this series. The higher than expected thermal conductivity is most likely due to the purity of the tin used for this series of samples, as the level of oxides present must have been increased contributing to the poor performance. The tin purification procedure must have not performed as intended, and instead must have increased the amount of oxides present.

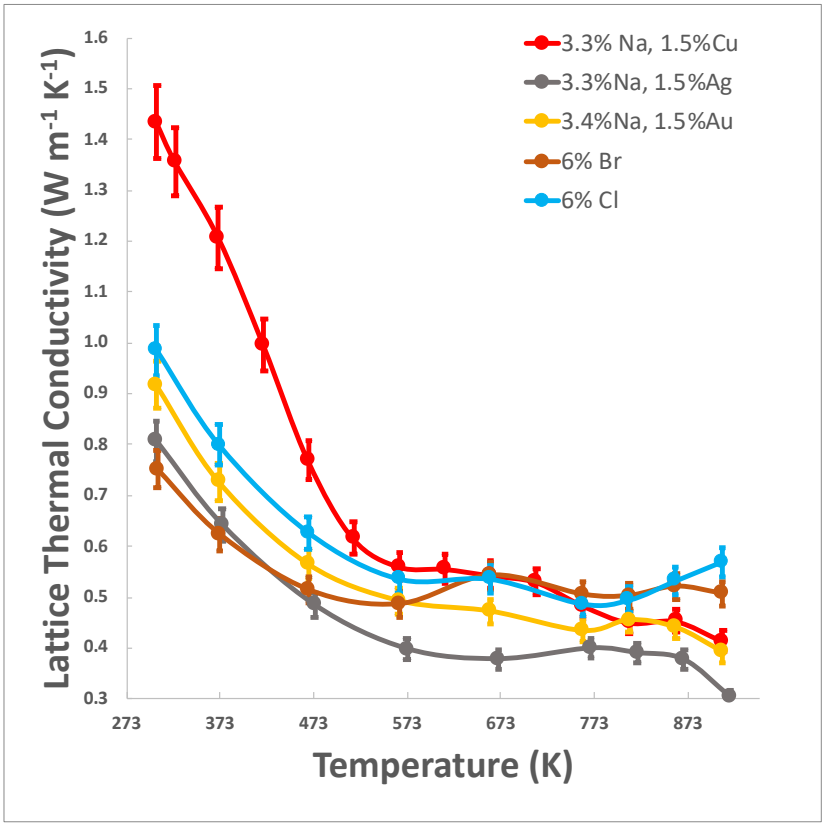

Figure 81. Lattice thermal conductivities of Na/Cu, Na/Ag, Na/Au doped *p*-type SnSe samples, and Cl, and Br doped *n*-type SnSe samples.

The lattice thermal conductivity shown in Figure 82 also shows the expected lower lattice thermal conductivity of the Au doped sample when compared to the Cu doped sample, however the Ag doped sample is an interesting exception to the trend for reducing lattice thermal conductivity by going down the groups with the dopants. The Cl doped sample is also expectedly showing a higher lattice thermal conductivity than the Br doped sample due to the lower atomic weight of Cl compared to Br.

5.1.2 Seebeck Coefficient

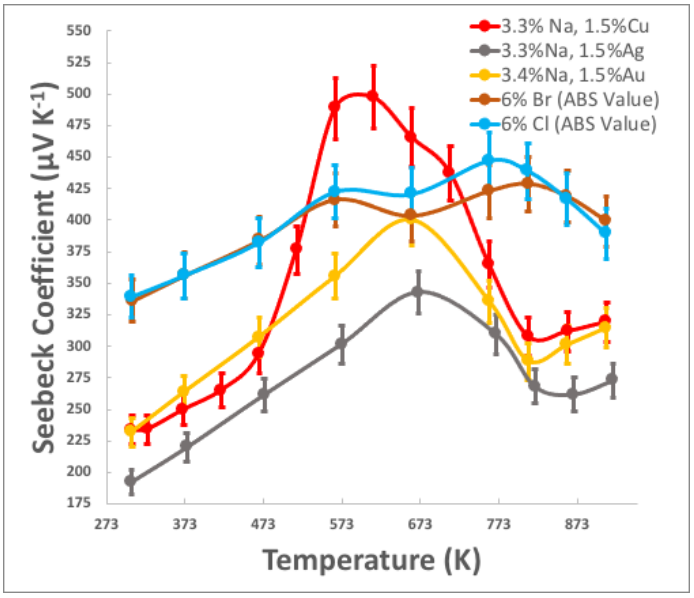

Figure 82. Seebeck coefficients of Na/Cu, Na/Ag, Na/Au doped *p*-type SnSe samples, and Cl, and Br doped *n*-type SnSe samples.

The Seebeck coefficients of the *n*-type Cl and Br doped samples were very similar with no significant change considering the experimental error of 5 %. While the *p*-type dopants with Cu, Ag, and Au show that Ag doping decreases the Seebeck coefficient compared to Au doping. The Cu doped sample also shows the characteristic spike in Seebeck coefficient in

mid-range temperatures as seen for many samples in Chapter 3. The Au doped sample shows an improved Seebeck coefficient compared to the Ag doping.

5.1.3 Electrical Conductivity

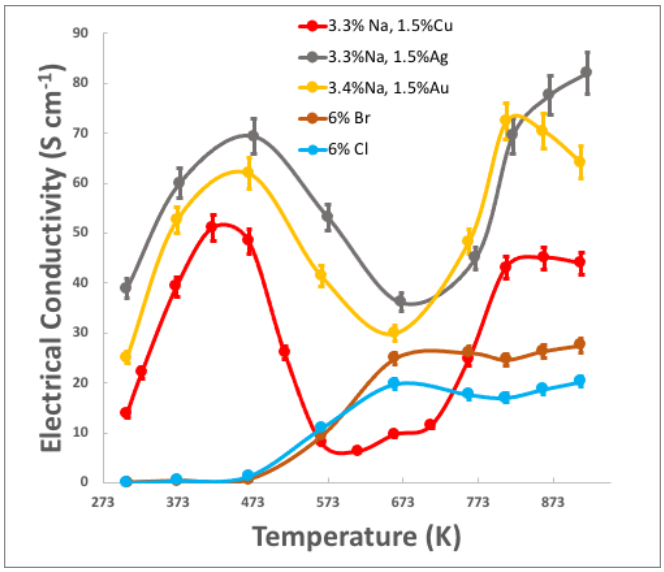

Figure 83. Electrical conductivities of Na/Cu, Na/Ag, Na/Au doped *p*-type SnSe samples, and Cl, and Br doped *n*-type SnSe samples.

The electrical conductivity of the *p*-type dopants show that Ag was the most efficient dopant at increasing the carrier concentration, followed by Au, and finally by Cu.

The slightly less efficient doping by Au is likely due to the higher electronegativity of Au when compared to Ag. However Cu was shown to be the least efficient of the three for increasing the electrical conductivity, possibly due to the possible formation of Cu selenide, as well as the larger size difference between Sn and Cu when compared to Sn and Ag. For the *n*-type dopants, the Br doping was shown to be more efficient at increasing the carrier concentration and thus the peak electrical conductivity was higher. This is most likely due to the similar size

of Br and Se allowing for effective placement of Br atoms within the tin selenide structure, while the Cl is a much smaller atom.

5.1.4 Power Factor and *zT*

The power factor of the Na/Au doped sample was the highest, due to the increased Seebeck coefficient when compared to the Na/Ag doped sample, while the Na/Cu doped sample showed a decreased power factor throughout the midrange temperatures from 523-723 K. This resulted in the Na/Cu doped sample to have the lowest *zT* of the *p*-type dopants tested. The Na/Ag and Na/Au samples *zT*'s were very similar with no clear higher performing sample, as the Na/Ag doped samples reduced thermal conductivity made up for its lower PF when compared to the Na/Au doped sample. For the *n*-type dopants the higher power factor and lower thermal conductivity of the Br doped sample resulted in a much higher *zT* starting from 673 K onwards.

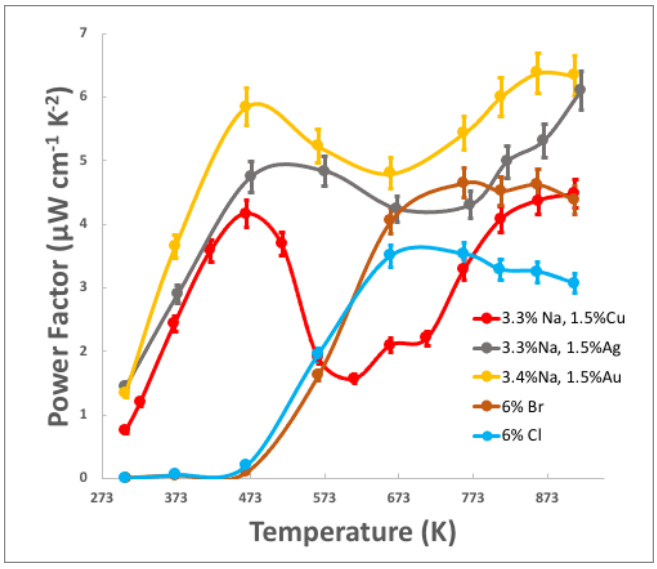

Figure 84. Power Factors of Na/Cu, Na/Ag, Na/Au doped *p*-type SnSe samples, and Cl, and Br doped *n*-type SnSe samples.

Both the *n*-type dopants Cl and Br resulted in samples which were highly temperature stable, and resistant to oxidation when compared to any of the *p*-type dopants used.

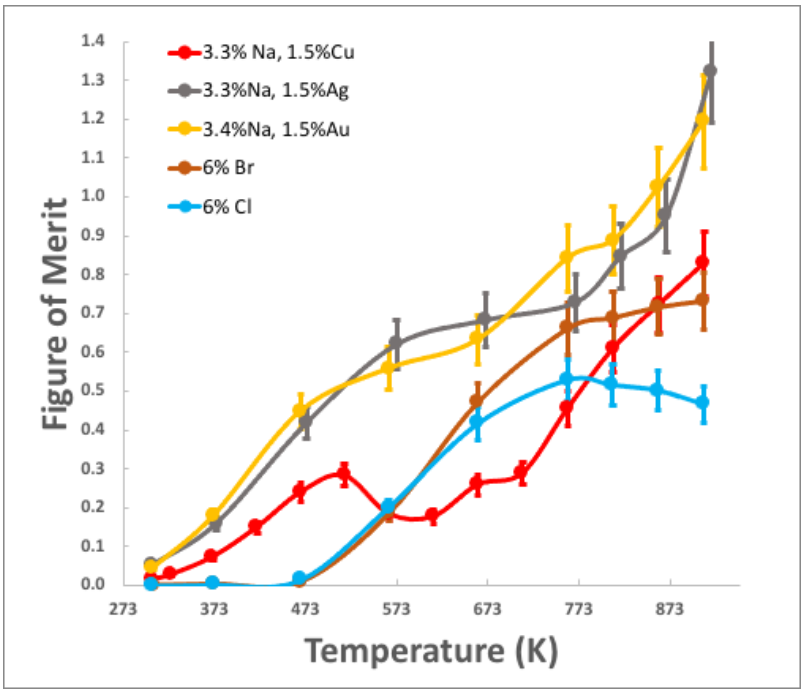

Figure 85. Figure of Merits of Na/Cu, Na/Ag, Na/Au doped *p*-type SnSe samples, and Cl, and Br doped *n*-type SnSe samples.

5.2 Optimized Samples

Using the compiled previous results, a selection of 4 different compositions were prepared, one un-doped pure tin selenide using the same procedure and tin starting material, two with the composition $Na_{0.033}Ag_{0.016}Sn_{0.963}Se$, two with the composition $Na_{0.032}Au_{0.015}Sn_{0.963}Se$, and one sample with the composition $SnSe_{0.9}Br_{0.1}$. Adding an undoped sample as a control sample was key to compare the effect of the addition of doping elements, as well as to compare to published results for undoped tin selenide to compare the procedure used for synthesis. The Na/Ag double doped, and Na/Au double doped compositions were chosen due to the results from sections 5.1.1-5.1.4 where the average and maximum *zT* of these compositions was very similar with no clear higher performing composition. Finally the Br doped *n*-type sample composition was changed from the previously selected $SnSe_{0.94}Br_{0.06}$ composition due to the relatively low maximum electrical conductivity, indicating that the carrier concentration was not high enough. Using previous published results for polycrystalline Br doping, the amount of Br doping was increased to 10 % from 6 %. This increase was selected before the results of the previously mentioned 4 % Br doped sample was re-measured after the ZEM instrument was repaired, otherwise it may have been reasonable to reduce the amount of Br in the composition.

Using the same starting materials as in section 5.1, the tin was subjected to an additional step in an attempt to reduce the oxide concentration since this was suspected to be the main issue with the previously prepared samples. The tin metal was brought into the reduction oven, and melted under 5 % H_2/Ar gas at 1073 K for 1 hour, followed by loading into the glovebox, and scraping the surface clean. For each of the 4 compositions, 8 grams total was the sample

size used for synthesis. Each samples elements was weighed into quartz tubes, vacuum sealed, and then loaded into a second larger sample tube to ensure no contact with oxygen in the event of tube breakage. As an example pictured below in Figure 87 is the $Na_{0.033}Ag_{0.016}Sn_{0.963}Se$ sample. The Na, Sn, and Ag are all visible and visually appear free of oxides. Most importantly the Na is lustrous demonstrating the sealing of the quartz tube was successful in preventing oxygen contamination.

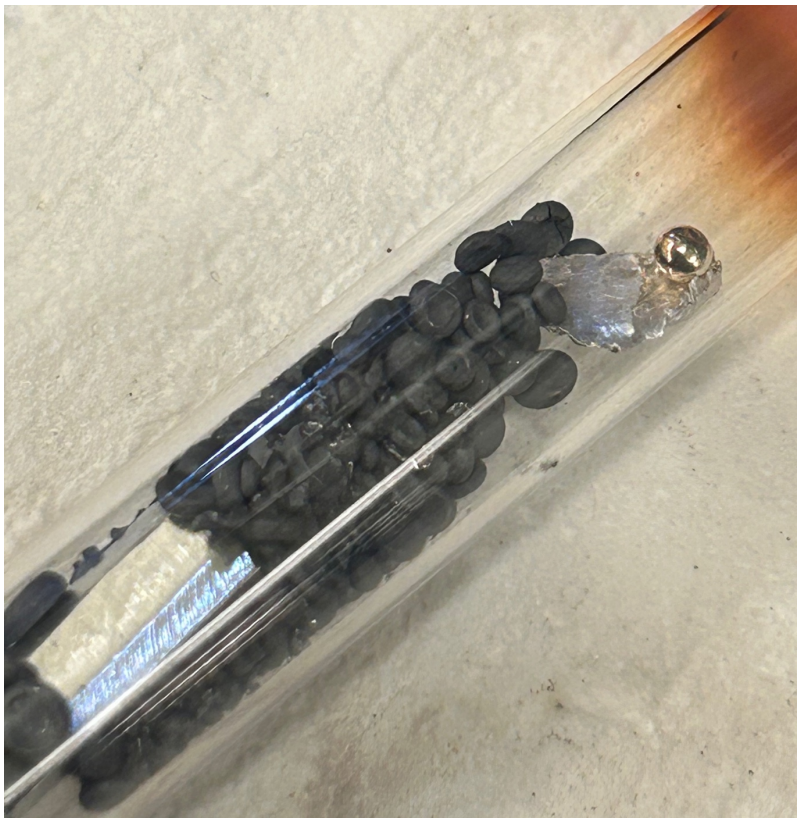

Figure 86. The weighed out and double vacuum sealed Na, Sn, Ag, and Se for the samples with the composition $Na_{0.033}Ag_{0.016}Sn_{0.963}Se$.

Each of the four samples was melted at 1373 K for 30 minutes, followed by water quenching, ball milling for 20 cycles of 5 minutes at 600rpm, and the doped samples were reduced at 758

K for 10 hours, while the undoped sample was reduced at 506 K for 10 hours. Followed by sieving to <63 um and weighing out 3g for hot pressing. Due to breakage of the larger hot press die, larger samples for measurement parallel to the hot pressing direction were not able to be synthesized. This formed the initial set of 4 samples. The additional prepared powders were kept in the glovebox in case a second set needed to be prepared.

These 4 samples were hot pressed with a ramp time of 60 minutes and a holding time of 5 minutes at 773 K with a pressure of 40 MPa. The resulting densities were all in excess of 97.5 %.

Table 2. Densities of the first set of 'optimized' polycrystalline tin selenide samples.

Sample	Density
SnSe	6.04 g cm^{-3} (97.8 %)
$Na_{0.033}Ag_{0.016}Sn_{0.963}Se$	6.08 g cm^{-3} (99.4 %)
$Na_{0.032}Au_{0.015}Sn_{0.963}Se$	6.15 g cm^{-3} (99.8 %)
$SnSe_{0.9}Br_{0.1}$	6.14 g cm^{-3} (99.2 %)

Finally the three doped samples were annealed at 758 K for 3 hours under 5 % H_2/Ar prior to cutting for TD, and ZEM measurements. The undoped sample was annealed at 828 K for 12 hours under 5 % H_2/Ar.

The thermal conductivity of the undoped tin selenide sample had a consistent hysteresis during the heating and cooling phases which was unchanged from the initial cycle to 773 K compared to the cycle to 923 K as shown in Figure 88. The sample with the composition $Na_{0.033}Ag_{0.016}Sn_{0.963}Se$ was found to be stable up to 773 K, and exhibited a similar hysteresis during the cooling from 773 K to RT, with both the first heating cycle to 773 K and final heating cycle to 923 K having consistent results. During the final cooling cycle from 923 K, the sample

was found to have degraded, with greatly reduced thermal conductivity due to bubbling, and permanent thermal expansion from the phase transition.

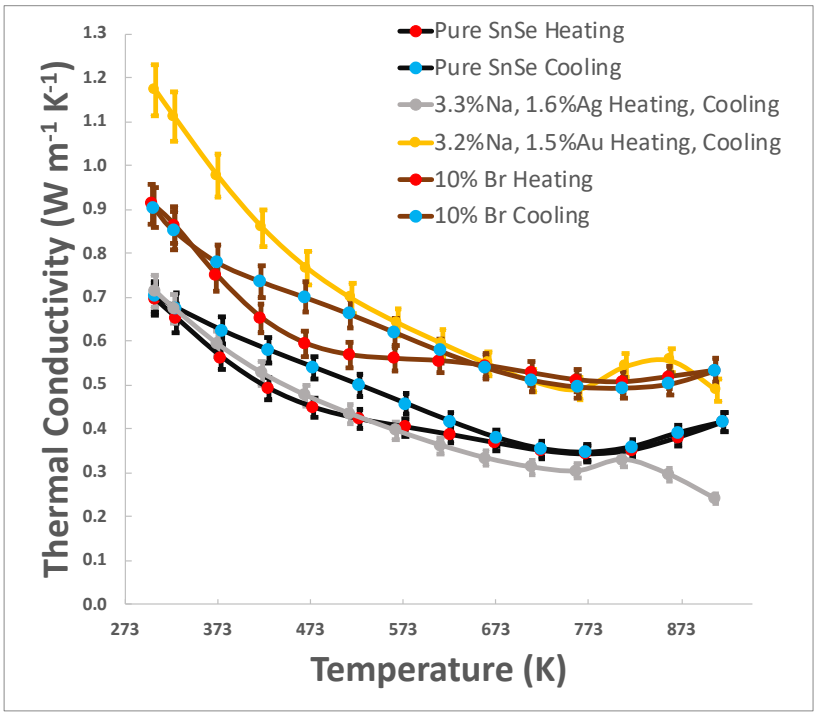

Figure 87. Thermal Conductivity of first set of four 'optimized' tin selenide samples, pictured are the results that were consistent during heating and cooling, the degraded sample results are not shown.

The Na/Ag doped sample yet again showed the lowest thermal conductivity, followed by the undoped SnSe sample, the Br doped sample, and then the Na/Au doped sample. The K_{lat} plot in Figure 88. Further shows the reduced lattice thermal conductivity when doping with Ag compared to Au. However the Na/Au doped sample shows an improved electrical conductivity for this set of samples unlike the previously prepared series, while both the Na/Ag and Na/Au doped samples had very similar Seebeck coefficients. The Br doped sample shows a higher Seebeck coefficient, and lower electrical conductivity compared to the *p*-type

sample which is further evidence that the doping level needs to be increased to reach the optimal carrier concentration.

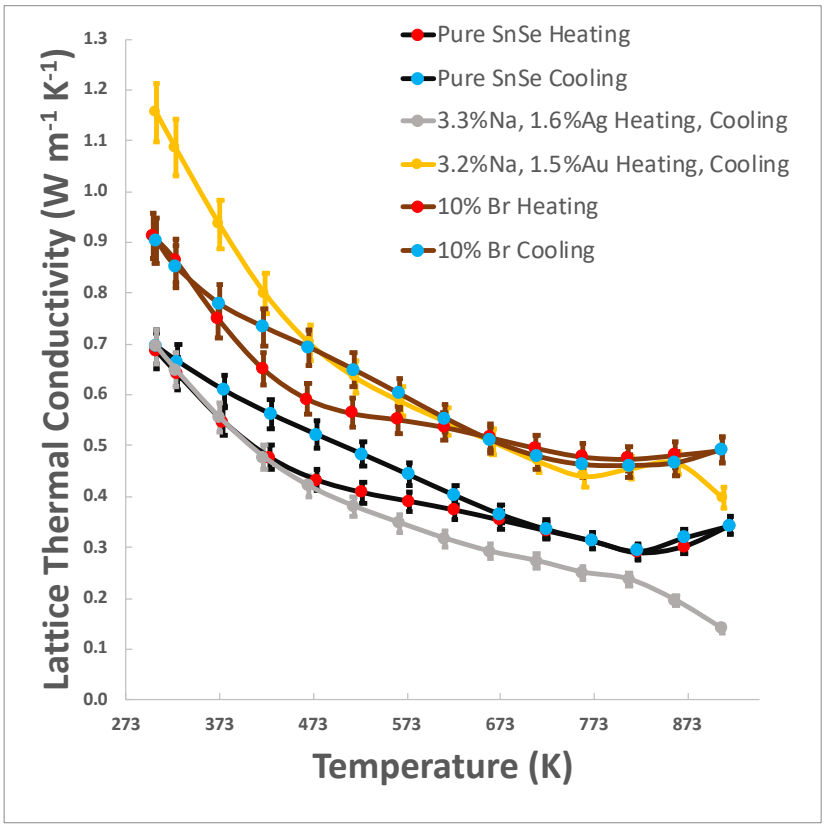

Figure 88. Lattice thermal conductivity of first set of four 'optimized' tin selenide samples.

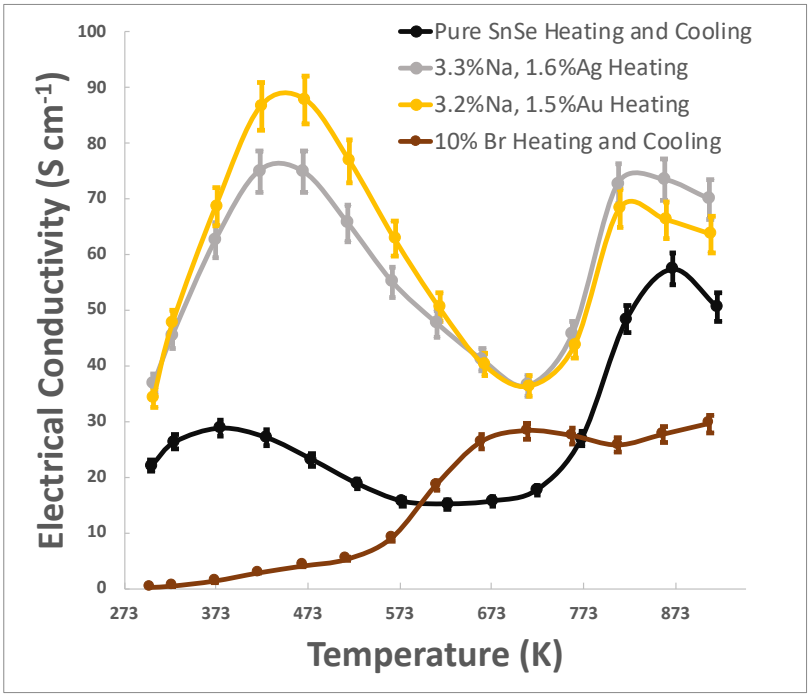

Figure 89. Electrical conductivity of first set of four 'optimized' tin selenide samples.

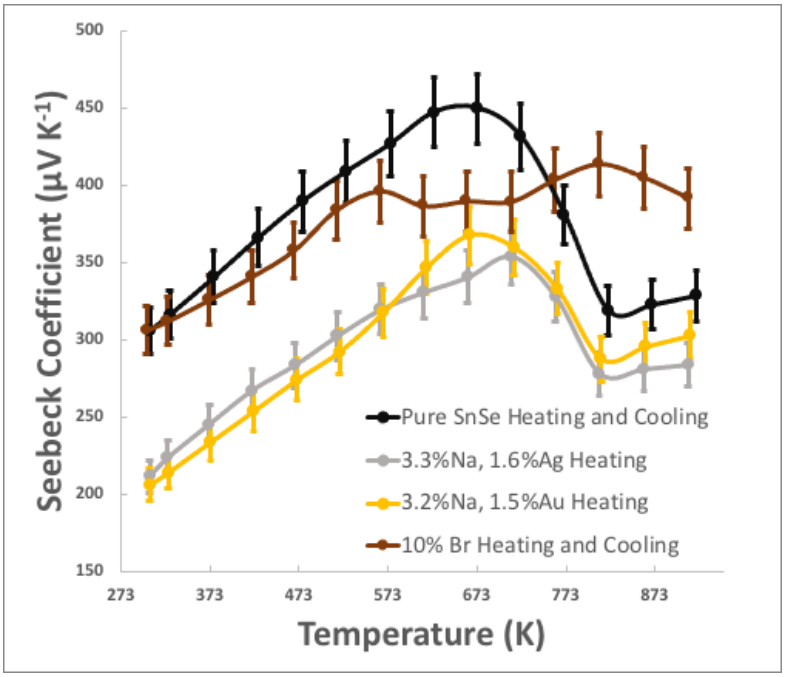

Figure 90. Seebeck coefficient of first set of four 'optimized' tin selenide samples, 10 % Br is shown as an absolute value of its Seebeck coefficient.

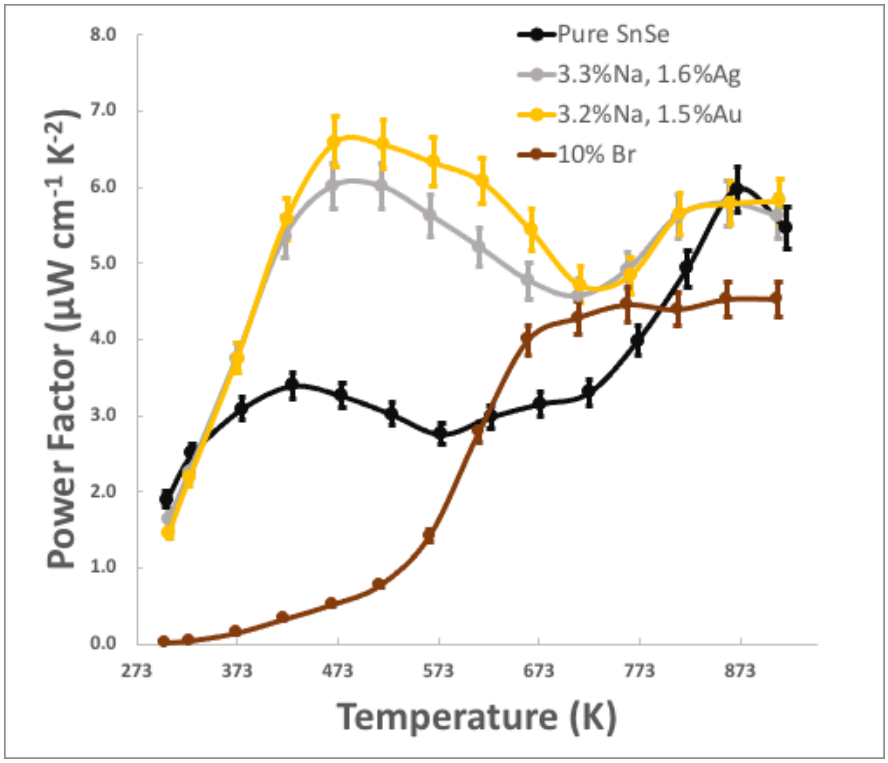

Figure 91. Power Factors of first set of four 'optimized' tin selenide samples.

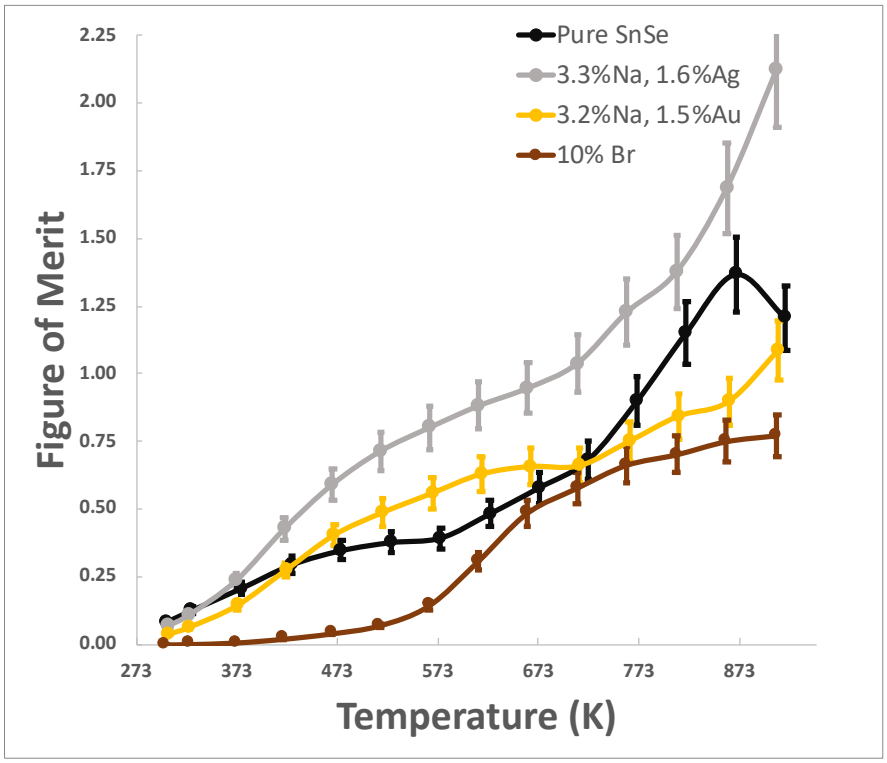

Figure 92. Figure of Merits of first set of four 'optimized' tin selenide samples.

Although the Ag doped sample shows an extremely improved figure of merit compared to the undoped and the Au doped sample due to the significantly reduced thermal conductivity, the results are brought into question because of the further reduced thermal conductivity during cooling from 923 K from the bubbling of the sample. Therefore, a second set was prepared for both the Na/Ag and Na/Au doped samples.

With the hysteresis and instability of the *p*-type samples at the maximum temperature, an attempt was made using the excess powders for the *p*-type samples to hot press followed by annealing at 828 K for 24 hours. The resulting pellets had a very low density after the high temperature annealing step; 5.60 g cm^{-3} for $Na_{0.032}Sn_{0.963}Au_{0.015}Se$, and 5.20 g cm^{-3} for $Na_{0.033}Ag_{0.016}Sn_{0.963}Se$. These pellets were then ground using the mortar and pestle and re-reduced at 904 K for 1 hour under 5 % H_2/Ar followed by hot pressing at 773 K with a 30 minute ramping time and a 10 minute holding time with 40 MPa pressure.

The final resulting pellets had the same composition as the first pellets, and were labelled $Na_{0.032}Sn_{0.963}Au_{0.015}Se$-2 and $Na_{0.033}Ag_{0.016}Sn_{0.963}Se$-2, and had densities of 6.15 g cm^{-3} and 6.08 g cm^{-3} respectively.

Plotting these pellets properties next to the same undoped SnSe sample and the same 10 % Br doped sample follows in Figures 93-98.

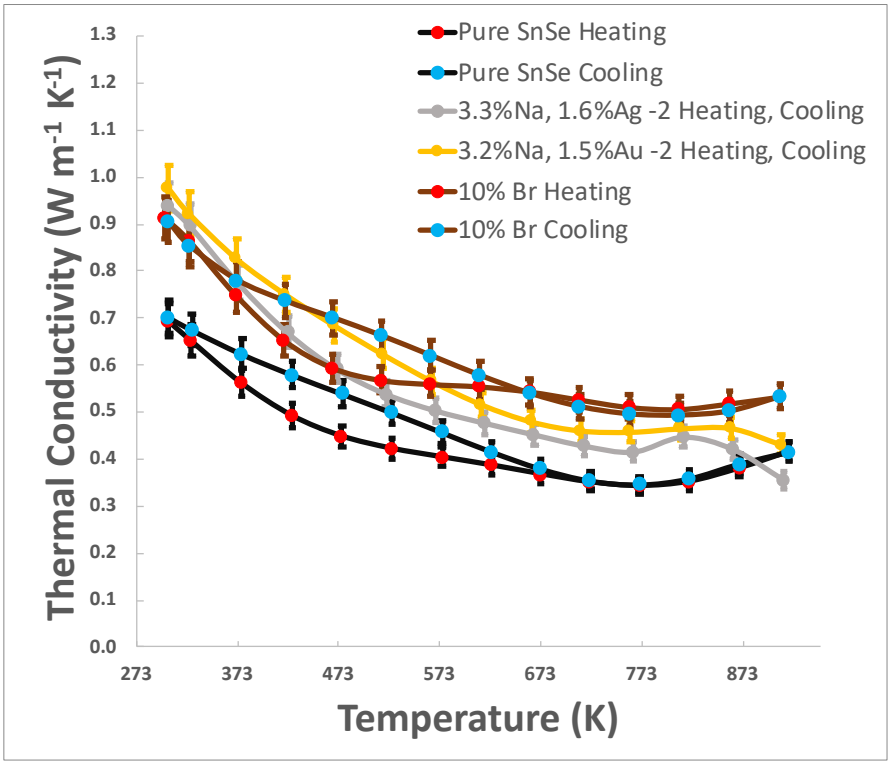

Figure 93. Thermal Conductivity of final set of four 'optimized' tin selenide samples, pictured are the results that were consistent during heating and cooling.

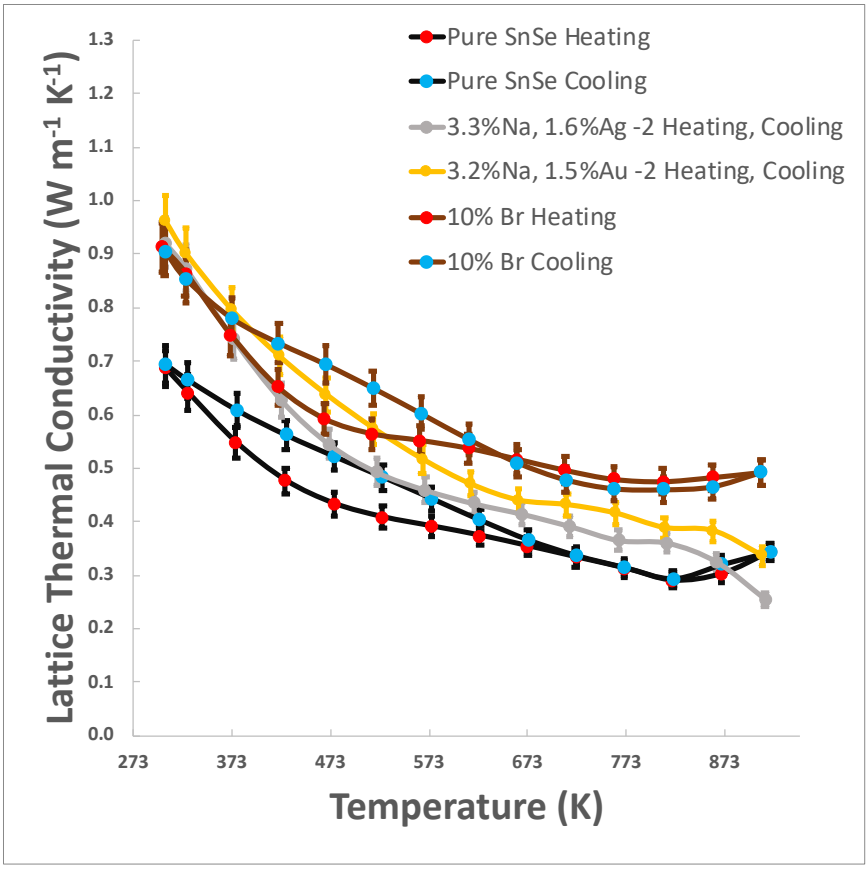

Figure 94. Lattice thermal conductivity of final set of four 'optimized' tin selenide samples, pictured are the results that were consistent during heating and cooling.

After the additional high temperature reduction step, the Na/Au doped sample had a reduced thermal conductivity which matches the other samples more closely, while the Na/Ag doped samples thermal conductivity increased.

The Seebeck coefficients remained nearly unchanged by this additional step, while the electrical conductivity of the Au sample also was unchanged. However the Ag doped sample was negatively affected with a reduced peak electrical conductivity.

Despite this the PF of the Na/Ag doped sample was only reduced slightly, and matched the PF of the Na/Au sample when undergoing the same treatment.

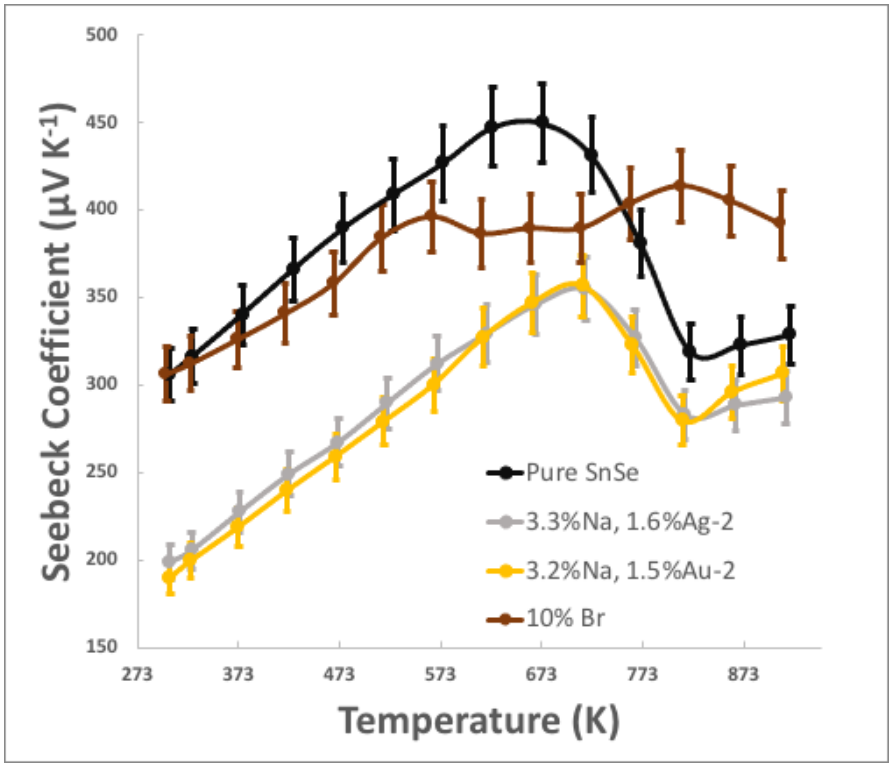

Figure 95. Seebeck coefficients of final set of four 'optimized' tin selenide samples.

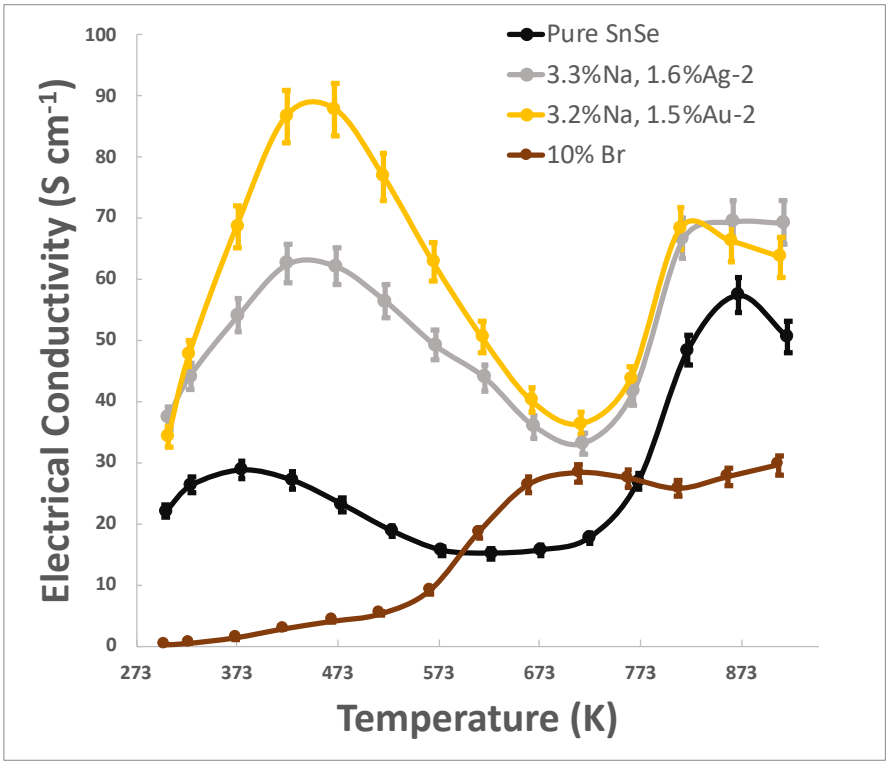

Figure 96. Electrical conductivity of final set of four 'optimized' tin selenide samples.

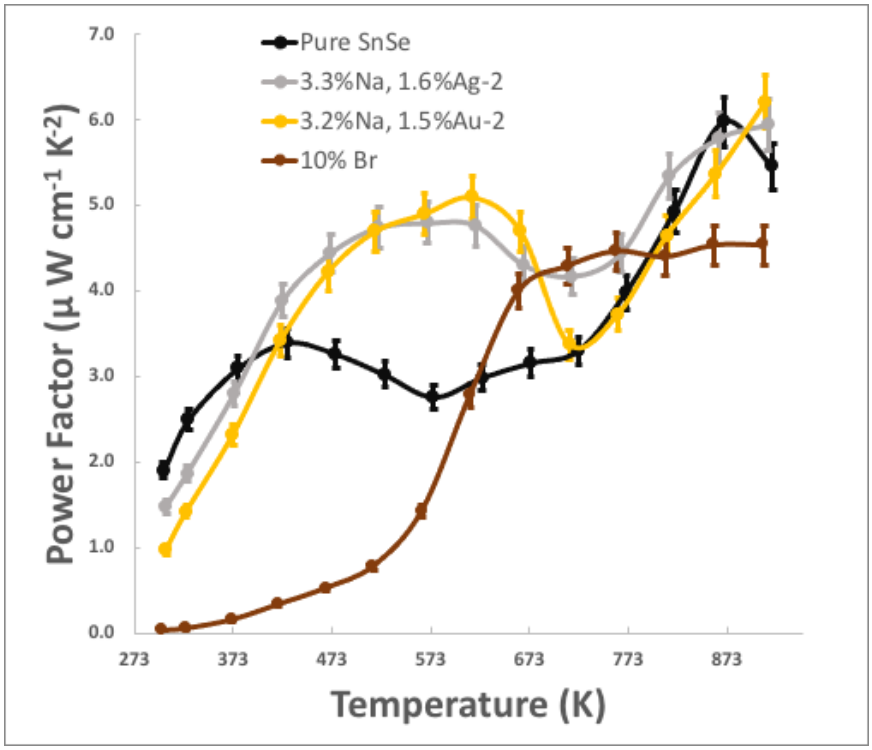

Figure 97. Power Factors of final set of four 'optimized' tin selenide samples.

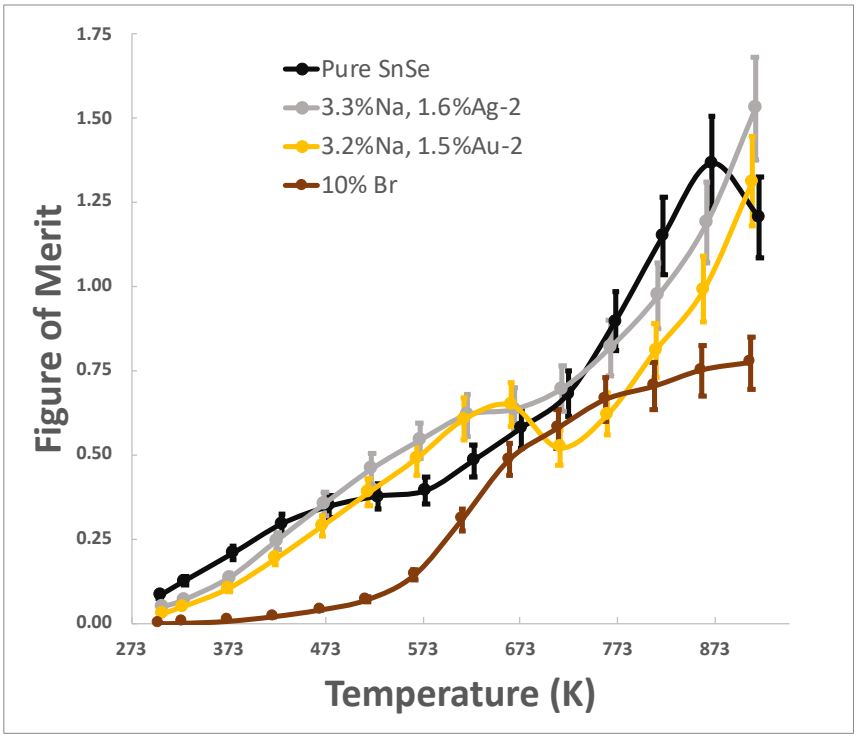

Figure 98. Maximum *zT* of final set of four 'optimized' tin selenide samples.

The ZT results from this additional high temperature process also showed an improved *zT* for the Na/Au doped sample, due to the reduced thermal conductivity, while the Na/Ag doped samples *zT* was reduced and is similar to the Au doped sample.

Ultimately one of the key conclusions from this was that as going down the group from Cu-Ag-Au, the reactivity, and thus sensitivity of the resulting tin selenide material is reduced. Ag doping reaches a good balance, as it is less reactive than Cu, while also achieving a high doping efficiency, and when compared to Au, doing so at a reduced cost.

Chapter 6: Summary and Outlook

Polycrystalline tin selenide is a difficult material to optimize the properties with due to the sensitivity of the synthesis and sensitivity of the material. Although the material holds a high potential for future improvement, this sensitivity is a limiting factor in both research and future industrial usage. Comparing some of the highest performing samples from this thesis with the recently published record holding sample by Zhou et al.[2] in Figure 99. This shows possibility for future improvement using doping strategies such as double doping, if combined with the oxide removal technique using higher purity tin. The oxide removal process is the most important stage in the synthesis of tin selenide samples due to the extreme sensitivity of the properties to any amount of oxides. This is a particular challenge during research as measuring the extremely small amount of oxides in the tin starting material in a quantitative way requires a method such as atom-probe-tomography. Other methods are unlikely to even show a signal from the minute quantities of oxides required to negatively affect the properties. However with careful preparation using identical starting materials, and ensuring the synthesis process is perfect, comparisons can be made between samples from the same batch to draw conclusions about doping, and material engineering of tin selenide samples. Comparing different published absolute values of *zT* results from tin selenide samples may not lead to the "true" conclusions as differing levels of oxides present between the published results may lead to poor conclusions. However within a single study, the results may be considered accurate for internal comparison.

Additionally it is possible to consider that prior published results for tin selenide samples with the amount of doping required may be skewed by the oxide content. This may also explain

the discrepancy between doping studies on polycrystalline tin selenide and single crystal tin selenide, where multiple studies have required larger amounts of the doping element to achieve the required carrier concentrations in the polycrystalline samples; usually in the range of 3 % for single crystal doping, and up to 10 % in some polycrystalline doping.

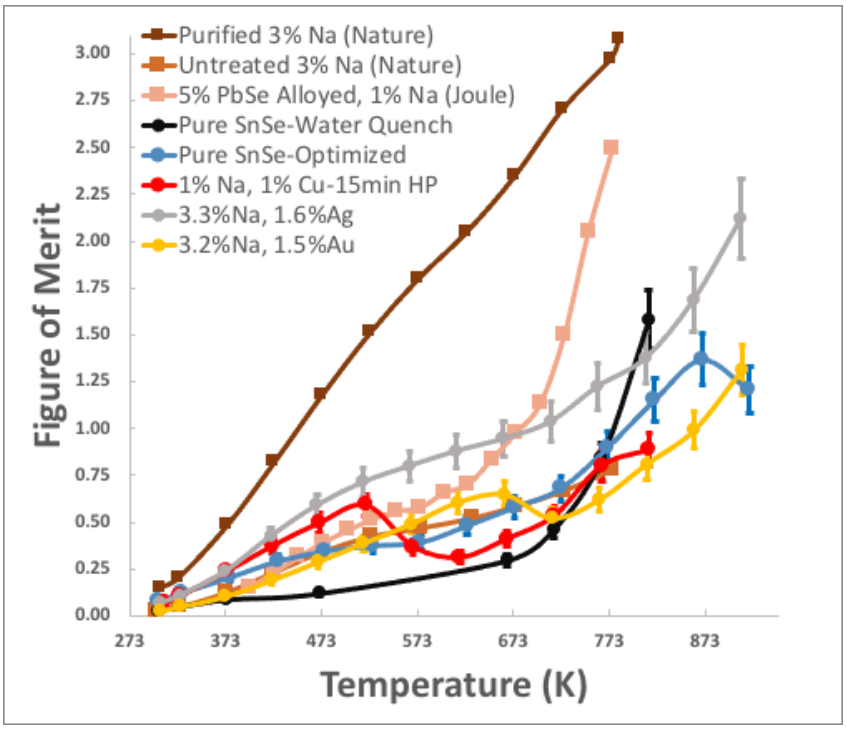

Figure 99. The top 3 *p*-type doped samples prepared, as well as the two highest performing pure SnSe samples, compared to the record holding purified $Na_{0.03}Sn_{0.965}Se$, untreated $Na_{0.03}Sn_{0.965}Se$ from Nature, and SnSe-5 % PbSe doped with 1 % Na from Joule.[2,22]

In Figure 99, the low temperature *zT* results of the double doped *p*-type samples were improved compared to two of the previously published results. However either due to oxide contamination which negatively impacts the ultra-low thermal conductivity as the

temperature increases, and electrical conductivity, or oxidation during the ZEM measurement, as the temperature increased, the results were not improved. Given the higher total thermal conductivity results of the samples prepared in this thesis, as well as the oxidation during ZEM measurements, it is reasonable to conclude that oxide contamination led to the poor maximum *zT* results. When comparing the results of the optimized *p*-type double doped samples to the 3 % Na sample from Chapter 3 with the same composition as Zhou et al.'s record holding sample, double doping was found to be successful in improving the average and maximum *zT*.

In the future testing new methods of double doping for *n*-type doping should be attempted in polycrystalline SnSe, as the *n*-type samples are much less sensitive to oxidation during the measurement, have a large room for improvement, as well as are highly stable up to 923 K, unlike some of the *p*-type samples which may begin degrading beyond 773-823 K. A proposed method is to use high amounts of Bi and Br doping separately, followed by ball milling the two individual powders together. Alternatively an entirely ball milled synthesis could be chosen; such as ball mill the starting materials for the composition $Sn_{0.8}Bi_{0.2}Se$, and the starting materials for $SnSe_{0.8}Br_{0.2}$, followed by reducing each powder separately. Then ball mill the two powders together resulting in the composition $Sn_{0.9}Bi_{0.1}Se_{0.9}Br_{0.1}$. Such a method might avoid low Seebeck coefficients shown in Chapter 4, as well as result in lower thermal conductivity due to the fully ball milled synthesis. Or by doping with Cl and Br together only on the Se atomic sites this might further avoid the issue of low power factors when double doping *n*-type tin selenide.

References

(1) Chen, Z. G.; Shi, X.; Zhao, L. D.; Zou, J. High-Performance SnSe Thermoelectric Materials: Progress and Future Challenge. *Prog. Mater. Sci.* **2018**, *97*, 283–346. https://doi.org/10.1016/j.pmatsci.2018.04.005.

(2) Zhou, C.; Lee, Y. K.; Yu, Y.; Byun, S.; Luo, Z. Z.; Lee, H.; Ge, B.; Lee, Y. L.; Chen, X.; Lee, J. Y.; Cojocaru-Mirédin, O.; Chang, H.; Im, J.; Cho, S. P.; Wuttig, M.; Dravid, V. P.; Kanatzidis, M. G.; Chung, I. Polycrystalline SnSe with a Thermoelectric Figure of Merit Greater than the Single Crystal. *Nat. Mater.* **2021**, *20* (10), 1378–1384. https://doi.org/10.1038/s41563-021-01064-6.

(3) Bos, J. W. Thermoelectric Materials: Efficiencies Found in Nanocomposites. *Educ. Chem.* **2012**, *49* (2), 15–18. ISSN 00131350.

(4) DiSalvo, F. J. Thermoelectric Cooling and Power Generation. *Science .* **1999**, *285* (5428), 703–706. https://doi.org/10.1126/science.285.5428.703.

(5) Sharma, S.; Dwivedi, V. K.; Pandit, S. N. A Review of Thermoelectric Devices for Cooling Applications. *Int. J. Green Energy* **2014**, *11* (9), 899–909. https://doi.org/10.1080/15435075.2013.829778.

(6) Hamid Elsheikh, M.; Shnawah, D. A.; Sabri, M. F. M.; Said, S. B. M.; Haji Hassan, M.; Ali Bashir, M. B.; Mohamad, M. A Review on Thermoelectric Renewable Energy: Principle Parameters That Affect Their Performance. *Renew. Sustain. Energy Rev.* **2014**, *30*, 337–355. https://doi.org/10.1016/j.rser.2013.10.027.

(7) Xiao-Lei Shi, Jin Zou, and Z.-G. C. Advanced Thermoelectric Design: From Materials and Structures to Devices. *Chem. Rev.* **2020**, 120 (15), 7399–7515. https://doi.org/10.1021/acs.chemrev.0c00026.

(8) Lalonde, A. D.; Pei, Y.; Wang, H.; Jeffrey Snyder, G. Lead Telluride Alloy Thermoelectrics. *Mater. Today* **2011**, *14* (11), 526–532. https://doi.org/10.1016/S1369-7021(11)70278-4.

(9) Tritt, T. M. *Thermal Conductivity Theory, Properties, and Applications*; US: New York, *Kluwer Academic.* 2004. ISBN 0-306-48327-0

(10) Chang, C.; Wu, M.; He, D.; Pei, Y.; Wu, C. F.; Wu, X.; Yu, H.; Zhu, F.; Wang, K.; Chen, Y.; Huang, L.; Li, J. F.; He, J.; Zhao, L. D. 3D Charge and 2D Phonon Transports Leading to High Out-of-Plane *ZT* in *n*-Type SnSe Crystals. *Science.* **2018**, *360* (6390), 778–783. https://doi.org/10.1126/science.aaq1479.

(11) Li, S.; Wang, Y.; Chen, C.; Li, X.; Xue, W.; Wang, X.; Zhang, Z.; Cao, F.; Sui, J.; Liu, X.; Zhang, Q. Heavy Doping by Bromine to Improve the Thermoelectric Properties of *n*-Type Polycrystalline SnSe. *Adv. Sci.* **2018**, *5* (9), 6–11. https://doi.org/10.1002/advs.201800598.

(12) Zhao, L. D.; Lo, S. H.; Zhang, Y.; Sun, H.; Tan, G.; Uher, C.; Wolverton, C.; Dravid, V. P.; Kanatzidis, M. G. Ultralow Thermal Conductivity and High Thermoelectric Figure of Merit in SnSe Crystals. *Nature* **2014**, *508* (7496), 373–377. https://doi.org/10.1038/nature13184.

(13) Xu, X.; Zhou, J.; Chen, J. Thermal Transport in Conductive Polymer–Based Materials. *Adv. Funct. Mater.* **2020**, *30* (8), 1–18. https://doi.org/10.1002/adfm.201904704.

(14) Nolas, G. S.; Sharp, J.; Goldsmid, H. J. *Thermoelectrics: Basic Principles and New Materials Developments*; US: New York*, Springer.* 2001. ISSN 0933-033X

(15) Lucas, A.; Das Sarma, S. Electronic Hydrodynamics and the Breakdown of the Wiedemann-Franz and Mott Laws in Interacting Metals. *Phys. Rev. B* **2018**, *97* (24), 1–16. https://doi.org/10.1103/PhysRevB.97.245128.

(16) Franz, R., Wiedemann, G. Über die Wärme-Leitungsfähigkeit der Metalle. Ann. Phys. Chem. **1853**, 165 (8), 497–531. https://doi.org/10.1002/andp.18531650802

(17) Kim, H. S.; Gibbs, Z. M.; Tang, Y.; Wang, H.; Snyder, G. J. Characterization of Lorenz Number with Seebeck Coefficient Measurement. *APL Mater.* **2015**, *3* (4), 1–6. https://doi.org/10.1063/1.4908244.

(18) Wang, H.; Porter, W. D.; Böttner, H.; König, J.; Chen, L.; Bai, S.; Tritt, T. M.; Mayolet, A.; Senawiratne, J.; Smith, C.; Harris, F.; Gilbert, P.; Sharp, J.; Lo, J.; Kleinke, H.; Kiss, L. Transport Properties of Bulk Thermoelectrics: An International Round-Robin Study, Part II: Thermal Diffusivity, Specific Heat, and Thermal Conductivity. *J. Electron. Mater.* **2013**, *42* (6), 1073–1084. https://doi.org/10.1007/s11664-013-2516-0.

(19) Bulusu, A.; Walker, D. G. Review of Electronic Transport Models for Thermoelectric Materials. *Superlattices Microstruct.* **2008**, *44* (1), 1–36. https://doi.org/10.1016/j.spmi.2008.02.008.

(20) Cutler, M.; Mott, N. F. Observation of Anderson Localization in an Electron Gas. *Phys. Rev.* **1969**, *181* (3), 1336–1340. https://doi.org/10.1103/PhysRev.181.1336.

(21) Hummel, R. E. *Electronic Properties of Materials*, 4th edition.; Springer US: Gainesville, FL,

2011. https://doi.org/10.1007/978-1-4419-8164-6.

(22) Lee, Y. K.; Luo, Z.; Cho, S. P.; Kanatzidis, M. G.; Chung, I. Surface Oxide Removal for Polycrystalline SnSe Reveals Near-Single-Crystal Thermoelectric Performance. *Joule* **2019**, *3* (3), 719–731. https://doi.org/10.1016/j.joule.2019.01.001.

(23) Li, C.; Guo, D.; Li, K.; Shao, B.; Chen, D.; Ma, Y.; Sun, J. Excellent Thermoelectricity Performance of *p*-Type SnSe along b Axis. *Phys. B Condens. Matter* **2018**, *530*, 264–269. https://doi.org/10.1016/j.physb.2017.11.074.

(24) Shi, W.; Gao, M.; Wei, J.; Gao, J.; Fan, C.; Ashalley, E.; Li, H.; Wang, Z. Tin Selenide (SnSe): Growth, Properties, and Applications. *Adv. Sci.* **2018**, *5* (4), 1700602. https://doi.org/10.1002/advs.201700602.

(25) Grüneisen, E. Theorie Des Festen Zustandes Einatomiger Elemente. *Ann. Phys.* **1912**, *344* (12), 257–306. https://doi.org/10.1002/andp.19123441202.

(26) Porter, L. J.; Justo, J. F.; Yip, S. The Importance of Grüneisen Parameters in Developing Interatomic Potentials. *J. Appl. Phys.* **1997**, *82* (11), 5378–5381. https://doi.org/10.1063/1.366305.

(27) Dugdale, J. S.; MacDonald, D. K. C. Vibrational Anharmonicity and Lattice Thermal Properties. *Phys. Rev.* **1954**, *96* (1), 57–62. https://doi.org/10.1103/PhysRev.96.57.

(28) Banik, A.; Biswas, K. A Game-Changing Strategy in SnSe Thermoelectrics. *Joule* **2019**, *3* (3), 636–638. https://doi.org/10.1016/j.joule.2019.03.001.

(29) Chen, Y. X.; Ge, Z. H.; Yin, M.; Feng, D.; Huang, X. Q.; Zhao, W.; He, J. Understanding of the Extremely Low Thermal Conductivity in High-Performance Polycrystalline SnSe

through Potassium Doping. *Adv. Funct. Mater.* **2016**, *26* (37), 6836–6845. https://doi.org/10.1002/adfm.201602652.

(30) Ge, Z. H.; Song, D.; Chong, X.; Zheng, F.; Jin, L.; Qian, X.; Zheng, L.; Dunin-Borkowski, R. E.; Qin, P.; Feng, J.; Zhao, L. D. Boosting the Thermoelectric Performance of (Na,K)-Codoped Polycrystalline SnSe by Synergistic Tailoring of the Band Structure and Atomic-Scale Defect Phonon Scattering. *J. Am. Chem. Soc.* **2017**, *139* (28), 9714–9720. https://doi.org/10.1021/jacs.7b05339.

(31) Cai, B.; Li, J.; Sun, H.; Zhao, P.; Yu, F.; Zhang, L.; Yu, D.; Tian, Y.; Xu, B. Sodium Doped Polycrystalline SnSe: High Pressure Synthesis and Thermoelectric Properties. *J. Alloys Compd.* **2017**, *727*, 1014–1019. https://doi.org/10.1016/j.jallcom.2017.08.223.

(32) Chu, F.; Zhang, Q.; Zhou, Z.; Hou, D.; Wang, L.; Jiang, W. Enhanced Thermoelectric and Mechanical Properties of Na-Doped Polycrystalline SnSe Thermoelectric Materials via CNTs Dispersion. *J. Alloys Compd.* **2018**, *741*, 756–764. https://doi.org/10.1016/j.jallcom.2018.01.178.

(33) Gong, Y.; Chang, C.; Wei, W.; Liu, J.; Xiong, W.; Chai, S.; Li, D.; Zhang, J.; Tang, G. Extremely Low Thermal Conductivity and Enhanced Thermoelectric Performance of Polycrystalline SnSe by Cu Doping. *Scr. Mater.* **2018**, *147*, 74–78. https://doi.org/10.1016/j.scriptamat.2017.12.035.

(34) González-Romero, R. L.; Meléndez, J. J. Variation of the *ZT* Factor of SnSe with Doping: A First-Principles Study. *J. Alloys Compd.* **2018**, *732*, 536–546. https://doi.org/10.1016/j.jallcom.2017.10.196.

(35) Lin, C. C.; Ginting, D.; Kim, G.; Ahn, K.; Rhyee, J. S. High Thermoelectric Performance and Low Thermal Conductivity in K-Doped SnSe Polycrystalline Compounds. *Curr. Appl. Phys.* **2018**, *18* (12), 1534–1539. https://doi.org/10.1016/j.cap.2018.09.011.

(36) Lin, C. C.; Lydia, R.; Yun, J. H.; Lee, H. S.; Rhyee, J. S. Extremely Low Lattice Thermal Conductivity and Point Defect Scattering of Phonons in Ag-Doped (SnSe)1-x(SnS)x Compounds. *Chem. Mater.* **2017**, *29* (12), 5344–5352. https://doi.org/10.1021/acs.chemmater.7b01612.

(37) Liu, J.; Wang, P.; Wang, M.; Xu, R.; Zhang, J.; Liu, J.; Li, D.; Liang, N.; Du, Y.; Chen, G.; Tang, G. Achieving High Thermoelectric Performance with Pb and Zn Codoped Polycrystalline SnSe via Phase Separation and Nanostructuring Strategies. *Nano Energy* **2018**, *53* (July), 683–689. https://doi.org/10.1016/j.nanoen.2018.09.025.

(38) Luo, Y.; Cai, S.; Hua, X.; Chen, H.; Liang, Q.; Du, C.; Zheng, Y.; Shen, J.; Xu, J.; Wolverton, C.; Dravid, V. P.; Yan, Q.; Kanatzidis, M. G. High Thermoelectric Performance in Polycrystalline SnSe Via Dual-Doping with Ag/Na and Nanostructuring With Ag8SnSe6. *Adv. Energy Mater.* **2019**, *9* (2), 1803072/1–8. https://doi.org/10.1002/aenm.201803072.

(39) Shi, X. L.; Tao, X.; Zou, J.; Chen, Z. G. High-Performance Thermoelectric SnSe: Aqueous Synthesis, Innovations, and Challenges. *Adv. Sci.* **2020**, *7* (7), 1902923/1-51 https://doi.org/10.1002/advs.201902923.

(40) Wei, T. R.; Tan, G.; Zhang, X.; Wu, C. F.; Li, J. F.; Dravid, V. P.; Snyder, G. J.; Kanatzidis, M. G. Distinct Impact of Alkali-Ion Doping on Electrical Transport Properties of Thermoelectric *p*-Type Polycrystalline SnSe. *J. Am. Chem. Soc.* **2016**, *138* (28), 8875–

8882. https://doi.org/10.1021/jacs.6b04181.

(41) Zhang, L.; Wang, J.; Sun, Q.; Qin, P.; Cheng, Z.; Ge, Z.; Li, Z.; Dou, S. Three-Stage Inter-Orthorhombic Evolution and High Thermoelectric Performance in Ag-Doped Nanolaminar SnSe Polycrystals. *Adv. Energy Mater.* **2017**, *7* (19), 1700573/1–12. https://doi.org/10.1002/aenm.201700573.

(42) Singh, N. K.; Bathula, S.; Gahtori, B.; Tyagi, K.; Haranath, D.; Dhar, A. The Effect of Doping on Thermoelectric Performance of *p*-Type SnSe: Promising Thermoelectric Material. *J. Alloys Compd.* **2016**, *668*, 152–158. https://doi.org/10.1016/j.jallcom.2016.01.190.

(43) Zhao, Q.; Qin, B.; Wang, D.; Qiu, Y.; Zhao, L. D. Realizing High Thermoelectric Performance in Polycrystalline SnSe via Silver Doping and Germanium Alloying. *ACS Appl. Energy Mater.* **2020**, *3* (3), 2049–2054. https://doi.org/10.1021/acsaem.9b01475.

(44) Duong, A. T.; Nguyen, V. Q.; Duvjir, G.; Duong, V. T.; Kwon, S.; Song, J. Y.; Lee, J. K.; Lee, J. E.; Park, S.; Min, T.; Lee, J.; Kim, J.; Cho, S. Achieving *ZT*=2.2 with Bi-Doped *n*-Type SnSe Single Crystals. *Nat. Commun.* **2016**, *7*, 13713/1–6. https://doi.org/10.1038/ncomms13713.

(45) Li, X.; Chen, C.; Xue, W.; Li, S.; Cao, F.; Chen, Y.; He, J.; Sui, J.; Liu, X.; Wang, Y.; Zhang, Q. *n*-Type Bi-Doped SnSe Thermoelectric Nanomaterials Synthesized by a Facile Solution Method. *Inorg. Chem.* **2018**, *57* (21), 13800–13808. https://doi.org/10.1021/acs.inorgchem.8b02324.

(46) Wei, Wei.; Cheng, Chang.; Teng, Yang.; et al. Achieving High Thermoelectric Figure of Merit in Polycrystalline SnSe via Introducing Sn Vacancies. *J. Am. Chem Soc*. **2018**, 140, 1,

499-505

https://doi.org/10.1021/jacs.7b11875

(47) Chandra, S.; Biswas, K. Realization of High Thermoelectric Figure of Merit in Solution Synthesized 2D SnSe Nanoplates via Ge Alloying. *J. Am. Chem. Soc.* **2019**, *141* (15), 6141–6145. https://doi.org/10.1021/jacs.9b01396.

(48) Rui, Xu.; Lulu, Huang.; Jian, Zhang.; Di, Li.; Jizi, Li.; Jiang, Liu.; Jun, Fang.; Meiyu, Wang.; Guodong, Tang.; Nanostructured SnSe Integrated with Se Quantum Dots with Ultrahigh Power Factor and Thermoelectric Performance from Magnetic Field-Assisted Hydrothermal Synthesis†. *J. Mater. Chem. A* **2017**, No. 26, 13828–13841. https://doi.org/10.1039/c3ta12421e.

(49) Lu, W.; Li, S.; Xu, R.; Zhang, J.; Li, D.; Feng, Z.; Zhang, Y.; Tang, G. Boosting Thermoelectric Performance of SnSe via Tailoring Band Structure, Suppressing Bipolar Thermal Conductivity, and Introducing Large Mass Fluctuation. *ACS Appl. Mater. Interfaces* **2019**, *11* (48), 45133–45141. https://doi.org/10.1021/acsami.9b17811.

(50) Asfandiyar; Cai, B.; Zhuang, H. L.; Tang, H.; Li, J. F. Polycrystalline SnSe–Sn1–vS Solid Solutions: Vacancy Engineering and Nanostructuring Leading to High Thermoelectric Performance. *Nano Energy* **2020**, *69*, 104393/1-9. https://doi.org/10.1016/j.nanoen.2019.104393.

(51) Burton, M. R.; Mehraban, S.; Beynon, D.; McGettrick, J.; Watson, T.; Lavery, N. P.; Carnie, M. J. 3D Printed SnSe Thermoelectric Generators with High Figure of Merit. *Adv. Energy Mater.* **2019**, *9* (26), 1900201/1-8. https://doi.org/10.1002/aenm.201900201.

(52) Tang, G.; Wei, W.; Zhang, J.; Li, Y.; Wang, X.; Xu, G.; Chang, C.; Wang, Z.; Du, Y.; Zhao, L. D. Realizing High Figure of Merit in Phase-Separated Polycrystalline Sn1-XPbxSe. *J. Am. Chem. Soc.* **2016**, *138* (41), 13647–13654. https://doi.org/10.1021/jacs.6b07010.

(53) Guo, H.; Xin, H.; Qin, X.; Zhang, J.; Li, D.; Li, Y.; Song, C.; Li, C. Enhanced Thermoelectric Performance of Highly Oriented Polycrystalline SnSe Based Composites Incorporated with SnTe Nanoinclusions. *J. Alloys Compd.* **2016**, *689*, 87–93. https://doi.org/10.1016/j.jallcom.2016.07.291.

(54) Shi, X.; Zheng, K.; Hong, M.; Liu, W.; Moshwan, R.; Wang, Y.; Qu, X.; Chen, Z. G.; Zou, J. Boosting the Thermoelectric Performance of *p*-Type Heavily Cu-Doped Polycrystalline SnSe: Via Inducing Intensive Crystal Imperfections and Defect Phonon Scattering. *Chem. Sci.* **2018**, *9* (37), 7376–7389. https://doi.org/10.1039/c8sc02397b.

(55) Li, M.; Shao, H.; Xu, J.; Wu, Q.; Tan, X.; Liu, G.; Jin, M.; Hu, H.; Huang, H.; Zhang, J.; Jiang, J. Microstructure Engineering beyond SnSe1-xSx Solid Solution for High Thermoelectric Performance. *J. Mater.* **2018**, *4* (4), 321–328. https://doi.org/10.1016/j.jmat.2018.09.001.

(56) Lee, Y. K.; Ahn, K.; Cha, J.; Zhou, C.; Kim, H. S.; Choi, G.; Chae, S. I.; Park, J. H.; Cho, S. P.; Park, S. H.; Sung, Y. E.; Lee, W. B.; Hyeon, T.; Chung, I. Enhancing *p*-Type Thermoelectric Performances of Polycrystalline SnSe via Tuning Phase Transition Temperature. *J. Am. Chem. Soc.* **2017**, *139* (31), 10887–10896. https://doi.org/10.1021/jacs.7b05881.

(57) Zhao, L. D.; Chang, C.; Tan, G.; Kanatzidis, M. G. SnSe: A Remarkable New Thermoelectric Material. *Energy Environ. Sci.* **2016**, *9* (10), 3044–3060.

https://doi.org/10.1039/c6ee01755j.

(58) Kim, B. S.; Lee, J. C.; Yoon, H. S.; Kim, S. K. Reduction of SnO2 with Hydrogen. *Mater. Trans.* **2011**, *52* (9), 1814–1817. https://doi.org/10.2320/matertrans.M2011118.

(59) Yang, S.; Si, J.; Su, Q.; Wu, H. Enhanced Thermoelectric Performance of SnSe Doped with Layered MoS2/Graphene. *Mater. Lett.* **2017**, *193*, 146–149. https://doi.org/10.1016/j.matlet.2017.01.079.